



UNIVERSITY OF THE PHILIPPINES

Bachelor of Science in Physics

Jesus Miguel A. Yulo II

*Dynamics and strange attractors of stellar pulsation in one-zone  
models of long-period variable stars*

Thesis Adviser:

Michael Francis Ian G. Vega II, Ph.D.

National Institute of Physics

University of the Philippines Diliman

Date of Submission:

June 2022

Thesis Classification:

**P**

*This thesis is not available to the public. Please ask the library for assistance.*

Title of Thesis: Dynamics and strange attractors of stellar pulsation in one-zone models of long-period variable stars

Author: Jesus Miguel A. Yulo II

BS Physics Thesis

National Institute of Physics

University of the Philippines Diliman

June 2022

Classification\* : P

\* I – invention or creation, P – publication, C – confidential information

Available to the general public	No
Available only after consultation with author/adviser for thesis	Yes
Available only to those bound by nondisclosure or confidentiality agreement	Yes



(signature above printed name)

Jesus Miguel A. Yulo II

Student



(signature above printed name)

Michael Francis Ian G. Vega II, Ph.D.

Thesis Adviser

## Honor Code

By submitting this thesis, I affirm that I uphold the core values of Honor and Excellence as codified in the University of the Philippines Code of Student Conduct. This work adheres to the highest standards of academic integrity wherein scholarly sources have been attributed accurately; data has been collected and analyzed in accordance with established academic and scientific practices; and results have been reported in a scholarly and transparent manner.

A handwritten signature in black ink, appearing to read 'Miguel Yulo II', written in a cursive style.

Jesus Miguel A. Yulo II



**NATIONAL INSTITUTE OF PHYSICS**  
COLLEGE OF SCIENCE  
University of the Philippines  
Diliman, Quezon City 1101 Metro-Manila  
Tel. +63 2 920-97-49 www.nip.upd.edu.ph



### ENDORSEMENT

This is to certify that this undergraduate thesis entitled **DYNAMICS AND STRANGE ATTRACTORS OF STELLAR PULSATION IN ONE-ZONE MODELS OF LONG-PERIOD VARIABLE STARS** prepared and submitted by Jesus Miguel A. Yulo II, is hereby endorsed for acceptance as partial fulfillment of the requirements for the degree of Bachelor of Science in Physics.

MICHAEL FRANCIS IAN G. VEGA II, Ph.D.  
Thesis Adviser

This undergraduate thesis is hereby officially accepted in partial fulfillment of the requirements for the degree of Bachelor of Science in Physics.

WILSON O. GARCIA, Ph.D.  
Director  
National Institute of Physics



**NATIONAL INSTITUTE OF PHYSICS**  
**COLLEGE OF SCIENCE**  
 University of the Philippines  
 Diliman, Quezon City 1101 Metro-Manila  
 Telephone No. 981-8500 Locals 3701/3704



June 1, 2022

Dr. Wilson O. Garcia  
 Director  
 National Institute of Physics  
 C.S., U.P. Diliman, Quezon City

Dear Dr. Garcia:

Below is the official action of the panel members in the undergraduate thesis defense of Mr. Jesus Miguel A. Yulo II. The defense of the thesis entitled "**DYNAMICS AND STRANGE ATTRACTORS OF STELLAR PULSATION IN ONE-ZONE MODELS OF LONG-PERIOD VARIABLE STARS**" was held via Zoom link: <https://up-edu.zoom.us/j/98230394167> on Wednesday, 1 June 2022, 2:45 P.M.

Panel Members	<u>Rating</u>	
	PASSED	FAILED
Angelo Marco A. Ramoso, M.Sc. Instructor of Physics National Institute of Physics C.S., U.P. Diliman, Quezon City		_____
John Jaykel P. Magadan, M.Sc. Instructor of Physics National Institute of Physics C.S., U.P. Diliman, Quezon City		_____
Michael Francis Ian G. Vega II, Ph.D. (Adviser) Professor of Physics National Institute of Physics C.S., U.P. Diliman, Quezon City		_____

The rating is therefore           PASSED          .

Sincerely yours,

  
 CRISTINE DLR VILLAGONZALO, Dr.rer.nat.  
 Deputy Director for Academic Affairs, NIP

NATIONAL INSTITUTE OF PHYSICS  
College of Science  
University of the Philippines  
Diliman, Quezon City

ANNOUNCEMENT OF THE UNDERGRADUATE THESIS SEMINAR

of

**JESUS MIGUEL A. YULO II**

on

**DYNAMICS AND STRANGE ATTRACTORS OF STELLAR PULSATION IN ONE-ZONE  
MODELS OF LONG-PERIOD VARIABLE STARS**

In partial fulfillment of the requirements for the degree of

**Bachelor of Science in Physics**

on Monday, 1 June 2022, 2:45 PM

To participate in the online thesis/dissertation defense, please register at:

Zoom link: <https://up-edu.zoom.us/j/98230394167>

Meeting ID: 982 3039 4167

Password: YuloBSDef

THESIS ADVISER

MICHAEL FRANCIS IAN G. VEGA II, Ph.D.

Professor of Physics

National Institute of Physics

C.S., U.P. Diliman, Quezon City

THESIS PANEL MEMBER

ANGELO MARCO A. RAMOSO, M.Sc.

Instructor of Physics

National Institute of Physics

C.S., U.P. Diliman, Quezon City

THESIS PANEL MEMBER

JOHN JAYKEL P. MAGADAN, M.Sc.

Instructor of Physics

National Institute of Physics

C.S., U.P. Diliman, Quezon City

ENDORSED BY:

  
CRISTINE DLR. VILLAGONZALO, Dr.rer.nat.

Deputy Director for Academic Affairs

National Institute of Physics

C.S., U.P. Diliman, Quezon City

AUTHORIZED BY:

  
WILSON O. GARCIA, Ph.D.

Director

National Institute of Physics

C.S., U.P. Diliman, Quezon City

14 May 2022

“Fuck you, Marcos!”

— Walden “Gigachad” Bello

# Acknowledgments

For small creatures such as we  
the vastness is bearable only  
through love.

---

*Ann Druyan*  
*Contact*

I would like to acknowledge and thank the people who have been with me throughout my college life, and who have made this thesis possible.

**Christopher Nolan** for making the movie *Interstellar*. There is a big chance I would not be in this course if that movie had not changed the life of a certain 14 year-old boy.

**My family** for bearing with me being a know-it-all; and for dealing with me whenever I was anti-social while studying and writing this thesis.

**The Gravity Group, and my NIP batchmates** for answering my stupid algebra questions at 2 a.m., and for allowing me to have a very human introduction to the scientific community.

**The UP Debate Society** for letting me be a frustrated nerd in a competitive environment; as well as for all the inumans and shenanigans that defined much of my college experience.

**My ADMU-SHS debate students** who continually show me what a passion for learning can do.

**My friends from high school** who have seen me through it all, especially all the unique circumstances I've had to sing *Pare Ko* and *Burnout* for my continual woes.

**All the professors and teachers** who have never failed to challenge me and believe in me.

**My adviser, Dr. Ian Vega**, for being a constant source of encouragement and scientific insight. But perhaps most especially for reminding us that there is more to life than physics.

And to Volodymyr Zelensky and the show *Servant of the People* for getting me through these hard times.

## ABSTRACT

### DYNAMICS AND STRANGE ATTRACTORS OF STELLAR PULSATION IN ONE-ZONE MODELS OF LONG-PERIOD VARIABLE STARS

Jesus Miguel A. Yulo II  
University of the Philippines (2022)

Adviser:  
Michael Francis Ian G. Vega II,  
Ph.D.

We explore the solutions of two one-zone models of the pulsation of long-period variable stars, which are described by dynamical systems in terms of the radius  $r$ , radial velocity  $v$ , and pressure  $p$ . In the first model, the opacity exponents are taken to be the constants  $n = 1$  and  $s = 3$ . Our novel finding is that this model has an equilibrium curve in the  $(r, v, p)$  phase space parametrized by  $(r, 0, r^{-4})$ . We discovered that phase space trajectories emanating near the conventional fixed point  $(1, 0, 1)$  will tend to spiral towards other fixed points along this curve. The second model, on the other hand, involves dynamically evolving opacity exponents. The presence of these exponents then permit the presence of chaotic solutions. These are of much interest, as many long-period variable stars are known to exhibit chaotic pulsations. The compelling result we discovered for this case is that the non-adiabaticity route to chaos, from variation in the control parameter  $\xi$ , produces a “ $y$ ”-shaped strange attractor in its Lorenz Map for parameter values  $a = 20$  and  $\xi = 0.12$ , that had previously only been seen in the  $\kappa$ -mechanism route to chaos, from variation in the control parameter  $a$ , with parameter values  $a = 13.5$  and  $\xi = 0.08$ . This may mean that long-period variable stars such as S Vul and WY And that had previously been identified as having observational Lorenz Maps corresponding to such “ $y$ ”-shapes, could just as well have these features explained by the non-adiabaticity route to chaos, as from the previously posited  $\kappa$ -mechanism route. In order to further allow for future comparisons of the chaotic solutions of this model to observational data, we performed time-delay embedding reconstructions using both pairs of the parameters corresponding to these “ $y$ ”-shaped Lorenz Maps. We found an optimal delay time  $\tau_{opt} \approx 80$  and minimal embedding dimension  $d_e = 3$ , when the radius  $r$  was used in the reconstruction. When  $v$  was used, we found the optimal values to be  $\tau_{opt} \approx 73$  and  $d_e = 4$ .

PACS: 97.30.-b (Variable stars), 05.45.-a (Nonlinear dynamical systems), 95.10.Fh (Chaos; astronomy)

# Table of Contents

Acknowledgments	ii
Abstract	iii
List of Figures	v
<b>1 Introduction</b>	<b>1</b>
1.1 Long-period variable stars . . . . .	2
1.2 One-zone models . . . . .	4
1.3 Dynamical systems and chaos in the model . . . . .	5
1.4 Statement of the problem . . . . .	6
1.5 Significance of the study . . . . .	6
1.6 Outline of the manuscript . . . . .	6
<b>2 Dynamical systems preliminaries</b>	<b>8</b>
2.1 Defining a dynamical system . . . . .	8
2.2 Phase plots . . . . .	9
2.3 Dynamical systems as vector fields . . . . .	10
2.4 Equilibrium solutions and stability analysis . . . . .	10
2.5 Classification of fixed points . . . . .	13
2.6 Periodicity . . . . .	15
<b>3 Chaotic analysis preliminaries</b>	<b>20</b>
3.1 Conditions for chaos . . . . .	20
3.2 Defining strange chaotic attractors . . . . .	22
3.3 Lorenz Maps . . . . .	23
3.4 Time-delay embedding for attractor reconstruction . . . . .	24
3.5 Finding an optimal delay time $\tau_{opt}$ . . . . .	26
3.6 Choice of embedding dimension $d_e$ . . . . .	28
<b>4 Stellar pulsation in the one-zone models</b>	<b>30</b>
4.1 The $\kappa$ -mechanism . . . . .	31
4.2 Non-adiabaticity . . . . .	32
4.3 Motivation and history of one-zone models . . . . .	34
4.4 Derivation of the one-zone models . . . . .	36
4.5 The Stellingwerf Model . . . . .	41
4.6 The Munteanu Model . . . . .	42

<b>5</b>	<b>Dynamical behavior of the one-zone models</b>	<b>44</b>
5.1	The conventional fixed point . . . . .	44
5.2	Equilibrium solutions of the Stellingwerf model . . . . .	45
5.3	Phase space trajectories in the Stellingwerf model . . . . .	52
5.4	Variation of $\xi$ in the Stellingwerf model . . . . .	57
5.5	Physical considerations and implications of the behavior of the Stellingwerf model . . . . .	58
5.6	Equilibrium solutions and transient behavior of the Munteanu model	60
5.7	Non-adiabaticity period-doubling route in the Munteanu model . . .	63
5.8	$\kappa$ -mechanism period-doubling route in the Munteanu model . . . . .	64
5.9	Physical implications of limit cycles and chaotic solutions in the Munteanu model . . . . .	64
<b>6</b>	<b>Strange attractors of stellar pulsation in the Munteanu model</b>	<b>69</b>
6.1	Period-doubling route to chaos in Lorenz Maps of the pressure $p$ . .	69
6.2	Lorenz Maps of the radial velocity $v$ . . . . .	72
6.3	Time-delay embedding reconstruction of the strange attractors . . .	74
<b>7</b>	<b>Conclusions and further work</b>	<b>83</b>
7.1	Summary and conclusions . . . . .	83
7.2	Recommendations for future work . . . . .	85
	<b>Bibliography</b>	<b>90</b>

# List of Figures

1.1	Hertzsprung-Russell diagram of stellar pulsators. . . . .	2
1.2	The prototype RV Tauri variable RV Tauri (left) and the prototype Mira variable Omicron Ceti (right) taken from the ESO Online Digitized Sky Survey. . . . .	3
1.3	Schematic diagram of a one-zone model. (Not to scale.) . . . . .	4
2.1	Sample trajectory of a 2nd order dynamical system. . . . .	10
2.2	Vectors showing the direction of flow along a trajectory. . . . .	11
2.3	Behavior of fixed points in a two-dimensional phase space. Retrieved from [29]. . . . .	14
2.4	Behavior of fixed points in a three-dimensional phase space. Retrieved from [15]. . . . .	16
2.5	Sample time-series of a state variable $x_1(t)$ showing period-1 and period-2 solutions. . . . .	17
2.6	Sample phase plots of state variables $x_1(t)$ and $x_2(t)$ showing period-1 and period-2 solutions. . . . .	17
2.7	Phase plot of a chaotic solution of the Lorenz system. . . . .	19
3.1	Diagram showing the growth of the separation $\eta(t)$ of two trajectories. . . . .	21
3.2	The Lorenz Map of the Lorenz system for $\sigma = 10, \rho = 28, \beta = \frac{8}{3}$ . Plotted using the <i>Mathematica</i> ® code of Binous et al. (2013) [4]. . . . .	23
3.3	Lorenz Maps of a state variable $x$ showing period-1 and period-2 solutions. . . . .	24
4.1	Diagram of a star using the one-zone model. (Not to scale.) . . . . .	34
5.1	A section of the equilibrium curve $\mathcal{E}$ in phase space. The conventional fixed point $\mathcal{H}$ is shown in green. . . . .	46
5.2	Vector field $(\dot{\mathbf{v}}, \dot{\mathbf{p}})$ on the surface $r = 1$ , for $\xi = 0.08$ . The stable spiral $\mathcal{H}$ is shown in green. . . . .	48
5.3	Vector field $(\dot{\mathbf{v}}, \dot{\mathbf{p}})$ on the surface $r \approx 2.29578$ , for $\xi = 0.08$ . The borderline stable node fixed point of $\mathcal{E}$ on this surface is shown in blue. . . . .	48
5.4	Vector field $(\dot{\mathbf{v}}, \dot{\mathbf{p}})$ on the surface $r \approx 2.34578$ , for $\xi = 0.08$ . The stable node fixed point of $\mathcal{E}$ on this surface is shown in blue. . . . .	49
5.5	Vector field $(\dot{\mathbf{r}}, \dot{\mathbf{v}})$ on the surface $p = 1$ , for $\xi = 0.08$ . The saddle point $\mathcal{H}$ is shown in green. . . . .	50

5.6	Vector field $(\dot{\mathbf{r}}, \dot{\mathbf{p}})$ on the surface $v = 0$ , for $\xi = 0.08$ . A section of $\mathcal{E}$ is shown in blue, and the point $\mathcal{H}$ is marked in green. . . . .	51
5.7	Phase plot of the Stellingwerf model for $\xi = 0.08$ , with initial condition $(0.9986, 0, 0.9986)$ marked in red. The trajectory ends at the point $(0.991654, 0, 1.03409)$ on $\mathcal{E}$ shown in blue. . . . .	53
5.8	Phase plot of the Stellingwerf model for $\xi = 0.08$ , with initial condition $(1.02, 0.1, 0.98)$ marked in red. The trajectory ends at the point $(1.18323, 0, 0.510184)$ on $\mathcal{E}$ shown in blue. . . . .	53
5.9	Phase plot of the Stellingwerf model for $\xi = 0.08$ , with initial condition $(0.97, -0.1, 1.04)$ marked in red. The trajectory ends at the point $(0.865729, 0, 1.78022)$ on $\mathcal{E}$ shown in blue. . . . .	54
5.10	Phase plot of the Stellingwerf model for $\xi = 0.08$ , with initial condition $(0.9, -0.1, 1.1)$ marked in red. The trajectory ends at the point $(0.668043, 0, 5.02092)$ on $\mathcal{E}$ shown in blue. . . . .	54
5.11	Phase plot of the Stellingwerf model for $\xi = 0.08$ , with initial condition $(1.15, 0.1, 0.8)$ marked in red. The trajectory ends at the point $(3.59087, 0, 0.00601451)$ on $\mathcal{E}$ shown in blue. . . . .	55
5.12	Phase plot of the Stellingwerf model for $\xi = 0.08$ , with initial condition $(1.1, 0.1, 1.1)$ marked in red. The trajectory appears to diverge to unphysical values for the radius. . . . .	56
5.13	Phase plots of the Stellingwerf model with initial condition $(0.9986, 0.1, 0.9986)$ marked in red, for varying $\xi$ . Both trajectories shown end at the point $(0.991654, 0, 1.03409)$ on $\mathcal{E}$ . . . . .	57
5.14	Phase plot of the Munteanu model for $\xi = 0.08, a = 20$ , with initial condition near the fixed point $\mathcal{C}$ marked in red. . . . .	61
5.15	Phase plots of the Munteanu model for $\xi = 0.08, a = 20$ with initial conditions near $\mathcal{H}$ showing transient and long-term behavior. The initial condition is shown in red. . . . .	62
5.16	Phase plots of the Munteanu model for $\xi = 0.08, a = 20$ with initial conditions near $\mathcal{B}$ showing transient and long-term behavior. The initial condition is shown in red. . . . .	62
5.17	Trajectories of the Munteanu model for $\xi = 0.08, a = 20$ from near $\mathcal{H}$ (black) and $\mathcal{B}$ (orange) settling onto the same limit cycle for $t \in (2000, 3000)$ . . . . .	63
5.18	Phase plots of the Munteanu model with initial conditions near $\mathcal{H}$ for $a = 20$ , showing a period-doubling route to chaos from variation in $\xi$ . . . . .	65
5.19	Lorenz Map in $p$ of the Munteanu model for parameter values $\xi = 0.08, a = 15$ , showing a period-6 solution. We previously presented this plot in [43]. . . . .	66
5.20	Phase plots of the Munteanu model with initial conditions near $\mathcal{H}$ for $\xi = 0.08$ , showing a period-doubling route to chaos from variation in $a$ . . . . .	67
5.21	Time-series of $r(t)$ and $\ell(t)$ in the Munteanu model showing the corresponding proportionality in their periodicities for $\xi = 0.08, a = 20$ . Here, $t$ is our dimensionless time $t = \omega_* \tau$ . . . . .	68

5.22	Time-series of $r(t)$ and $\ell(t)$ in the Munteanu model showing chaotic oscillations for $\xi = 0.12, a = 20$ . Here, $t$ is our dimensionless time $t = \omega_* \tau$ . . . . .	68
6.1	Lorenz Maps of $p$ of the Munteanu model $a = 20$ , showing a period-doubling route to chaos from variation in $\xi$ . We previously presented these plots in [43]. . . . .	70
6.2	Lorenz Maps of $p$ of the Munteanu model $\xi = 0,08$ , showing a period-doubling route to chaos from variation in $a$ . We previously presented these plots in [43]. . . . .	71
6.3	Lorenz Maps of the radial velocity $v$ showing “ $y$ ”-shaped structures from both routes to chaos. We previously presented these plots in [43].	73
6.4	Plots of average mutual information $I(\tau)$ for the state variables $r$ and $v$ , for the $\kappa$ -mechanism route to chaos: $a = 13.5, \xi = 0.08$ . . . . .	75
6.5	Plots of average mutual information $I(\tau)$ for the state variables $r$ and $v$ , for the non-adiabaticity route to chaos: $a = 20, \xi = 0.12$ . . . . .	76
6.6	Plots of the time-delay embedding reconstruction using the radius $r$ with varying delay time $\tau$ for the $\kappa$ -mechanism route to chaos wherein $a = 13.5, \xi = 0.08$ . . . . .	78
6.7	Plots of the time-delay embedding reconstruction using the radius $r$ with varying delay time $\tau$ for the non-adiabaticity route to chaos wherein $a = 20, \xi = 0.12$ . . . . .	79
6.8	Plots of the time-delay embedding reconstruction using the radial velocity $v$ with varying delay time $\tau$ for the $\kappa$ -mechanism route to chaos wherein $a = 13.5, \xi = 0.08$ . . . . .	80
6.9	Plots of the time-delay embedding reconstruction using the radial velocity $v$ with varying delay time $\tau$ for the non-adiabaticity route to chaos wherein $a = 20, \xi = 0.12$ . . . . .	81

# Chapter 1

## Introduction

Twinkle, twinkle, little star,  
How I wonder what you are!

---

*Jane Taylor*  
*The Star*

Looking up at the night sky, it is easy to become mesmerized by a plethora of twinkling points of light. This apparent twinkling, however, is not a feature of stars themselves, but is rather an aberration of their light as it passes through the Earth's atmosphere. That said, nature does rescue our childhood nursery rhyme though with the existence of variable stars. These are stars that exhibit variations in their brightness over time because of the physical processes ruling their dynamics.

Variable stars, or stellar pulsators, have been indispensable to astronomy since their first discovery centuries ago. The most popular variable stars, the classical Cepheids, exhibit regular periodic pulsations. Cataloguing observations of these stars led Henrietta Swan Leavitt to notice that the brighter Cepheids also had correspondingly longer periods of pulsation. Thus, by recording their pulsational periods, the absolute magnitude and apparent magnitudes of luminosity could then be easily calculated. This has led to classical Cepheids being dubbed “standard candles” as they serve as metrics of distance when surveying the heavens [8].

While classical Cepheids have pulsational periods on the order of a few days or a few weeks, some classes of variable stars have been observed to exhibit luminosity variations with periods on the order of months. These long-period variable (LPV) stars have been of much interest in recent decades due to complicated features present in their luminosity time-series (light curves). Since these are intrinsic variables, meaning that their oscillations are not due to the gravitational influence of a binary partner or

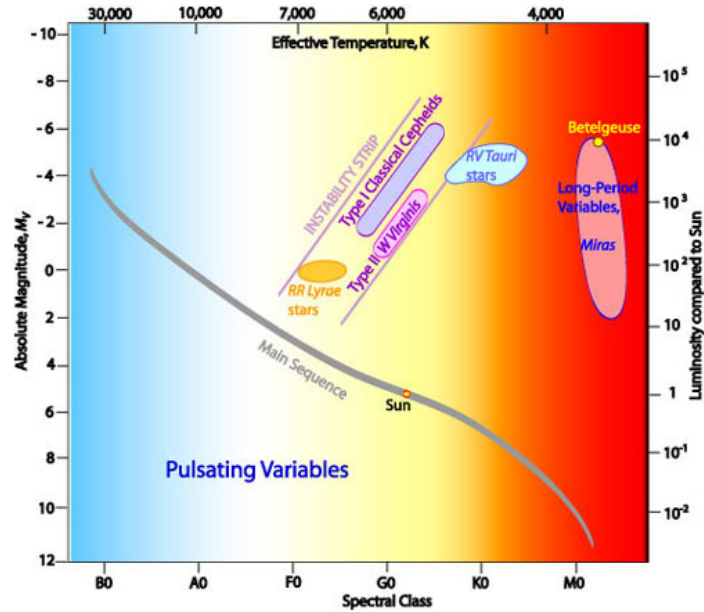


Figure 1.1: Hertzsprung-Russell diagram of stellar pulsators.

the transit of an exoplanet, the study of their pulsations may have much to say about the physical processes present within these stars. In fact, certain LPVs have even been known to exhibit irregular or even chaotic oscillations. The ability to model and extract physical insight from these perplexing behaviors thus breeds much enthusiasm for their study.

## 1.1 Long-period variable stars

While there is some debate and disagreement over exactly what subclasses of pulsating stars fall under the definition of long-period variable stars, we consider the classification used by the American Association of Variable Star Observers (AAVSO) [33]. This includes some pulsators from the red and yellow giant and supergiant classes such as RV Tauris, Miras, and Semiregular variables. As such, these stars are old and relatively cool, as can be seen from the RV Tauri and Mira variables in the Hertzsprung-Russell diagram in Figure 1.1 <sup>1</sup>.

Since these stars are found on the Asymptotic Giant Branch (AGB) and post-Asymptotic Giant Branch (post-AGB) of their evolutionary tracks, they feature nuclear fusion of heavier elements. Specifically, these stars have helium-burning shells in addition to hydrogen-burning shells surrounding a carbon-rich core [28]. This fusion

<sup>1</sup>HR diagram retrieved from: [https://www.atnf.csiro.au/outreach/education/senior/astrophysics/variable\\_pulsating.html](https://www.atnf.csiro.au/outreach/education/senior/astrophysics/variable_pulsating.html).

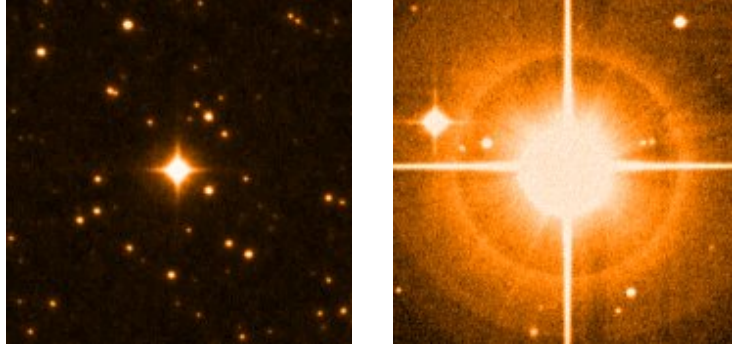


**Figure 1.2:** The prototype RV Tauri variable RV Tauri (left) and the prototype Mira variable Omicron Ceti (right) taken from the ESO Online Digitized Sky Survey.

of heavier elements is an indicator that these are dying stars that are in the final stages of their evolutionary processes, before they transition into becoming white dwarfs and planetary nebulae. There is thus some existential significance in studying these geriatric stars, as the physical processes governing them are what create and form future generations of stars and planets. In a way then, Dylan Thomas might say that long-period variables are stars raging against the dying of the light <sup>2</sup>.

While these stars may extend to up to thousands of times the size of the Sun, these are in fact stars of low or intermediate mass. Their masses range from below  $1 M_{\odot}$  to around  $10 M_{\odot}$ , where  $M_{\odot}$  represents the mass of the Sun. Prototypes of RV Tauri and Mira variables can be seen in Figure 1.2 <sup>3</sup>. The star RV Tauri is a post-AGB yellow supergiant, while Omicron Ceti is an AGB red giant.

The luminosity variations exhibited by these stars are thought to be due to the instabilities and opacity variations present from the layering of different nuclear burning and ionization zones. It is important to note that the luminosity variations are not just a dimming and brightening of the stars alone, but also correspond to contractions and expansions of the stellar surface.

Although LPVs are classified based on their having luminosity variations with periods of a few dozen days to upwards of 1000 days, there is in fact much debate over how to even define a period for these stars due to their often irregular oscillations. For many LPVs, a characteristic feature of their light curves is the presence of alternating deep and shallow minima [5, 19]. Thus, some choose to define the period of variation as the time between successive deep minima [28]. However, these still are often not

<sup>2</sup>Referring to the poem *Do not go gentle into that good night* by Dylan Thomas.

<sup>3</sup>RV Tauri and Omicron Ceti images retrieved from the ESO Online Digitized Sky Survey: <https://archive.eso.org/dss/dss>.

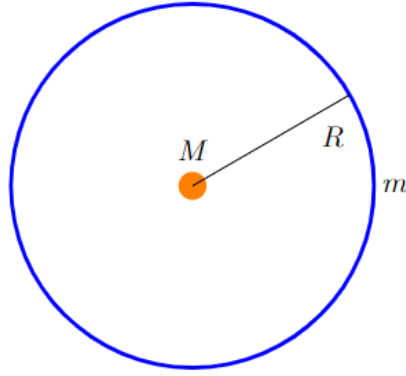


**Figure 1.3:** Schematic diagram of a one-zone model. (Not to scale.)

uniform enough to define a clear periodicity. For some of these variables, the discovery of low-dimensional chaos in their oscillations has proved fruitful for further analysis and modelling [7].

## 1.2 One-zone models

The question then becomes how it is best to model these stars and their pulsations. The answer to this question depends upon the kind of information one wishes to extract from the modelling. One route is through detailed hydrodynamic codes that take into account the specific layering of nuclear burning and ionization zones within the star. While the results from these may be robust, it may be difficult to extract intuitive physical insight into what exactly is causing certain features of the stellar oscillations.

Another route is to consider simple toy models with a minimal number of moving parts, which can serve as a pedagogical tool for insight into the physical processes in these stars. This method still allows for an assessment of the effects of changing certain global parameters such as the adiabatic coefficient, the form of the opacity law, etc. These models can then be stated in terms of sets of nonlinear differential equations. Using a dynamical systems approach then, the irregular features of the oscillations of these stars such as low-dimensional chaos may be assessed [6].

One class of models in line with the latter approach are the one-zone models of stellar pulsators first put forward by Baker (1966) [2]. In this model, we have what is essentially a point mass  $M$  containing much of the stellar mass surrounded by a thin spherical shell of mass  $m$ , with radial extension  $R$ , representing the “surface” of the

star. The processes within the star then result in a pressure  $P$  acting on the shell.

When writing down Newton's 2nd Law for a star, we usually use Euler's Equation for a continuous mass distribution given by

$$\rho \frac{d^2 \mathbf{R}}{d\tau^2} = \rho \nabla U - \nabla \mathbf{P}, \quad (1.1)$$

where  $U$  is the gravitational potential,  $\rho$  is the density, and  $\tau$  is time. However, since the one-zone model involves two discrete masses instead of a continuous mass distribution, we are able to simplify this to

$$m \frac{d^2 R}{d\tau^2} = -\frac{GMm}{R^2} + 4\pi R^2 P. \quad (1.2)$$

In this study, we only consider radial oscillations, so the force from the pressure  $P$  takes this spherically symmetric form. The equations of motion of the stellar surface then all flow from Equation (1.2), after the form of the pressure  $P$  is specified from a stellar energy equation.

### 1.3 Dynamical systems and chaos in the model

In understanding the temporal behavior of a star described by a one-zone model, it is useful to use a dynamical systems approach. Through this, equations of motion may be written down for the system through a set of nonlinear ordinary differential equations (ODEs) describing the temporal evolution of the radius, radial velocity, and pressure of the star.

Since these equations are nonlinear, finding analytic or closed-form solutions is often impossible or unwieldy. The dynamical systems approach makes use of numerical integration to survey the temporal evolution of the system of ODEs [40]. Through phase plots, the long term behavior of the variables may be assessed through qualitative analysis giving insight into periodicity, asymptotic behavior, chaos, among others.

Due to the purported presence of low-dimensional chaos in the oscillations of long-period variable stars, the ability of one-zone models to render chaotic solutions is of keen interest. Since chaos would appear as non-repeating non-random patterns in time-series of variables, the ability to characterize the geometric properties of the strange chaotic attractors of the system requires numerous mathematical tools such as Lorenz maps, time-delay embeddings, Lyapunov exponents, and others [17, 22, 27].

## 1.4 Statement of the problem

While one-zone models are relatively simple, the ability to tune certain physical parameters allows for a wide range of possible behaviors of the stellar pulsation.

We first consider a one-zone model wherein the opacity exponents are constants. We seek to determine the possible final states of a star after a small perturbation from equilibrium.

We then probe the long-term behavior of the system when the opacity exponents are no longer constants, but are instead dynamical functions of the radius and pressure. Two different period-doubling routes to chaos are explored. One is from variation in the control parameter  $a$  controlling the strength of the  $\kappa$ -mechanism, and the other derives from variation in  $\xi$  controlling the amount of non-adiabaticity.

It then becomes pertinent to characterize and compare the strange chaotic attractors from both routes to chaos. We seek to find if there are any similarities or generic features of the chaos deriving from these two different physical processes. This is done via the use of Lorenz maps and time-delay reconstruction of the attractors.

## 1.5 Significance of the study

Since long-period variable stars do not exhibit pulsations as regular as other variable stars like classical Cepheids, the ability to shed more light on some of the physical processes governing their behavior is of much importance. We hope to contribute to the use of one-zone models as instructive pedagogical tools in the examination of these twinkling lights in the sky.

Furthermore, since observations of these stars from amateur astronomers or even space telescopes may only give time-series of one or a few physical variables, the features of chaotic variability may be difficult to interpret. Through the use of Lorenz maps and time-delay reconstructions, fundamental features of the strange attractors are revealed using only one physical variable. It is then possible for these results to potentially be compared to new observational data from observations of these stars.

## 1.6 Outline of the manuscript

This work is split into seven chapters. In Chapter 2, we develop the preliminaries of the dynamical systems approach that is used to analyze the temporal evolution of

the system. Next, the mathematical toolbox for chaotic analysis is expounded upon in Chapter 3. We then motivate the one-zone models and the physical processes that they describe in Chapter 4. The dynamical behavior of the one-zone models is the subject of Chapter 5. Chapter 6 deals with the analysis of the strange chaotic attractors of the model that features dynamically evolving opacity exponents. Lastly, we state our conclusions and insights into possible future work in Chapter 7.

# Chapter 2

## Dynamical systems preliminaries

That is why man cannot be happy:  
happiness is the longing for repetition.

---

*Milan Kundera*  
*The Unbearable Lightness of Being*

While writing Newton's 2nd Law for a one-zone model as in Equation 1.2 may seem deceptively simple, once we specify the pressure  $P$  via a stellar energy equation, it becomes apparent that the differential equations governing the system become highly nonlinear. This means that a closed form solution describing the temporal evolution of the star is unlikely or even impossible. This then merits the use of a dynamical systems approach wherein we numerically integrate the set of differential equations describing the equations of motion of the system. Through phase plots, we can visualize the trajectories the variables describing the system take over time [16]. This leads us to qualitative insights into the long-term behavior of the stars described by the one-zone models.

In this chapter, we present an introduction to the language of dynamical systems. A more comprehensive development of the topic can be found in many well-established reference textbooks [12, 16, 40].

### 2.1 Defining a dynamical system

The definition of dynamical systems includes both iterated maps which are discrete, and systems of differential equations which are continuous [40]. For the purposes of this work, we will deal mostly with the latter.

We define our dynamical system in general by a set of  $d$  ordinary differential

equations

$$\begin{aligned}\dot{x}_1 &= f_1(x_1, \dots, x_d) \\ &\vdots \\ \dot{x}_d &= f_d(x_1, \dots, x_d).\end{aligned}\tag{2.1}$$

Here, we use dot notation to indicate a derivative with respect to our dimensionless time  $t$  as

$$\dot{x}_j = \frac{dx_j}{dt},\tag{2.2}$$

and our index runs from

$$j = 1, \dots, d.\tag{2.3}$$

It should be noted that the functions  $f_j$  show no explicit dependence on our dimensionless time  $t$ , and only depend on our state variables  $x_1, \dots, x_d$ . Thus, we may call our system an  $d$ -th order<sup>1</sup> or  $d$ -dimensional autonomous system. A system with an explicit time dependence would be considered non-autonomous. The analysis in this work is confined to autonomous differential equations, so we will not spend further time developing ideas for non-autonomous systems.

## 2.2 Phase plots

The state of a dynamical system tells you the values of the state variables at a particular time. For example, for an initial time  $t_0$ , our system would be in the state of initial conditions  $(x_1(t_0), \dots, x_d(t_0))$ . A state at a later time  $t_1$  would then similarly be written as  $(x_1(t_1), \dots, x_d(t_1))$ . If we trace out the curve connecting these two states, we would have a trajectory of the system [16]. We get this trajectory by simultaneously solving the differential equations in our system. For our purposes, we use numerical integration to achieve this.

This trajectory is part of what is called a phase plot or phase portrait, and it is drawn in what we call phase space. The number of dimensions of the phase space is equal to the order of our dynamical system. For example, a 2nd order dynamical system would have a 2-dimensional phase space. In Figure 2.1, we show a sample trajectory for such a system in a 2-dimensional phase space.

An important thing to note is that trajectories of a particular dynamical system cannot cross. This is guaranteed by the Existence and Uniqueness Theorems [40].

---

<sup>1</sup>This is not to be confused with the order of an ODE, which indicates the order of the derivative.

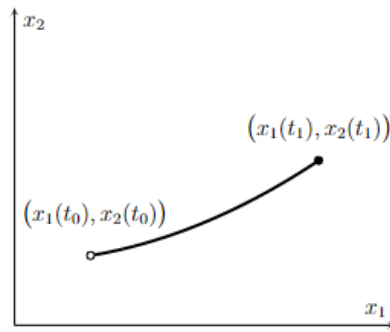


**Figure 2.1:** Sample trajectory of a 2nd order dynamical system.

This means that the choice of initial conditions uniquely determines the temporal evolution of the dynamical system.

## 2.3 Dynamical systems as vector fields

Dynamical systems are also thought of by considering the “flow” of trajectories. The natural way to visualize this would be through the use of vector fields in the phase space. We can thus recast our dynamical system from Equation 2.1 as a vector equation

$$\dot{\mathbf{x}} = \mathbf{f}(\mathbf{x}). \quad (2.4)$$

In this form, we have

$$\mathbf{x} = (x_1, \dots, x_d) \quad (2.5)$$

$$\mathbf{f}(\mathbf{x}) = (f_1(\mathbf{x}), \dots, f_d(\mathbf{x})). \quad (2.6)$$

Using this, we can assign a vector to each point along a trajectory in a phase portrait that points along the direction of the flow. This allows us to get qualitative insight into how the state variables of the system are tending to behave in a particular region of the phase space. In Figure 2.2, we show some of the vectors indicating the direction of the flow along our sample trajectory.

## 2.4 Equilibrium solutions and stability analysis

Now that we have established a means to understand flow in a dynamical system, it is important to consider states of the system where the flow becomes zero

$$\dot{\mathbf{x}} = 0. \quad (2.7)$$

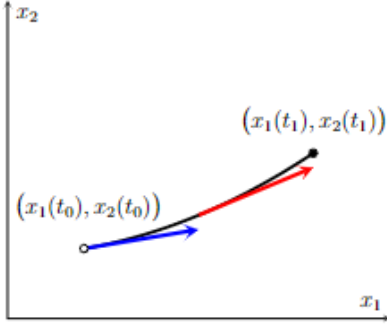


**Figure 2.2:** Vectors showing the direction of flow along a trajectory.

In phase space, these equilibrium solutions can be points, curves, or even planes in higher dimensions. When these solutions are simply points, we call them fixed points. We define these fixed points as

$$\mathbf{x}^* = (x_1^*, \dots, x_d^*), \quad (2.8)$$

which satisfy

$$\mathbf{f}(\mathbf{x}^*) = 0. \quad (2.9)$$

While once a trajectory reaches a point on an equilibrium solution, it stays there forever, it is of much interest to consider the qualitative behavior of the flow around a small displacement from the equilibrium solution. This is where stability analysis comes in. In crude terms, when trajectories around such a point tend to move towards it, we consider the point as stable. When trajectories tend to move away from it, we call it unstable. There are numerous ways to classify such equilibrium solutions, and we will discuss one of them here.

When the equilibrium solution is a fixed point, we can perform a linearization about it. We conduct our linear stability analysis by first defining a small displacement away from the fixed point as

$$\boldsymbol{\eta} = \mathbf{x} - \mathbf{x}^*. \quad (2.10)$$

Since  $\mathbf{x}^*$  simply contains constant entries, differentiating  $\boldsymbol{\eta}$  with respect to  $t$  just yields

$$\dot{\boldsymbol{\eta}} = \dot{\mathbf{x}} = \mathbf{f}(\mathbf{x} + \boldsymbol{\eta}). \quad (2.11)$$

We can then perform a Taylor expansion of this to get

$$\mathbf{f}(\mathbf{x} + \boldsymbol{\eta}) = \mathbf{f}(\mathbf{x}^*) + \left. \frac{\partial \mathbf{f}}{\partial \mathbf{x}} \right|_{\mathbf{x}=\mathbf{x}^*} \boldsymbol{\eta} + O(\boldsymbol{\eta}^2). \quad (2.12)$$

Clearly by Equation 2.9, the first term vanishes. We further disregard higher order terms as negligible [40]. This then allows us to simplify this to

$$\mathbf{f}(\mathbf{x} + \boldsymbol{\eta}) = \left. \frac{\partial \mathbf{f}}{\partial \mathbf{x}} \right|_{\mathbf{x}=\mathbf{x}^*} \boldsymbol{\eta}. \quad (2.13)$$

We can then define the Jacobian matrix, which is a matrix containing first partial derivatives of our functions  $f_i$  with respect to the state variables. This is written as

$$\mathbf{J} = \begin{pmatrix} \frac{\partial f_1}{\partial x_1} & \frac{\partial f_1}{\partial x_2} & \dots & \frac{\partial f_1}{\partial x_d} \\ \frac{\partial f_2}{\partial x_1} & \frac{\partial f_2}{\partial x_2} & \dots & \frac{\partial f_2}{\partial x_d} \\ \frac{\partial f_3}{\partial x_1} & \frac{\partial f_3}{\partial x_2} & \dots & \frac{\partial f_3}{\partial x_d} \\ \vdots & \vdots & \ddots & \vdots \\ \frac{\partial f_d}{\partial x_1} & \frac{\partial f_d}{\partial x_2} & \dots & \frac{\partial f_d}{\partial x_d} \end{pmatrix}_{(x_1^*, \dots, x_d^*)}. \quad (2.14)$$

This then allows us to rewrite Equation (2.11) as

$$\dot{\boldsymbol{\eta}} = \mathbf{J}\boldsymbol{\eta}. \quad (2.15)$$

It now becomes evident that we can treat this as an eigenvalue problem. We can find solutions for  $\boldsymbol{\eta}$  as a linear combination including the eigenvalues of eigenvectors of  $\mathbf{J}$ . This can be written as

$$\boldsymbol{\eta}(t) = \sum_{i=1}^n C_j \mathbf{v}_j e^{\lambda_j t}, \quad (2.16)$$

where  $\lambda_j$  are the eigenvalues,  $\mathbf{v}_j$  are the eigenvectors, and  $C_j$  are constant coefficients.

We can see that it is the eigenvalues that determine the growth of the initial displacement from equilibrium. In general, the eigenvalues are complex quantities, and we can thus split them into their real and imaginary parts as

$$\lambda_j = \alpha_j + i\mu_j. \quad (2.17)$$

This allows us to restate the exponential in Equation 2.16 as

$$e^{\lambda_j t} = e^{\alpha_j t} e^{i\mu_j t}. \quad (2.18)$$

It is useful to recast this using Euler's formula as

$$e^{\lambda_j t} = e^{\alpha_j t} (\cos(\mu_j t) + i \sin(\mu_j t)). \quad (2.19)$$

Stating the exponential in this form then more intuitively reveals to us that the real part  $\alpha_j$  determines the growth of the initial displacement  $\boldsymbol{\eta}$  from equilibrium. If  $\alpha_j$  is positive, we expect the displacement to grow larger. We then expect the displacement to shrink if it is negative. The imaginary part  $\mu_j$  on the other hand governs its oscillatory behavior [34].

Going back to the idea of flow, a shrinking perturbation  $\boldsymbol{\eta}$  would entail that trajectories tend to move toward the fixed point, rendering it stable. A growing displacement would then mean trajectories tend to move away from the fixed point, making it unstable [34].

An important question to ask is what role the eigenvectors  $\mathbf{v}_j$  play in this. The eigenvectors in fact determine the direction of the stability or instability that we assess from their corresponding eigenvalues. Since we have  $d$  eigenvalues and eigenvectors for a  $d$ -dimensional Jacobian  $\mathbf{J}$ , we would be assessing the stability along  $d$  directions.

While it is a powerful tool for many fixed points, there are limits to linear stability analysis. For example, we may have cases wherein there exists an eigenvalue that has a zero real part or is even entirely zero. It then becomes impossible to determine from Equation 2.19 if we expect a growing or shrinking perturbation.

Another case to consider is when the equilibrium solution is not just a fixed point but is a curve, a plane, or some other kind of surface. Since this case would imply each equilibrium point has an adjacent equilibrium point in some direction, we have to resort to other means of analysis such as plotting the vector field near such equilibrium solutions.

## 2.5 Classification of fixed points

Now that we have discussed the process by which we conduct linear stability analysis, we now present the classification of such fixed points.

We first begin our discussion for fixed points in a two-dimensional dynamical system. The eigenvalues of a two-dimensional Jacobian can directly be solved for by calculation of the trace  $Tr(\mathbf{J})$  and the determinant  $Det(\mathbf{J})$  [40]. These eigenvalues are found using

$$\lambda_{1,2} = \frac{1}{2} \left( Tr(\mathbf{J}) \pm \sqrt{Tr(\mathbf{J})^2 - 4Det(\mathbf{J})} \right). \quad (2.20)$$

Using this equation then, we can then classify fixed points based on the resulting form of the eigenvalues. In Table 2.1, we present the classification of such fixed points.

$Det(\mathbf{J}) < 0$	$Det(\mathbf{J}) > 0$				
Saddle Point	$Tr(\mathbf{J}) = 0$	$Tr(\mathbf{J})^2 - 4Det(\mathbf{J}) > 0$		$Tr(\mathbf{J})^2 - 4Det(\mathbf{J}) < 0$	
	Center	$Tr(\mathbf{J}) < 0$	$Tr(\mathbf{J}) > 0$	$Tr(\mathbf{J}) < 0$	$Tr(\mathbf{J}) > 0$
		Stable Node	Unstable Node	Stable Spiral	Unstable Spiral

**Table 2.1:** Classification of fixed points in a two-dimensional phase space.

Type of Fixed Point	Behavior of Trajectories
<b>Saddle Point</b>	Attracted in some directions, repelled in others
<b>Center</b>	Neither attracted nor repelled
<b>Stable Node</b>	Attracted
<b>Unstable Node</b>	Repelled
<b>Stable Spiral</b>	Spiral towards it
<b>Unstable Spiral</b>	Spiral away from it

**Table 2.2:** Behavior of trajectories around fixed points in a two-dimensional phase space.

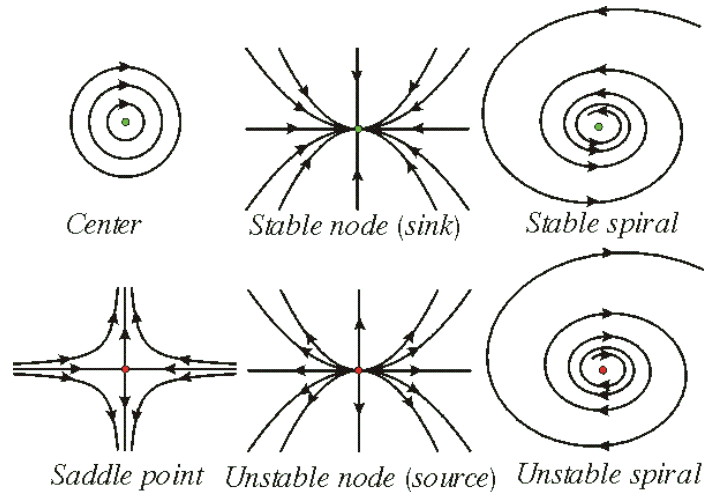


**Figure 2.3:** Behavior of fixed points in a two-dimensional phase space. Retrieved from [29].

The subsequent descriptions of the behavior of trajectories around such fixed points can be found in Table 2.2 and Figure 2.3 [29].

Moving on to fixed points in a three-dimensional dynamical system, the form of the eigenvalues cannot as easily be determined from the trace and the determinant. We must explicitly evaluate the results of the three-dimensional Jacobian, and base our classification on the signs of the real  $\alpha_j$  and imaginary  $\mu_j$  parts of the eigenvalues. Furthermore, the added dimension makes the three-dimensional cases more complex.

Form of eigenvalues	Classification	Behavior of trajectories
$\alpha_{1,2,3} < 0, \mu_{1,2,3} = 0$	<b>Stable Node</b>	Attracted
$\alpha_{1,2,3} > 0, \mu_{1,2,3} = 0$	<b>Unstable Node</b>	Repelled
$\mu_{1,2,3} = 0, \alpha_1 > 0 \wedge \alpha_2 < 0 \wedge \alpha_3 \neq 0$	<b>Saddle</b>	Attracted in some directions, repelled in others
$\mu_1 = 0 \wedge \mu_{2,3} \neq 0, \alpha_{1,2,3} < 0$	<b>Stable Focus-Node</b>	Attracted in some directions, spirals towards in some other directions
$\mu_1 = 0 \wedge \mu_{2,3} \neq 0, \alpha_{1,2,3} > 0$	<b>Unstable Focus-Node</b>	Repelled in some directions, spirals away in some other directions
$\mu_1 = 0 \wedge \mu_{2,3} \neq 0, \alpha_1 > 0 \wedge \alpha_{2,3} < 0$	<b>Saddle-Focus</b>	Attracted in some directions, spirals away in some other directions
$\mu_1 = 0 \wedge \mu_{2,3} \neq 0, \alpha_1 < 0 \wedge \alpha_{2,3} > 0$	<b>Saddle-Focus</b>	Repelled in some directions, spirals towards in some other directions

**Table 2.3:** Behavior of trajectories around fixed points in a three-dimensional phase space.

For example, the focus-node acts like a spiral in some directions, and like a node in others.

We present the classification of fixed points in a three-dimensional phase space and their corresponding behaviors in Table 2.3. These are visualized in Figure 2.4 [15].

While there are other forms of fixed points called non-hyperbolic equilibria, these often require higher order terms in the Taylor expansion in Equation 2.12 [15]. We will therefore not present them here, as the systems we are studying do not exhibit such fixed points anyway.

## 2.6 Periodicity

Often in dynamical systems, we find solutions wherein the trajectories are repeating or periodic. This can be stated as

$$\mathbf{x}(t) = \mathbf{x}(t + \Pi), \quad (2.21)$$

for some period  $\Pi$ .

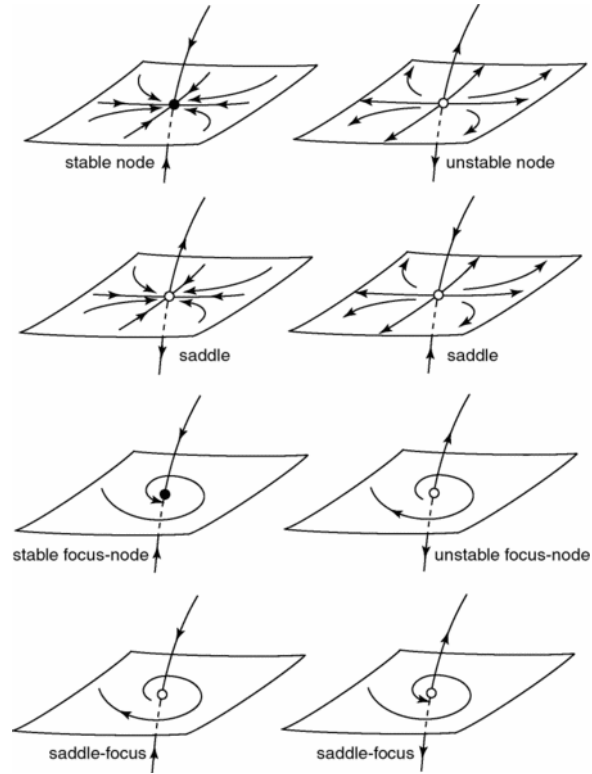


**Figure 2.4:** Behavior of fixed points in a three-dimensional phase space. Retrieved from [15].

This repeating pattern can be seen when we plot a time-series of one of the state variables. In analyzing such periodic solutions, it is also pertinent to pay attention to some of the features of the oscillations. Thus, we have the concept of “counting” the periodicity of such solutions. If in each repeating cycle, we have one maxima, we call this period-1. When we have two maxima per cycle, this is period-2, and so on and so forth. In Figure 2.5, we show sample period-1 and period-2 time-series for some state variable  $x_1(t)$ .

Periodicity can also be visualized via phase plots. In phase plots, these periodic solutions take the form of limit cycles. Limit cycles are isolated periodic solutions, meaning that nearby trajectories either move toward or away from limit cycles. This means that these nearby trajectories aren’t closed [40].

We can also count the periodicity when viewing a phase plot. Instead of counting the number of maxima per cycle as in a time-series, we count the number of rings making up the limit cycle structure. This can be seen in Figure 2.6, wherein we have 1 ring for the period-1 case, and 2 rings for the period-2 case.

It is important to note that it may take some time for trajectories emanating

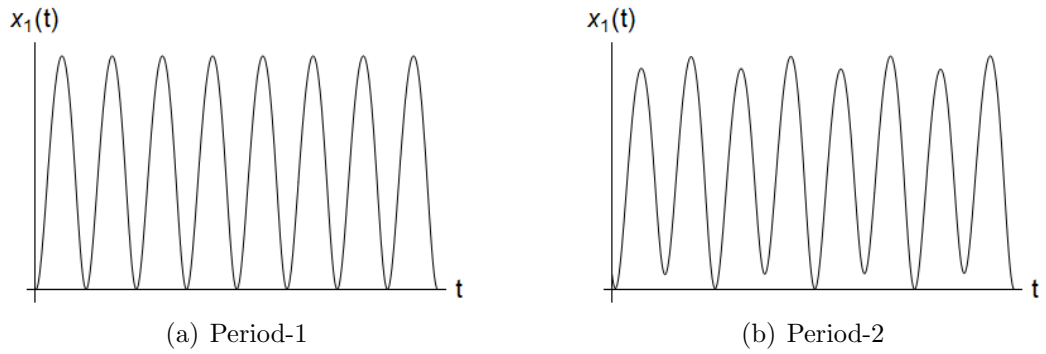


**Figure 2.5:** Sample time-series of a state variable  $x_1(t)$  showing period-1 and period-2 solutions.

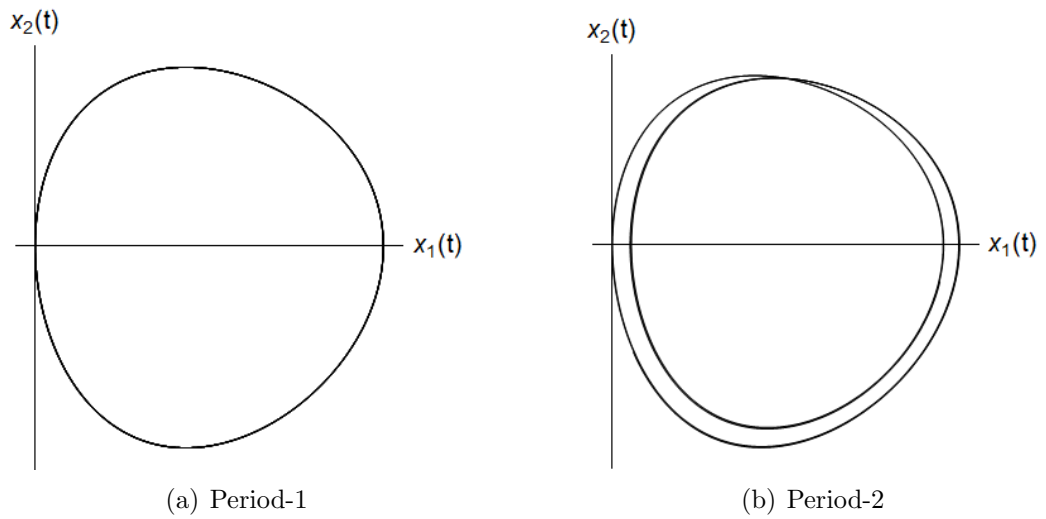


**Figure 2.6:** Sample phase plots of state variables  $x_1(t)$  and  $x_2(t)$  showing period-1 and period-2 solutions.

from some initial conditions to settle onto a limit cycle. It is expected for there to be transient behavior in the phase plot that may not be periodic, before trajectories settle onto the limit cycle.

An important phenomenon we will be exploring later on in this work is the period-doubling route to chaos. This is the process by which the variation of a parameter or coefficient, in one or more of the differential equations making up the dynamical system, leads to period doubling.

For example, let's say we have a parameter  $\sigma$ . When  $\sigma = \sigma_1$ , we have a period-1 limit cycle solution. After we increase this to some value  $\sigma_2$ , and re-solve the differential equations, we end up with a period-2 solution. This cascade goes on as we continue varying  $\sigma$ , and get period-4, period-8, and period-16 solutions and so on until at some critical value of  $\sigma$  we end up in a chaotic regime.

Chaotic solutions manifest as non-repeating non-random oscillations in time-series. Thus, chaos is aperiodic. In phase plots, chaotic solutions can appear as trajectories seeming to densely occupy some region of the phase space.

Perhaps the most famous example of a chaotic system is Edward Lorenz's attractor [21]. This dynamical system, which was constructed as a simple weather model, is made up of the three ordinary differential equations given by

$$\begin{aligned} \dot{x} &= \sigma(y - x) \\ \dot{y} &= x(\rho - z) - y \\ \dot{z} &= xy - \beta z. \end{aligned} \tag{2.22}$$

In Figure 2.7, we plot a chaotic solution to the Lorenz equations with parameter values  $\sigma = 10$ ,  $\rho = 28$ , and  $\beta = \frac{8}{3}$ . This visualization can help give an idea of the kinds of complicated structures chaotic solutions may yield. This particular solution seems to resemble the wings of a butterfly, and it is how Edward Lorenz came up with the moniker of the "Butterfly Effect" to describe the sensitive dependence to initial conditions inherent to chaos.

Looking at Figure 2.7, it may seem that trajectories cross themselves in phase space. However, this is not the case, as guaranteed by the Existence and Uniqueness Theorems. It may just appear that way due to the limited resolution of computer graphics.

As we have now established the language of dynamical systems, and given an introduction to the concept of chaos, we can now move on to establishing mathematical

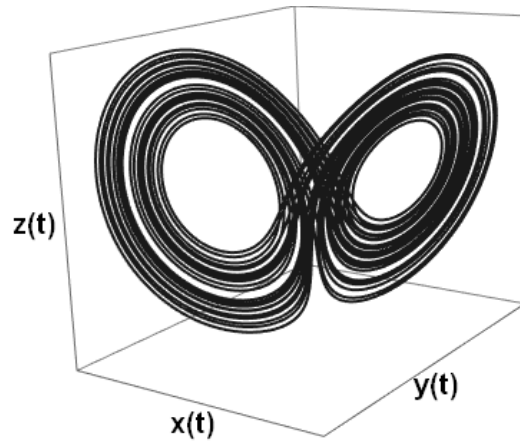


**Figure 2.7:** Phase plot of a chaotic solution of the Lorenz system.

tools that can be used to analyze chaos on a deeper level in the next chapter.

# Chapter 3

## Chaotic analysis preliminaries

Chaos, yet harmony.

---

*The Jedi Code*

With chaotic solutions having previously been found in one-zone models, it becomes pertinent to understand precisely what chaos is and how to analyze it [26, 37]. While chaos is often mistakenly associated with randomness, it is in fact explicitly non-random. It may just appear that way since chaotic dynamics are often very complex, and their analysis requires the use of mathematical techniques that may be unfamiliar.

This chapter is dedicated to developing the mathematical toolbox to analyze strange chaotic attractors. Once again, a more expansive discussion may be found in select textbooks [17, 22, 27].

### 3.1 Conditions for chaos

While there is some disagreement about exact definitions of what precisely determines whether or not a system is chaotic, there are some generally accepted features. For the purposes of this work, we base our working assumptions of what chaos is on Strogatz (2018) [40].

The definition of deterministic chaos presented by Strogatz has three primary conditions. Firstly, chaotic behavior is aperiodic. This means that there is the presence of trajectories which do not repeat, or settle down to some particular value [40]. For example, a limit cycle trajectory could not be considered chaotic, as this is periodic by definition. This is not to say that a chaotic dynamical system cannot have some

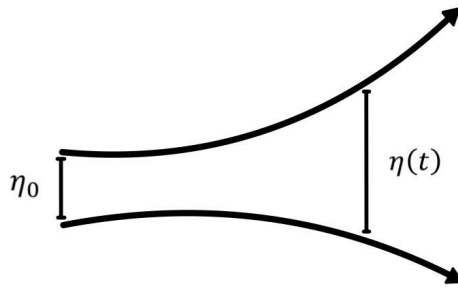


**Figure 3.1:** Diagram showing the growth of the separation  $\eta(t)$  of two trajectories.

trajectories that settle down to a particular value or limit cycle. It is just that there must be a significant number of trajectories in phase space that do not exhibit such regular behavior.

Secondly, the system must be deterministic. This requires that the system is non-random or not noisy [40]. It also means that given exact precise numbers specifying parameters and initial conditions, we should be able to predict the precise state of a trajectory after some time  $t$ .

Thirdly, the system must exhibit a sensitive dependence on initial conditions. This entails that trajectories in phase space starting out with initial conditions very close to one another, will eventually diverge from one another at an exponential rate [40].

This condition of exponential divergence is usually quantified using the concept of the Lyapunov exponent  $\Lambda$ . To illustrate this concept, we may imagine two trajectories emanating from initial conditions that are separated from each other by some minuscule distance  $\eta_0$ , as shown in Figure 3.1. After some time  $t$ , the magnitude of the separation  $\eta(t)$  between the two trajectories can be calculated as

$$\|\eta(t)\| \approx \|\eta_0\| e^{\Lambda t}. \quad (3.1)$$

We can thus solve for the Lyapunov exponent after some time  $t$  as

$$\Lambda \approx \frac{1}{t} \ln \left( \frac{\|\eta(t)\|}{\|\eta_0\|} \right). \quad (3.2)$$

Thus, when  $\Lambda > 0$ , the growth of the separation is exponentially increasing. This would thus be a requirement for chaos.

It is important to note that for a given  $d$ -dimensional dynamical system, we would actually need to measure  $d$  Lyapunov exponents. For example, for three-dimensional systems, we would in fact have 3 Lyapunov exponents. However, for chaos, we only

require that the largest of the Lyapunov exponents be positive. This is what is called the maximal Lyapunov exponent.

## 3.2 Defining strange chaotic attractors

Once again, there is no universal agreement on what precisely defines a strange chaotic attractor. We will once more refer to Strogatz (2018) for the definitions we will be considering [40].

This definition is made up of three prongs. For convenience, let us consider a strange attractor  $S$ . Firstly,  $S$  is invariant, meaning that trajectories that begin in  $S$  cannot leave it [40].

Secondly,  $S$  attracts an open set  $I$  of initial conditions sufficiently near it. This means that trajectories emanating from within  $I$  will tend to  $S$  as  $t \rightarrow \infty$  [40].

Lastly,  $S$  must exhibit the sensitive dependence on initial conditions outlined earlier [40]. This means that there must be trajectories within  $S$  that have positive maximal Lyapunov exponents.

Other features of strange chaotic attractors spring from these conditions. Attractors are called strange when they exhibit fractal structure or fractional dimensions [42]. For example, while a fixed point may be an attractor, it has zero dimension. A strange attractor would have a non-integer dimension.

This fractal structure can be difficult to visualize. This is why trajectories in phase space for chaotic systems such as the Lorenz system we showed in Figure 2.7 can look very complicated. This is because the underlying strange attractor governing the dynamics exhibits such a fractal structure. Thus, it is through other means of visualizations, such as the Lorenz Maps that we will discuss in the next section, that we are able to probe some features of the strange attractors.

It is also interesting to note that it is possible to have a strange attractor that is not chaotic. These are called strange non-chaotic attractors (SNAs). These are strange attractors which do not exhibit a sensitive dependence on initial conditions, and thus do not have a positive maximal Lyapunov exponent [42]. They do however exhibit the characteristic fractal structures that make them strange. Some strange non-chaotic attractors have in fact been observed in the study of variable stars, specifically in some RR Lyrae stars [20].

However, SNAs are often associated with non-autonomous dynamical systems.

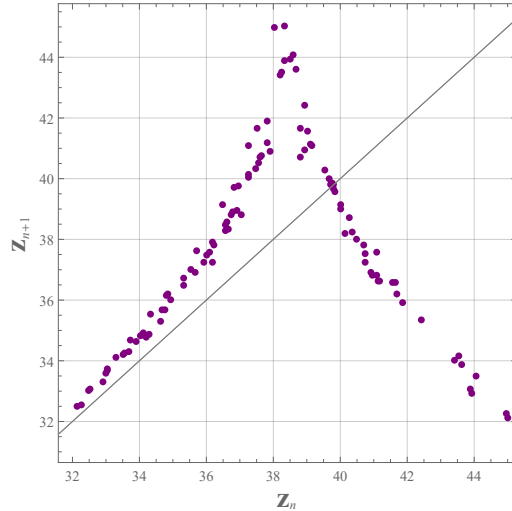


**Figure 3.2:** The Lorenz Map of the Lorenz system for  $\sigma = 10, \rho = 28, \beta = \frac{8}{3}$ . Plotted using the *Mathematica*® code of Binous et al. (2013) [4].

The dynamical systems we will be dealing with in this work are exclusively autonomous systems. Thus, for the rest of this work, we may refer to strange chaotic attractors as simply strange attractors without loss of ambiguity.

### 3.3 Lorenz Maps

Considering the intractability of directly analyzing the structure of strange attractors by looking at the full three-dimensional chaotic phase plot such as in Figure 2.7, Lorenz sought to find a way to cut down on the complexity and find a simpler way to study the features of a strange attractor [21]. He presented what are now called Lorenz Maps, or first return maps, in which the successive maxima of a single state variable are plotted in two-dimensions.

In the case of one of the chaotic solutions of the Lorenz system, the successive maxima,  $z_n$  vs  $z_{n+1}$ , are plotted in Figure 3.2 using the code from Binous et al. (2013) [4]. This forms what is called a tent map, as the plot looks like a tent [40].

Lorenz posited that succeeding points would fall along this curve. While the curve does not represent a well-defined function, as there is some thickness to the curve, it is still a useful way to study the strange attractor [40]. This is because by use of a Lorenz Map we are able to characterize patterns in the successive maxima of state variables that are a lot less complicated than the full phase plots.

Another use of Lorenz Maps is that they present an easy means of telling the

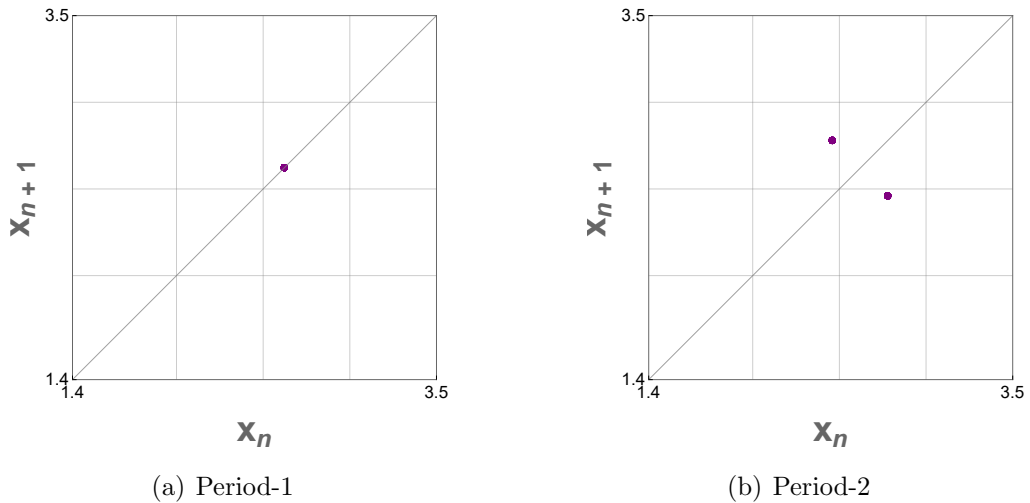


**Figure 3.3:** Lorenz Maps of a state variable  $x$  showing period-1 and period-2 solutions.

periodicity of solutions. Considering that when looking at a time-series of a state variable, we tell the periodicity by counting the number of maxima per cycle, a Lorenz Map is able to present this information in a more intuitive way. We can tell the periodicity of a solution by counting the number of points present on the plot, after of course considering a long enough time interval. In Figure 3.3, we show period-1 and period-2 solutions which are shown by having 1 point and 2 points on their respective Lorenz Maps.

For this work, we adapt the *Mathematica*® code of Binous (2012) for rendering the Lorenz Maps we will make use of in our analysis later [3].

### 3.4 Time-delay embedding for attractor reconstruction

It is pertinent to consider that while models of physical phenomena represented by dynamical systems may have multiple state variables  $\{x_d\}$ , it is often difficult or impossible to get information about all of these state variables in real life experiments or observations of nature. Thus, this opens up the problem of how to properly compare data of perhaps only a single observable state variable to a model with multiple state variables. This is especially difficult for chaotic systems, which are expected to show a sensitive dependence on initial conditions.

In the previous subsection, we presented a means of visualizing some geometric

features of the strange attractors of dynamical system via the use of Lorenz Maps which plot successive maxima. While this is of course a useful tool, we are unable to reconstruct the dynamics of the dynamical system from these maps alone. This is of course because the behavior of the time-series between each maxima are lost in these forms of plots.

This leads us to turn to the method of time-delay embeddings to reconstruct the dynamics of systems with strange attractors using information from only a single state variable. To do this, we make use of what are called delay coordinates [17]. In this coordinate system, we state the time-delay vectors, which replace the vectors  $\mathbf{x}$  of all the state variables in Equation 2.5, as

$$\mathbf{s}_t = (s_t, s_{t+\tau}, s_{t+2\tau}, \dots, s_{t+(d_e-1)\tau}). \quad (3.3)$$

This is equivalent to collecting information about a single state variable  $s$  for  $d_e$  time intervals of length  $\tau$ <sup>1</sup> [40]. Thus, we restate this delay-vector in a more intuitive form as

$$\mathbf{s}_t = (s(t), s(t + \tau), \dots, s(t + (d_e - 1)\tau)). \quad (3.4)$$

Here,  $\tau$  is referred to as the delay time. There is no one size fits all method for finding an appropriate optimal value for the delay time, which we denote  $\tau_{opt}$ . This is because it often depends on what the particular goal of the attractor reconstruction is. In this work, our purpose is to reconstruct the strange attractor of a one-zone model using a single state variable, such as the stellar radius  $r$  or radial velocity  $v$ , for potential comparison in the future with observational data of stellar radii and radial velocities. For this goal then, the optimization of the delay time  $\tau$  can be done by minimizing the average mutual information between components of the delay vector  $\mathbf{s}_t$ . The details of this will be discussed in the next subsection.

On the other hand,  $d_e$  is an integer called the embedding dimension. We note that since  $d_e$  determines the number of intervals we collect information about  $s$ , it also determines the dimension of our new delay coordinate system. Thus, we can consider the embedding dimension  $d_e$  as the number of dimensions our delay vectors need to be to reconstruct the dynamics of the original dynamical system [36]. By extension, this sets the number of dimensions our plots of the time-delay reconstruction will

---

<sup>1</sup>Note that the delay time  $\tau$  we use here is different from the  $\tau$ , representing the dimensionful time, we use in our derivation of the one-zone models in Chapter 4. We will never use these two versions of  $\tau$  in the same context, so there should be no need for confusion to arise.

have. The fact that  $d_e$  is an integer may lead to some confusion, as we previously mentioned that strange attractors are characterized by fractional dimensions. The embedding dimension is a measure describing the dynamics of the system, while the fractional dimensions of a strange attractor such as the box-counting dimension or correlation dimension are specific geometric quantities. We will not be dealing with these particular geometric dimensions in this work.

The validity of phase space reconstruction via time-delay embeddings is ensured by Takens' Theorem [41]. This states that for a deterministic system, by selecting a sufficient delay time  $\tau_{opt}$  and embedding dimension  $d_e$ , we may construct a set of delay coordinates  $\mathbf{s}_t$  that have a smooth invertible map to the coordinate system made up of the original state variables [36]. This effectively means that the delay coordinates contain the same topological information about the dynamics of the system as the original coordinates made up of the state variables do. It also means that information about the strange attractors for chaotic systems, such as Lyapunov exponents, can just as well be calculated using our delay reconstruction as from the original state variables.

For this work, we perform our time-delay embedding reconstruction using the publicly available *Mathematica*® package of Ruskeepää (2014) [36].

### 3.5 Finding an optimal delay time $\tau_{opt}$

There is some arbitrariness in the best choice for the delay time  $\tau_{opt}$ . However, as previously stated, the method of minimizing the average mutual information between delay vector components is best suited for our purposes.

Essentially, when we are trying to reconstruct the dynamics of a set of state variables  $\{x_d\}$  using a delay vector  $\mathbf{s}_t$ , we wish to ensure that each component of  $\mathbf{s}_t$  contains as much unique information as possible. Thus, each component of  $\mathbf{s}_t$  must be sufficiently uncorrelated from its fellow components, in order to maximize their usefulness. If we choose a  $\tau_{opt}$  that is too small, the different components of  $\mathbf{s}_t$  will be so temporally close to one another, that we are unable to maximize the amount of unique information carried by each component. However, we also cannot pick  $\tau_{opt}$  to be too large, as the components may end up being too unrelated to one another, and we will be unable to meaningfully reconstruct the dynamics of the system [36]. Therefore, the process of minimizing the average mutual information for the purposes

of time-delay reconstruction involves solving for the first minima of average mutual information between the components of  $\mathbf{s}_t$ .

In order to understand this, we must first establish how we calculate the mutual information between functions. For random variables  $X$  of  $x$  and  $Y$  of  $y$ , the mutual information, measured in bits, is given by

$$I(X; Y) = \log_2 \left( \frac{P_{X,Y}(x, y)}{P_X(x)P_Y(y)} \right), \quad (3.5)$$

where the functions  $P$  are the probability densities.

If  $X$  and  $Y$  are independent, the joint probability density is just

$$P_{X,Y}(x, y) = P_X(x)P_Y(y). \quad (3.6)$$

Thus, the mutual information is thus zero, as

$$I(X; Y) = \log_2 \left( \frac{P_X(x)P_Y(y)}{P_X(x)P_Y(y)} \right) = 0. \quad (3.7)$$

To calculate the average mutual information between  $X$  and  $Y$  then, we have the formula

$$I_{X,Y} = \sum_x \sum_y P_{X,Y}(x, y) \log_2 \left( \frac{P_{X,Y}(x, y)}{P_X(x)P_Y(y)} \right). \quad (3.8)$$

For the purposes of time-delay reconstruction, we collect data points from the time-series of a single state variable  $s$ . We then separate the information stored in these data points into different bins of specified width, as in a histogram. From this time-series data, we construct delay vector components  $s_t$  and  $s_{t+\tau}$ . For these two components then, we calculate the average mutual information as

$$I(\tau) = \sum_i \sum_j p_{i,j}(\tau) \log_2 \left( \frac{p_{i,j}(\tau)}{p_i p_j} \right), \quad (3.9)$$

where  $p_i$  is the probability that the component is in the  $i$ -th bin of a histogram. This is given by the relative frequency that a data point is found in the  $i$ -th bin [36].

In order to minimize the average mutual information then, the value of  $\tau$  is increased until we get the first minima of Equation 3.9. This value of  $\tau$  is then taken to be our optimal delay time  $\tau_{opt}$ . While  $\tau_{opt}$  can be any positive real number, it is often taken to be an integer for convenience. It is often even taken to be a range of values, instead of a single optimal value. This reflects the fact expressed earlier that the choice of an optimal  $\tau$  is somewhat arbitrary.

### 3.6 Choice of embedding dimension $d_e$

The choice of the value of the embedding dimension  $d_e$  is paramount to the process of time-delay reconstruction as it determines the number of delay coordinates necessary. We can of course consider simply choosing the largest value for  $d_e$  possible, as that would almost certainly ensure that we have enough information stored in the different coordinates. However, we should note that analysis and visualization of a system becomes increasingly difficult as we increase the number of dimensions. For example, if three dimensions is sufficient, using  $d_e = 4$  would definitely also work, but this choice would just complicate things unnecessarily.

The question now arises as to how to determine an appropriate minimal value of  $d_e$ . A well-established method for this is the method of false nearest neighbors [18]. The principle behind this method is ensuring that there is no loss of information about the true distances between points from having too low of an embedding dimension.

This can be better illustrated with an example. We can imagine two points on a three-dimensional helix that are on different rungs of the structure. If we represent this helix in two dimensions, these two points may appear to be very close to one another, since we lose information about the vertical component of their positions. Thus, this pair of points would be false nearest neighbors, as the projection in two dimensions leads us to wrongly classify them as being close together.

The method of false nearest neighbors then consists of increasing the value of the embedding dimension  $d_e$  until there are no false nearest neighbors left. Since at this point, we would have already found our optimal delay time  $\tau_{opt}$ , this is the value of  $\tau$  we use here.

We consider the representation of single point  $x$  in  $d_e$  dimensions as

$$x = (x_t, x_{t+\tau_{opt}}, \dots, x_{t+(d_e-1)\tau_{opt}}), \quad (3.10)$$

and in  $d_e + 1$  dimensions as

$$x = (x_t, x_{t+\tau_{opt}}, \dots, x_{t+(d_e-1)\tau_{opt}}, x_{t+d_e\tau_{opt}}). \quad (3.11)$$

For some points  $x$  and  $y$  which are nearest neighbors in  $d_e$  dimensions, we calculate their Euclidean distance from one another as

$$R_{d_e} = \sqrt{\sum_{i=0}^{d_e-1} (x_{t+i\tau_{opt}} - y_{t+i\tau_{opt}})^2}. \quad (3.12)$$

If we go a dimension higher, in  $d_e + 1$  dimensions the Euclidean distance would then be given by

$$R_{d_e+1} = \sqrt{\sum_{i=0}^{d_e-1} [(x_{t+i\tau_{opt}} - y_{t+i\tau_{opt}})^2] + (x_{t+d_e\tau_{opt}} - y_{t+d_e\tau_{opt}})^2}. \quad (3.13)$$

Thus, if we wish to minimize the number of false nearest neighbors, we consider the distance increase between two nearest neighbors when we move up from  $d_e$  dimensions to  $d_e + 1$  dimensions. If this distance increase is large in comparison to  $R_{d_e}$ , then the two points were false nearest neighbors. We thus need to establish a threshold criteria for determining whether or not we consider this distance increase large enough. This is given by

$$\sqrt{\frac{(x_{t+\tau_{opt}} - y_{t+\tau_{opt}})^2}{R_{d_e}^2}} > T_1, \quad (3.14)$$

where  $T_1$  is some threshold value. In the literature,  $T_1$  is usually taken to be  $T_1 = 15$  [36]. Thus, this is the threshold value we consider here. For some data sets which require high embedding dimensions, a point may be wrongly considered to be a true nearest neighbor. Thus, an additional requirement involving the standard deviation  $\sigma$  is used. This is stated as

$$\frac{|x_{t+\tau_{opt}} - y_{t+\tau_{opt}}|}{\sigma} > T_2, \quad (3.15)$$

where  $T_2$  is another threshold value conventionally taken to be  $T_2 = 2$  [36]. Thus, the lowest value of  $d_e$  wherein by these criteria there are zero false nearest neighbors, is the optimal value for the embedding dimension.

After the appropriate values of  $\tau_{opt}$  and  $d_e$  are found, we then proceed to plotting the reconstructed phase space using our delay coordinates. This can then be compared to the phase plots rendered from the set of original state variables, so that we can qualitatively assess if they show similarities. It is also possible that the optimal values of the delay time  $\tau_{opt}$  and the embedding dimension  $d_e$  show some dependence on the state variable chosen for the reconstruction [9, 31], and thus it may be of interest to find if such dependence applies to our systems.

# Chapter 4

## Stellar pulsation in the one-zone models

All models are wrong,  
but some are useful.

---

*George E.P. Box*

Before we begin to discuss the process of stellar pulsation, it is important to first establish the case wherein a star is in hydrostatic equilibrium. This means that the surface of the star is unmoving, as the pressure pushing outward exactly balances the gravitational force pulling inward.

We recall from the first chapter that Newton's 2nd Law for a star described by a one-zone model is given by

$$m \frac{d^2 R}{d\tau^2} = -\frac{GMm}{R^2} + 4\pi R^2 P. \quad (4.1)$$

To get the acceleration of the spherical shell, we simply divide both sides by the mass of the shell  $m$  to get

$$\frac{d^2 R}{d\tau^2} = -\frac{GM}{R^2} + \frac{4\pi R^2 P}{m}. \quad (4.2)$$

In hydrostatic equilibrium, the acceleration would be zero, so this yields

$$0 = -\frac{GM}{R_\star^2} + \frac{4\pi R_\star^2 P_\star}{m}, \quad (4.3)$$

$$\frac{GM}{R_\star^2} = \frac{4\pi R_\star^2 P_\star}{m}, \quad (4.4)$$

and the condition

$$\frac{4\pi}{m} = \frac{GM}{P_\star R_\star^4}, \quad (4.5)$$

where we use the  $\star$  subscript to denote equilibrium values.

Now that we have established the hydrostatic equilibrium case of a star, we now consider a case wherein some process, such as a random variation in pressure, leads to a small perturbation away from equilibrium. For non-variable stars, such as many main sequence stars like the Sun, these small perturbations are often not spherically-symmetric and die down relatively quickly<sup>1</sup>. Thus, they roughly maintain hydrostatic equilibrium over long timescales.

However, for stellar pulsators this is not the case. These small variations from equilibrium often end up growing into sustained oscillations [24]. In the first two sections of this chapter, we discuss two of the physical mechanisms within AGB and post-AGB stars that contribute to these pulsations in long-period variables: the  $\kappa$ -mechanism and non-adiabaticity.

## 4.1 The $\kappa$ -mechanism

The opacity of layers in a star is governed by Kramers' Law, which relates the density  $\rho$  and temperature  $T$  to the opacity  $\kappa$  as

$$\kappa = \kappa_0 \rho^n T^{-s}, \quad (4.6)$$

where  $\kappa_0$  is some proportionality constant, and  $n$  and  $s$  are the opacity exponents. Stellingwerf (1972) made the choice of opacity exponents  $n = 1$  and  $s = 3$ , for use in their one-zone model [38]. For these constant exponents then, we get

$$\kappa = \kappa_0 \rho T^{-3}. \quad (4.7)$$

In proposing a means by which opacity variations may drive stellar pulsation, Sir Arthur Eddington proposed a “valve mechanism” [10]. In this process, during phases of contraction, some layers of the star become more opaque due to the increase in density. This then traps energy beneath the layer, which in turn increases the pressure. This pressure pushing outwards then leads to an expansion [8]. As the star continues to expand and the pressure decreases, the gravitational force in Equation 4.1 once again dominates, leading to a contraction once more. Thus, we would have a series of alternating expansions and contractions of the stellar surface.

However, it should be considered that we would also expect a contraction trapping energy to increase the temperature. This then poses a problem as the form of Equation

---

<sup>1</sup>Solar-like stars also exhibit oscillations, but these are often more localized and are driven by different processes from those in LPVs.

4.7 shows a higher sensitivity on the temperature  $T$  than on the density  $\rho$ . Since the exponent of  $T$  is negative, this would hypothetically bring down the overall opacity of the gases during contraction phases instead of increasing it [8]. Thus, this would not allow for the driving of the pulsation.

The means for subverting this dominance of the temperature rise in contraction was later found to be attributable to the presence of partial ionization zones in Cepheids, long-period variables, and some other stellar pulsators. In these zones, specifically HeII partial ionization zones, the energy dammed up during expansion ends up contributing to the ionization of the gases. This leads to there being less energy left to contribute to a rise in temperature. Thus, the increase in the density dominates during these contraction phases, and the opacity does indeed rise. Furthermore, when the build up of pressure later leads to expansion, the energy stored in the ionized gases gets released. This then further excites the said expansion [11].

This process by which changes in the opacity drive oscillations is known as the  $\kappa$ -mechanism. It has also been considered that the choice of constant opacity exponents  $n$  and  $s$  in Equation 4.6 may be too crude an approximation for LPVs. We will later explore a case wherein the opacity exponents are dynamical quantities and also temporally evolve.

## 4.2 Non-adiabaticity

Non-adiabaticity is a measure of the ability of fluid components within the star to transfer heat to one another. A useful way this is quantified is by comparing timescale of fluid movement within the star to the timescale of heat transfer. This makes sense as if the time it takes for heat to transfer between components is comparable in magnitude to the time it takes for fluid components to move up in the star, we would expect non-adiabatic effects to be more prominent.

We can imagine there to be some average timescale for fluid components to move up in the star, which we refer to as the dynamical timescale  $\tau_{dyn}$ . The speed of this movement is governed by the speed of sound  $c_s$  within the star. We can therefore write the dynamical timescale as

$$\tau_{dyn} = \frac{\Delta R}{c_s}, \quad (4.8)$$

where  $\Delta R$  denotes the radial extension of the region of the star being considered.

The thermal timescale  $\tau_{thm}$  on the other hand measures the average amount of time it takes for fluid components to transfer heat between one another. This is given by

$$\tau_{thm} = 4\pi R^2 \left( \frac{\rho c_V T}{L_R} \right) \Delta R, \quad (4.9)$$

where  $c_V$  is the specific heat capacity at constant volume, and  $L_R$  is the luminosity at a given radius  $R$ .

This now allows us to define our dimensionless measure of non-adiabaticity as the ratio between the dynamical and thermal timescales

$$\xi = \frac{\tau_{dyn}}{\tau_{thm}}. \quad (4.10)$$

This yields for the whole star in the one-zone model

$$\xi = \frac{L_\star}{\omega_\star c_V m T_\star}, \quad (4.11)$$

where we define the characteristic frequency of the star at equilibrium as

$$\omega_\star \equiv \sqrt{\frac{GM}{R_\star^3}}. \quad (4.12)$$

We can think of the study of stellar pulsation as the attempt to understand the relationship between the energy processes within the star and the mechanical movement of the stellar surface. Thus, we can consider a star to be a coupled thermo-mechanical oscillator, where the non-adiabaticity parameter  $\xi$  is our coupling constant [25].

For long-period variable stars, the strength of non-adiabaticity is relatively low but non-zero [26, 37, 38]. This basically means that for such stars the response time for mechanical processes is much faster than its thermodynamic response time. In this study then, we consider values for the non-adiabaticity between

$$0 < \xi \leq 0.2. \quad (4.13)$$

The upper boundary of  $\xi = 0.2$  is chosen in order to allow for comparison to the values of  $\xi$  examined by Saitou et al. (1989) and Munteanu (2003) [26, 37]. It may be possible for some long-period variable stars to be described by values of  $\xi$  slightly higher than this, but we restrict our probes to the range of values for  $\xi$  already established in the literature.

In contrast to this, values for the strength of the non-adiabaticity of about  $\xi \approx 1$  correspond to other stars within the instability strip of the Hertzsprung-Russell

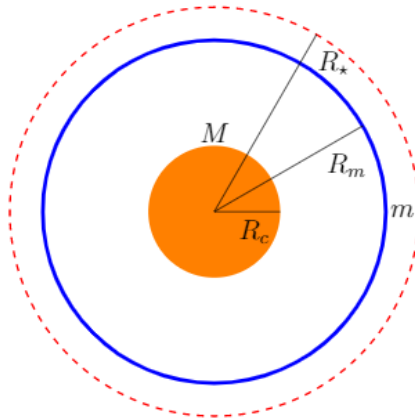


**Figure 4.1:** Diagram of a star using the one-zone model. (Not to scale.)

diagram, such as classical Cepheids. For such stars, the mechanical and thermal timescales are expected to be comparable, so this makes sense [38]. However, such stars are not the focus of this work.

### 4.3 Motivation and history of one-zone models

A fundamental assumption behind one-zone models of stellar pulsation is that since these stars being modeled are rather large, it is possible to approximate the nuclear burning regions and the upper regions as two discrete masses. This is because the differences in density between the two regions are so pronounced that we can consider them as essentially decoupled from one another.

In Figure 4.1, we present the diagram of a star using the one-zone model formalism of Munteanu (2003) [24], which is what we will use for this work. Here, we have a static stellar “core” with constant radius  $R_c$ , which is made up of stellar mass  $M$ . This is surrounded by our spherical shell, of radial extension  $R_m$  and mass  $m$ , representing the surface or “mantle” of the star. Thus, we are able to treat the star in the one-zone model as two discrete masses  $M$  and  $m$ .

One-zone models were first put forward by Baker (1966), in order to understand some of the processes which may lead to the decrease or increase in the amplitudes of initial oscillations in Cepheid type variables. This was presented in the form of four linear differential equations describing a spherically-symmetric star, whose mode of energy transport was radiation pressure [2]. Thus, this only considered

radial oscillations, and did not show take into account any angular dependence of oscillations.

Baker's model for Cepheid variability was expanded upon by Rudd and Rosenberg (1970), wherein they now considered nonlinear differential equations. One feature of their equations of motion was that they had two different equations specifying the change of the radial velocity. One described contraction phases, while another described expansion phases [35].

Drawing from Rudd and Rosenberg (1970), Stellingwerf (1972) adapted the equations of motion such that there was only one equation of motion for the radial velocity, instead of the two distinct ones for contracting and expansionary phases. The opacity in this model was considered to have the constant opacity exponents  $n = 1$  and  $s = 3$ . This work also considered a parametric study of variation in the strength of non-adiabaticity  $\xi$ , which later allowed for the extension of the one-zone model to represent other variable stars aside from Cepheids [38].

Saitou et al. (1989) modified the Stellingwerf (1972) model for the case of non-constant opacity coefficients. This allowed for one-zone models to be used to describe long-period variables, instead of just Cepheids. Using a dynamical systems approach, they explored a period-doubling route to chaos from variation in a parameter  $a$ <sup>2</sup> controlling the strength of the  $\kappa$ -mechanism. Using radial velocity Lorenz Maps, they were able to show some similarity in the patterns of these maps to that of observational luminosity Lorenz Maps of some RV Tauri and Semiregular variables [37]. Another route to chaos was found in this model by Munteanu et al. (2003), but this time it was via variation in the non-adiabaticity parameter  $\xi$  [26]. The phenomena of period-doubling from variation in the parameters  $a$  and  $\xi$  controlling two very different physical mechanisms in the model, the  $\kappa$ -mechanism and the non-adiabaticity respectively, is of much interest. This is because it may entail that long-period variables have multiple routes to achieve the irregular and even chaotic oscillations associated with them.

The one-zone models discussed so far have only considered radial oscillations via radiation pressure as the means of energy transport. The models we will be probing in this work will likewise be limited to spherically-symmetric pulsation and radiative energy transport. For one-zone models involving non-radial oscillations, we advise

---

<sup>2</sup>This parameter  $a$  is defined later in our derivation, specifically in Equation 4.59.

the reader to refer to Zahn (1968) [44]. Analysis involving time-dependent convection as an additional mode of energy transport can be found in Moore and Spiegel (1966), Stellingwerf (1986), and Icke et al. (1992)[14, 23, 39].

## 4.4 Derivation of the one-zone models

We may now begin deriving the equations of motion for the one-zone models we will be considering. We seek three final equations of motion in the form of ordinary differential equations for the radius, radial velocity, and pressure.

We focus our work on two one-zone models in particular. The first model is based off Stellingwerf (1972), wherein the opacity exponents in Kramers' Law are the constants shown in Equation 4.7 [38]. The second case we consider is one in which the opacity coefficients are dynamical quantities that are functions of the radius and pressure, as forwarded by Saitou et al. (1989) and Munteanu et al. (2003) [26, 37]. For convenience, we will just refer to these as the Stellingwerf and Munteanu models respectively. While there are other formulations of one-zone models present in the literature, we specifically selected these two for analysis due to the similarity in the forms of the differential equations making up their respective dynamical systems. This allows for a much more straightforward comparison of the effects of having constant opacity coefficients to a case wherein the opacity exponents dynamically evolve. These models have furthermore already had some successes in replicating some observational behaviors of variable stars, and thus prove ripe for further study [37, 38].

In order to ease our comparison of the dynamics between these two models, we have adopted a consistent formalism for the variables and parameters to be used. The differences in the opacity exponents between the two models will only become relevant in the final equations of motion. This means that the derivation we present here is consistent with both models to be considered.

We recall that the spherical shell is what exhibits oscillations about the equilibrium radius  $R_*$ , so we restate Euler's Equation in Equation 4.1 as

$$m \frac{d^2 R_m}{d\tau^2} = -\frac{GMm}{R_m^2} + 4\pi R_m^2 P_m. \quad (4.14)$$

We consider a stellar energy equation representing the processes outside the core. Since we assume that all the nuclear processes occur within the sphere defined by

$R_c$ , we do not include a nuclear energy term. Instead, we consider that the energy from the nuclear production within the core is already being transmitted via radiation pressure and fluid movement due to density changes. This then gives us the energy equation

$$c_V \frac{\partial T}{\partial \tau} = \left( \frac{P}{\rho^2} \right) \frac{\partial \rho}{\partial \tau} - \frac{\partial L}{\partial M_{R_m}}. \quad (4.15)$$

Here,  $c_V$  is our specific heat capacity at constant volume. The partial differential  $\partial M_{R_m}$  represents the mass differential across the radius  $R_m$  [37]. For our case, this is just the shell mass  $m$ , so we rewrite this as

$$c_V \frac{\partial T}{\partial \tau} = \left( \frac{P}{\rho^2} \right) \frac{\partial \rho}{\partial \tau} - \frac{\partial L}{\partial m}. \quad (4.16)$$

The Lagrangian luminosity derivative was approximated in Baker (1966) as simply

$$\frac{\partial L}{\partial m} = \left( \frac{L - L_c}{2} \right) \frac{1}{m}, \quad (4.17)$$

where  $L$  is the luminosity coming out of the shell, and  $L_c$  is the luminosity coming out of the core [2]. However, Stellingwerf (1972) found that this factor of  $\frac{1}{2}$  has little effect, so we follow their lead and drop it [38]. We also consider that the luminosity coming out of the core  $L_c$  is equivalent to the equilibrium luminosity  $L_*$ . Therefore, our energy equation becomes

$$c_V \frac{\partial T}{\partial \tau} = \left( \frac{P}{\rho^2} \right) \frac{\partial \rho}{\partial \tau} - \left( \frac{L - L_*}{m} \right). \quad (4.18)$$

Considering a diffusion approximation, the luminosity is given by

$$L = - \frac{16\pi R^2 \sigma}{3\kappa\rho} \frac{\partial T^4}{\partial R}, \quad (4.19)$$

where  $\sigma$  is the Stefan-Boltzmann constant. We further approximate the fourth derivative of  $T$  with respect to  $R$  as simply

$$\frac{\partial T^4}{\partial R} = - \frac{T^4}{R}. \quad (4.20)$$

Thus, our luminosity equation simplifies to

$$L = \frac{16\pi R \sigma T^4}{3\kappa\rho}. \quad (4.21)$$

It is helpful to express our final equations of motion in a dimensionless form, so we define the dimensionless variables for the radius and pressure as

$$r \equiv \frac{R_m}{R_*}, \quad (4.22)$$

and

$$p \equiv \frac{P_m}{P_\star}. \quad (4.23)$$

For convenience, we state the derivative of  $r$  with respect to  $\tau$  as

$$y \equiv \frac{dr}{d\tau}. \quad (4.24)$$

We can then write the density as

$$\rho = \rho_\star r^{-3}. \quad (4.25)$$

We further assume that the gases in the star follow the Ideal Gas Law, so we have the proportionality

$$PV \propto T, \quad (4.26)$$

which allows us to state the temperature as

$$T = T_\star p r^3. \quad (4.27)$$

Differentiating  $T$  with respect to  $\tau$  yields

$$\frac{\partial T}{\partial \tau} = T_\star \left( 3r^2 y p + r^3 \frac{dp}{d\tau} \right). \quad (4.28)$$

We rearrange this to get the derivative of the dimensionless pressure  $p$  with respect to  $\tau$  as

$$\frac{dp}{d\tau} = \frac{r^{-3}}{T_\star} \frac{\partial T}{\partial \tau} - 3r^{-1} y p. \quad (4.29)$$

We now have to solve for  $\frac{\partial T}{\partial \tau}$  from our energy equation. We first deal with the term including the derivative of  $\rho$ . Using Equation 4.25, we get

$$\frac{\partial \rho}{\partial \tau} = -3\rho_\star r^{-4} y, \quad (4.30)$$

$$\left( \frac{P}{\rho^2} \right) \frac{\partial \rho}{\partial \tau} = -3 \frac{P_\star}{\rho_\star} r^2 y p. \quad (4.31)$$

We now proceed to the luminosity term. As discussed previously, our opacity  $\kappa$  is taken to follow Kramers' Law of the form of Equation 4.6. When we plug this into Equation 4.21, and use our dimensionless radius and pressure variables, we get

$$L = \frac{16\pi\sigma}{3} \frac{R_\star T_\star^{s+4}}{\kappa_0 \rho_\star^{n+1}} r^{3n+3s+16} p^{s+4}, \quad (4.32)$$

for the luminosity out of the shell, and

$$L_\star = \frac{16\pi\sigma}{3} \frac{R_\star T_\star^{s+4}}{\kappa_0 \rho_\star^{n+1}}, \quad (4.33)$$

for the equilibrium luminosity. Subtracting these two gives us

$$L - L_\star = \frac{16\pi\sigma}{3} \frac{R_\star T_\star^{s+4}}{\kappa_0 \rho_\star^{n+1}} r^{3n+3s+16} p^{s+4} - \frac{16\pi\sigma}{3} \frac{R_\star T_\star^{s+4}}{\kappa_0 \rho_\star^{n+1}}. \quad (4.34)$$

For convenience, we introduce the terms

$$\beta \equiv 3n + 3s + 16, \quad (4.35)$$

and

$$\delta \equiv s + 4. \quad (4.36)$$

This allows us to factor the luminosity difference nicely as

$$L - L_\star = L_\star [r^\beta p^\delta - 1]. \quad (4.37)$$

We can now plug in Equations 4.31 and 4.37 back into our energy equation, which yields

$$c_V \frac{\partial T}{\partial \tau} = -3 \frac{P_\star}{\rho_\star} r^2 y p - \frac{L_\star}{m} [r^\beta p^\delta - 1]. \quad (4.38)$$

Dividing both sides by  $c_V T_\star r^3$  gives

$$r^{-3} \frac{1}{T_\star} \frac{\partial T}{\partial \tau} = -3 \frac{P_\star}{c_V \rho_\star T_\star} r^{-1} y - \frac{L_\star}{c_V m T_\star} r^{-3} [r^\beta p^\delta - 1]. \quad (4.39)$$

The adiabatic coefficient is defined as

$$\Gamma_1 = 1 + \frac{P_\star}{c_V \rho_\star T_\star}. \quad (4.40)$$

Plugging this in, and substituting Equation 4.39 into Equation 4.29, yields

$$\frac{dp}{d\tau} = -3\Gamma_1 r^{-1} y p - \frac{L_\star}{c_V m T_\star} r^{-3} [r^\beta p^\delta - 1]. \quad (4.41)$$

Since we seek to fully nondimensionalize our equations of motion, we need to make the time dimensionless as well. To accomplish this, we first consider that the characteristic frequency of the stellar mantle as being given by

$$\omega_m \equiv \sqrt{\frac{GM}{R_m^3}}. \quad (4.42)$$

However, since we assume that the stellar surface oscillates near the equilibrium configuration, we can approximate it as constant

$$\omega_m \approx \omega_*. \quad (4.43)$$

We now seek to get an equation for the derivative of  $y$  with respect to  $\tau$ . We note that

$$dy = d^2r = R_* d^2R_m. \quad (4.44)$$

Thus, from the Euler Equation in Equation 4.14 we get

$$\frac{dy}{d\tau} = -\frac{GM}{R_*^3} r^{-2} + \frac{4\pi}{m} P_m \frac{R_m^2}{R_*}, \quad (4.45)$$

Using the equilibrium condition from Equation 4.5, we can restate this as

$$\frac{dy}{d\tau} = -\frac{GM}{R_*^3} r^{-2} + \frac{GM}{R_*^3} p r^2, \quad (4.46)$$

$$\frac{dy}{d\tau} = \omega_m^2 [p r^2 - r^{-2}]. \quad (4.47)$$

To make this fully dimensionless then, we define the dimensionless time as

$$t \equiv \omega_m \tau. \quad (4.48)$$

Evaluating the differentials yields

$$dt = \omega_m d\tau, \quad (4.49)$$

and

$$dt^2 = \omega_m^2 d\tau^2. \quad (4.50)$$

We further define the dimensionless radial velocity as

$$\frac{dr}{dt} = v. \quad (4.51)$$

Thus, we have

$$\frac{dv}{dt} = \frac{1}{\omega_m^2} \frac{dy}{d\tau}, \quad (4.52)$$

and

$$\frac{dp}{dt} = \frac{1}{\omega_m} \frac{dp}{d\tau}. \quad (4.53)$$

Using dot notation to denote a derivative with respect to  $t$ , we can then finally write our three equations of motion as

$$\begin{aligned}\dot{r} &= v \\ \dot{v} &= pr^2 - r^{-2} \\ \dot{p} &= -3\Gamma_1 r^{-1}vp - \xi r^{-3} (r^\beta p^\delta - 1),\end{aligned}\tag{4.54}$$

where  $\xi$  is the dimensionless parameter controlling the amount of non-adiabaticity defined earlier, and the adiabatic coefficient  $\Gamma_1$  is taken to be  $\frac{5}{3}$  for an ideal monoatomic gas. These equations of motion make up the third order dynamical system we will be analyzing in this work.

The difference between the Stellingwerf and Munteanu models is ultimately found in the specification of the opacity exponents  $n$  and  $s$  making up  $\beta$  and  $\delta$ . We now set out to explore this difference between the two models in the succeeding sections.

## 4.5 The Stellingwerf Model

The model of Stellingwerf (1972) was made primarily as a nonlinear model of Cepheid variation. However, some of the low values of the non-adiabaticity parameter  $\xi$  explored prove apt for comparison to long-period variables.

As previously stated, Stellingwerf made the choice of  $n = 1$  and  $s = 3$  as the constant opacity exponents. This means we have

$$\beta = 28,\tag{4.55}$$

and

$$\delta = 7.\tag{4.56}$$

Thus, for this case, our equations of motion in Equation 4.54 become

$$\begin{aligned}\dot{r} &= v \\ \dot{v} &= pr^2 - r^{-2} \\ \dot{p} &= -3\Gamma_1 r^{-1}vp - \xi r^{-3} (r^{28} p^7 - 1).\end{aligned}\tag{4.57}$$

This means that since we have already specified  $\Gamma_1 = \frac{5}{3}$ , the only parameter that can be varied here is the strength of non-adiabaticity  $\xi$ .

In the original Stellingwerf (1972) paper, the final equations of motion included a few more other parameters. Specifically, it included parameters that defined the

thickness of the shell [38]. However, we are only particularly interested in comparing the effects of having the stated constant opacity exponents to the dynamically evolving opacity exponents in the Munteanu model. The Munteanu model makes no considerations for the specific thickness of the shell, and so we have re-expressed Stellingwerf’s final equations of motion to be consistent with this setup.

## 4.6 The Munteanu Model

The autonomous Munteanu et al. (2003) model is exactly the same as the Saitou et al. (1989) model, aside from a slight difference in convention as to how the state variables are defined. Saitou et al. (1989) stated the differential equations specifically in terms of the growth of the perturbations from equilibrium values of the variables. For example, the dimensionless radial extension was defined by them as

$$r = 1 + x, \tag{4.58}$$

where  $x$  is the perturbation of the radius from the conventional equilibrium. And thus, the differential equation describing variations of the radius was written using  $\frac{dx}{dt}$ . However, since we find the convention of Munteanu et al. (2003), which refers to changes in the variables overall instead of just the perturbations, to be more intuitive, we refer to the model in this work as the Munteanu model [26, 37].

The work of Saitou et al. introduced the time-varying opacity exponents as

$$\beta = a (r^3 p - 1.2) + 21.6, \tag{4.59}$$

and

$$\delta = 3.6 r^3 p (r^3 p - 0.2). \tag{4.60}$$

This gives the final equations of motion for the Munteanu model as

$$\begin{aligned} \dot{r} &= v \\ \dot{v} &= p r^2 - r^{-2} \\ \dot{p} &= -3\Gamma_1 r^{-1} v p - \xi r^{-3} \left( r^{a(r^3 p - 1.2) + 21.6} p^{3.6 r^3 p (r^3 p - 0.2)} - 1 \right). \end{aligned} \tag{4.61}$$

Thus, unlike the Stellingwerf model, we have two parameters that may be tuned, instead of just one. The additional control parameter present in this model is  $a$ , which controls the strength of the  $\kappa$ -mechanism. For long-period variable stars, values for  $a$  are considered to be given by

$$0 < a < 36. \tag{4.62}$$

Values of  $a$  greater than 36 have been found to be stable against pulsations, and thus cannot describe long-period variables [37]. Thus, we do not deal with such values here.

The form of  $\beta$  and  $\delta$  in this model are not immediately evident. We can recall that the  $\kappa$ -mechanism depends upon processes within the partial ionization zones. Since one-zone models do not include the details of these zones, it is rather difficult to establish an appropriate form for these exponents. Thus, Saitou et al.(1989) performed a best fit of the results of this one-zone model with an existing multi-layered hydrodynamic code they had, which included the details of the said ionization zones [24, 37]. This is what led to this specific form. We can be reassured of the validity of the form of these exponents, as the results from their one-zone model were able to replicate some features of the Lorenz Maps of RV Tauri variables and Semiregular variables.

Now that we have discussed some of the processes of stellar pulsation, along with having established the two one-zone models that we will be working with, we can now proceed to a dynamical systems analysis of these two models in the next chapter.

# Chapter 5

## Dynamical behavior of the one-zone models

The fault, dear Brutus, is not in our stars,  
But in ourselves, that we are underlings.

---

*William Shakespeare*  
*Julius Caesar*

We now proceed to applying the dynamical systems approach to the Stellingwerf and Munteanu models in Equations 4.57 and 4.61 respectively. In order to better characterize these systems, we identify the equilibrium solutions of these two models. This then lets us observe the behavior of the state variables in phase space after small perturbations away from such equilibrium states.

The characterization of such behavior then allows us to gain some insight into the possible long-term behavior of pulsations in stars characterized by these two one-zone models. Additionally, this analysis lets us identify some limitations of the model that may lead to behavior that would be considered unphysical in real stars.

### 5.1 The conventional fixed point

We can recall the state of hydrostatic equilibrium outlined in Equation 4.3. From this, we can find that in dimensionless form the point

$$(r^*, v^*, p^*) = (1, 0, 1), \tag{5.1}$$

is a solution that satisfies this equation. It is also easy to verify that this solution is valid for both the Stellingwerf and Munteanu models, as it is a fixed point of the dynamical system in Equation 4.54 in general.

Since this fixed point defines the regular state we expect a star to be in, the small initial perturbations we apply to the systems occur around this fixed point. Our phase space analysis of the dynamical systems will thus have initial conditions beginning very close to, but not at, this fixed point.

In order to highlight the fact that this fixed point has special physical significance, we will from now on denote it as

$$\mathcal{H} \equiv (1, 0, 1). \quad (5.2)$$

## 5.2 Equilibrium solutions of the Stellingwerf model

In order to understand the dynamical behavior of the Stellingwerf model, we first seek to identify if it has other equilibrium solutions aside from  $\mathcal{H}$ . In order to accomplish this, we set the three differential equations in Equation 4.57 to zero as

$$\begin{aligned} 0 &= v \\ 0 &= pr^2 - r^{-2} \\ 0 &= -3\Gamma_1 r^{-1} vp - \xi r^{-3} (r^{28} p^7 - 1). \end{aligned} \quad (5.3)$$

We find that this is solved by  $\{v = 0 \wedge p = r^{-4}\}$ . This in fact defines a curve in phase space, which we state parametrically and define as

$$\mathcal{E} \equiv (r, 0, r^{-4}). \quad (5.4)$$

We note that this solution diverges when  $r = 0$ . Since we don't expect the star to ever collapse to a point, we can safely confine our curve to  $r > 0$ .

It can be seen that the conventional fixed point  $\mathcal{H}$  in fact lies along this curve, and thus it is an element of it as

$$\mathcal{H} \in \mathcal{E}. \quad (5.5)$$

This means that aside from the conventional hydrostatic equilibrium state, a star described by the Stellingwerf model in fact has an infinite number of equilibrium states defined by the one-dimensional curve  $\mathcal{E}$ . It can be noted that on this curve, larger stars would have a lower corresponding pressure, which of course makes physical sense.

In Figure 5.1, we show a section of the equilibrium curve  $\mathcal{E}$  in the  $(r, v, p)$  phase space. We also show the conventional fixed point  $\mathcal{H}$  as an element of this curve.

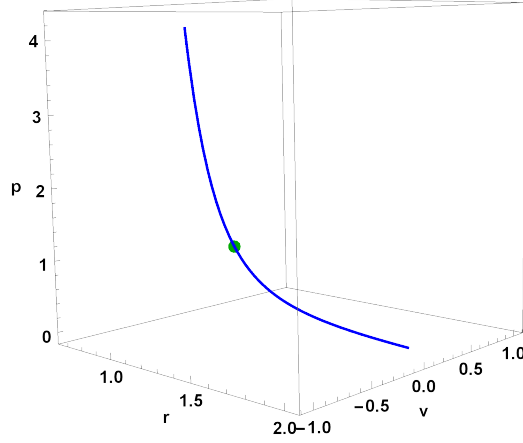


**Figure 5.1:** A section of the equilibrium curve  $\mathcal{E}$  in phase space. The conventional fixed point  $\mathcal{H}$  is shown in green.

We note that since  $\mathcal{E}$  is one-dimensional, the traditional linear fixed point stability analysis and classification we discussed in Chapter 2 does not hold. This is because for every fixed point on the curve, we have two fixed points adjacent on either side of it. We thus must resort to other means to probe the behavior of the dynamical system near the equilibrium curve.

**$r = \text{constant}$  surfaces**

One way we accomplish this is by taking  $r = \text{constant}$  slices of the phase space. This allows us to plot the vector field defined by  $(\dot{\mathbf{v}}, \dot{\mathbf{p}})$  on these two-dimensional slices.

Since the process of taking a slice reduces the phase space to two-dimensions, we only have to consider one fixed point of  $\mathcal{E}$  per surface. We can thus perform a traditional two-dimensional linear stability analysis and fixed point characterization on the reduced phase space of each slice.

We thus define the two-dimensional Jacobian on the  $r = \text{constant}$  slices as

$$\mathbf{J}_r = \left( \begin{array}{cc} \frac{\partial \dot{v}}{\partial v} & \frac{\partial \dot{v}}{\partial p} \\ \frac{\partial \dot{p}}{\partial v} & \frac{\partial \dot{p}}{\partial p} \end{array} \right)_{\mathcal{E}, r=\text{constant}} . \quad (5.6)$$

This evaluates to

$$\mathbf{J}_r = \left( \begin{array}{cc} 0 & r^2 \\ -5r^{-5} & -7\xi r \end{array} \right) . \quad (5.7)$$

From this, we get the trace as

$$Tr(\mathbf{J}_r) = -7\xi r, \quad (5.8)$$

and the determinant as

$$\text{Det}(\mathbf{J}_r) = 5r^{-3}. \quad (5.9)$$

We note that since both  $r$  and  $\xi$  are strictly positive, we find that the trace is strictly negative

$$\text{Tr}(\mathbf{J}_r) < 0. \quad (5.10)$$

This means that the fixed points of  $\mathcal{E}$  on each slice are linearly stable.

We next wish to find which sections of  $\mathcal{E}$  correspond to fixed points which are spirals or nodes on these slices. To accomplish this, we evaluate the sign of

$$\text{Tr}(\mathbf{J}_r)^2 - 4\text{Det}(\mathbf{J}_r) = 49\xi^2 r^2 - 20r^{-3}. \quad (5.11)$$

We see that the sign of Equation 5.11 depends upon the values of  $r$  and  $\xi$ . We can thus solve for the value of  $r$  where this equation changes sign, for a given value of  $\xi$ . We then find that the equation changes sign when

$$r_{crit} = \left(\frac{20}{49}\right)^{\frac{1}{5}} \xi^{-\frac{2}{5}}. \quad (5.12)$$

This means that on  $r = \text{constant}$  slices below this value, the fixed points on  $\mathcal{E}$  are stable spirals. When at or above this value, they are stable nodes. Thus, since all the  $r = \text{constant}$  slices have the points of  $\mathcal{E}$  as linearly stable, we can consider  $\mathcal{E}$  as generally linearly stable on such surfaces.

It is important to remember that these specific classifications only work on each of the two-dimensional slices, and do not classify the points of  $\mathcal{E}$  in the whole three-dimensional phase space.

To aid in this analysis, we present vector plots of  $(\dot{\mathbf{v}}, \dot{\mathbf{p}})$  on some  $r = \text{constant}$  surfaces. This helps us confirm the validity of our linear stability analysis classifications.

In Figure 5.2, we plot the vector field on the surface  $r = 1$  for  $\xi = 0.08$ . This surface includes the conventional fixed point  $\mathcal{H}$ . As we can see, the vector field does appear to be spiralling towards  $\mathcal{H}$  in a clockwise fashion. This is consistent with the fact that for  $\xi = 0.08$ ,  $1 < r_{crit}$ , so  $\mathcal{H}$  is indeed a stable spiral on this surface.

We show the borderline case, where we have the first stable node for  $\xi = 0.08$  on the surface  $r_{crit} \approx 2.29578$  in Figure 5.3. We see that this seems like a borderline case between a spiral and a node. This is evident as we see some trajectories appear to somewhat spiral towards the fixed point. However, there also seems to also be

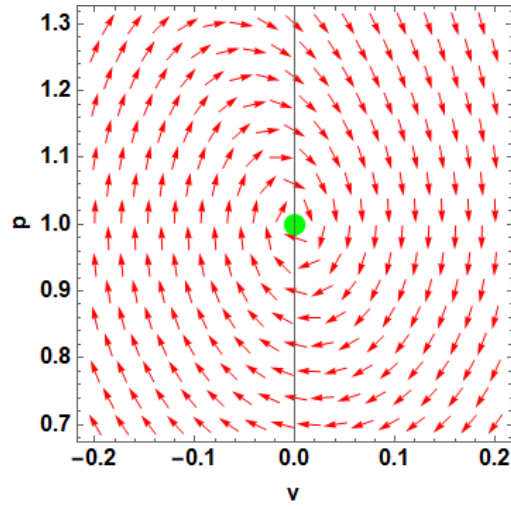


**Figure 5.2:** Vector field  $(\dot{\mathbf{v}}, \dot{\mathbf{p}})$  on the surface  $r = 1$ , for  $\xi = 0.08$ . The stable spiral  $\mathcal{H}$  is shown in green.

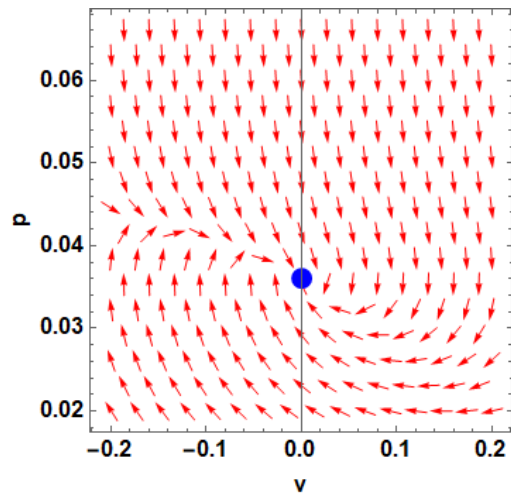


**Figure 5.3:** Vector field  $(\dot{\mathbf{v}}, \dot{\mathbf{p}})$  on the surface  $r \approx 2.29578$ , for  $\xi = 0.08$ . The borderline stable node fixed point of  $\mathcal{E}$  on this surface is shown in blue.

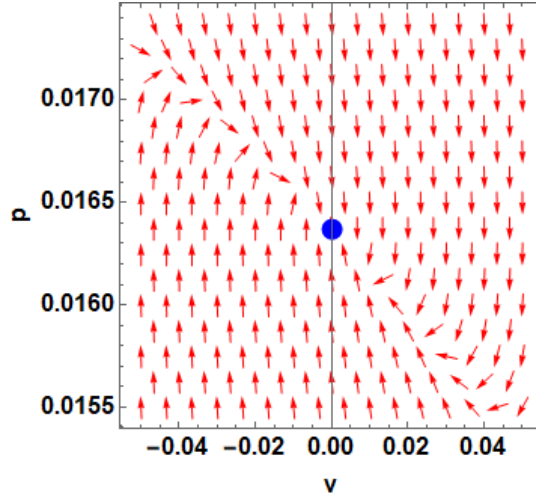


**Figure 5.4:** Vector field  $(\dot{\mathbf{v}}, \dot{\mathbf{p}})$  on the surface  $r \approx 2.34578$ , for  $\xi = 0.08$ . The stable node fixed point of  $\mathcal{E}$  on this surface is shown in blue.

the development of a preferred diagonal eigendirection pointing towards the fixed point. Thus, while we do classify this as a stable node, the fact that it is a borderline case explains why it seems to also show some spiral-like behavior. As Equation 5.11 gets more and more positive, we expect the node-like behavior to become more pronounced.

A case of a stable node, wherein Equation 5.11, is positive, on the surface  $r \approx 2.34578$  for  $\xi = 0.08$  can be seen in Figure 5.4. We can see that the spiral behavior is no longer evident here, in contrast to what we saw for the previous case. We are now more clearly able to see the diagonal eigendirection pointing towards the stable node.

#### $\mathbf{p} = \text{constant surfaces}$

We now repeat the same analysis for  $p = \text{constant}$  slices. This would now allow us to plot the vector field defined by  $(\dot{\mathbf{r}}, \dot{\mathbf{v}})$  on these slices.

We define the two-dimensional Jacobian for these  $p = \text{constant}$  slices as

$$\mathbf{J}_{\mathbf{p}} = \begin{pmatrix} \frac{\partial \dot{r}}{\partial r} & \frac{\partial \dot{r}}{\partial v} \\ \frac{\partial \dot{v}}{\partial r} & \frac{\partial \dot{v}}{\partial v} \end{pmatrix}_{\mathcal{E}, p=\text{constant}}. \quad (5.13)$$

Evaluating this gives us

$$\mathbf{J}_{\mathbf{p}} = \begin{pmatrix} 0 & 1 \\ 4p^{\frac{3}{4}} & 0 \end{pmatrix}. \quad (5.14)$$

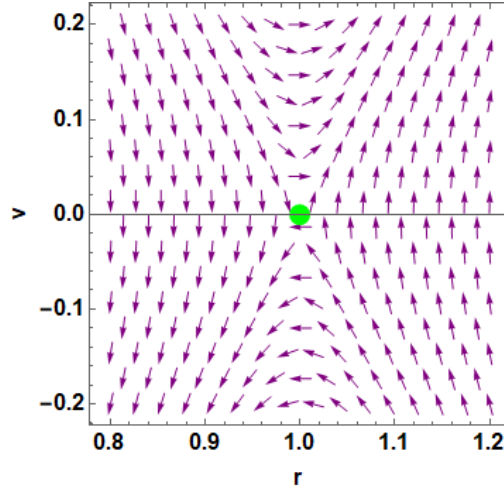


**Figure 5.5:** Vector field  $(\dot{\mathbf{r}}, \dot{\mathbf{v}})$  on the surface  $p = 1$ , for  $\xi = 0.08$ . The saddle point  $\mathcal{H}$  is shown in green.

The determinant is then

$$\text{Det}(\mathbf{J}_{\mathbf{p}}) = -4p^{-\frac{3}{4}}. \quad (5.15)$$

Since  $p$  is also strictly positive  $p > 0$ , the determinant is strictly negative

$$\text{Det}(\mathbf{J}_{\mathbf{p}}) < 0. \quad (5.16)$$

This means that on these  $p = \text{constant}$  slices, the points of  $\mathcal{E}$  are saddle points. This means that they may be attracting in some directions, but repelling in others.

We show the surface  $p = 1$  for  $\xi = 0.08$  in Figure 5.5. On this surface, the conventional fixed point  $\mathcal{H}$  is a saddle point. We see that the vector field appears to indeed portray the textbook behavior around a saddle point. We can observe the presence of a stable eigendirection along one diagonal, and an unstable eigendirection along another diagonal.

Due to the fact that the points of  $\mathcal{E}$  on the  $p = \text{constant}$  surfaces are saddles, we find that the mostly assured stability on the  $r = \text{constant}$  slices may more indicative of the long-term behavior of trajectories in the phase space of this model.

### The $\mathbf{v} = 0$ plane

We note that the entirety of  $\mathcal{E}$  resides on the plane  $v = 0$ . This means that we cannot perform the same analysis as we did on the  $r = \text{constant}$  and  $p = \text{constant}$  slices, wherein we only had one fixed point per slice. Thus, the most we can do is to plot the vector field near  $\mathcal{E}$ , and make qualitative assessments of its behavior.

Shown in Figure 5.6 is the vector field of  $(\dot{\mathbf{r}}, \dot{\mathbf{p}})$  around the equilibrium curve  $\mathcal{E}$  on the surface  $v = 0$ . Also specified in the plot the conventional equilibrium point  $\mathcal{H}$ .

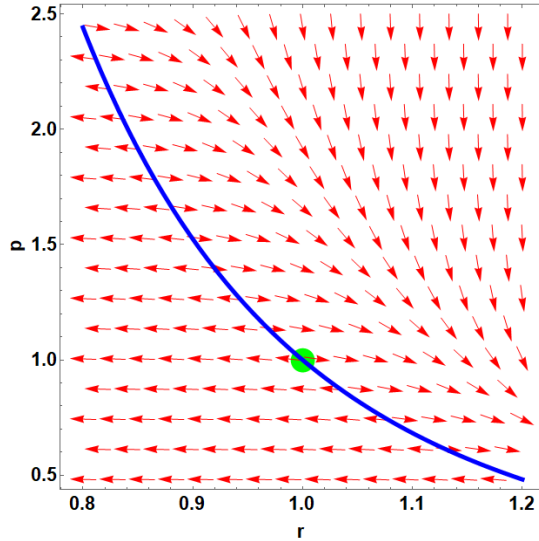


**Figure 5.6:** Vector field  $(\dot{\mathbf{r}}, \dot{\mathbf{p}})$  on the surface  $v = 0$ , for  $\xi = 0.08$ . A section of  $\mathcal{E}$  is shown in blue, and the point  $\mathcal{H}$  is marked in green.

We can see that all the vectors appear to be pointing away from  $\mathcal{E}$ . This entails that along the surface  $v = 0$ ,  $\mathcal{E}$  is unstable. This means that we do not expect any trajectories to approach  $\mathcal{E}$  along this plane. This means that any approaches to  $\mathcal{E}$  would have to be along  $r = \text{constant}$  surfaces or  $p = \text{constant}$  surfaces.

#### Overall assessment of the stability of $\mathcal{E}$

From our results so far, we have shown that all the  $r = \text{constant}$  surfaces for all possible values of  $\xi$  have the fixed points on  $\mathcal{E}$  as either stable spirals or stable nodes. Since these  $r = \text{constant}$  surfaces span the entirety of the phase space, we can conjecture that any trajectories beginning at initial conditions near  $\mathcal{E}$ , such as from a small perturbation from equilibrium, will eventually return to  $\mathcal{E}$ .

It is very important to note however that this return need not be to the same point on  $\mathcal{E}$  the initial perturbation may have taken it away from. Within this model, it is possible for trajectories beginning with initial conditions closest to a point on  $\mathcal{E}$ , say an arbitrary point  $\mathcal{E}_1$ , to eventually settle down to another distinct point on the curve  $\mathcal{E}_2$ . This can be stated by considering a small perturbation  $\eta$  as

$$\mathcal{E}_1 + \eta \rightarrow \mathcal{E}_2. \quad (5.17)$$

The role of the stability on  $p = \text{constant}$  is more difficult to assess, as we know that the points of  $\mathcal{E}$  are saddle points on these slices. Thus, while there is a stable direction to points on  $\mathcal{E}$  along these surfaces, there is also an unstable direction pointing away from the curve. Thus, while it is possible for trajectories to approach  $\mathcal{E}$  along these

stable directions, we are less assured of the overall stability of  $\mathcal{E}$  from our assessment of these  $p = \text{constant}$  surfaces than we are from the  $r = \text{constant}$  surfaces.

The actual behaviors of trajectories in this model, moving through a phase space which is three-dimensional, are of course more complicated than can be described by the vector fields along these two-dimensional sections. The instability on  $v = 0$ , partial stability along  $p = \text{constant}$  slices, and stability on  $r = \text{constant}$  slices are all likely to contribute to the behavior of such trajectories. However, since we have analytically shown that the slices of  $r = \text{constant}$  spanning the entire phase space have fixed points of  $\mathcal{E}$  as stable, we are strongly led to believe that points starting near a point on  $\mathcal{E}$  will eventually end up on  $\mathcal{E}$ . In the next subsection, we will show phase plots of trajectories emanating from near  $\mathcal{H}$  that confirm this expectation.

### 5.3 Phase space trajectories in the Stellingwerf model

We now plot the phase space trajectories of the dynamical system emanating from initial conditions close to  $\mathcal{H}$ . These initial conditions would represent a small perturbation away from the conventional equilibrium state we would expect our star to start out from. These phase plots represent behavior in the three-dimensional phase space, and can show if the dynamical behavior of trajectories is consistent with the generalized linear stability of points on  $\mathcal{E}$  we posited in the last subsection. The specific choice of individual initial conditions was done in a non-systematic fashion.

In Figures 5.7, 5.8, 5.9, and 5.10 we show the trajectories emanating from initial conditions relatively close to  $\mathcal{E}$  for  $\xi = 0.08$ . In all these cases, we see spiralling behavior towards other points along the equilibrium curve  $\mathcal{E}$ .

When we calculate the result of Equation 5.2 for  $\xi = 0.08$ , we see that fixed points on  $\mathcal{E}$  evaluated on  $r = \text{constant}$  slices transition from stable spirals to stable nodes at

$$r_{crit,0.08} \approx 2.29578. \tag{5.18}$$

Thus, since none of these trajectories ever reach this critical value, the appearance of spiral behavior even in the full three-dimensional phase space is consistent with our characterization of the points of  $\mathcal{E}$  on the  $r = \text{constant}$  surfaces. Furthermore, our assessment of the stability of  $\mathcal{E}$  is supported by these results. Our tested trajectories all appear to end on points along  $\mathcal{E}$ .

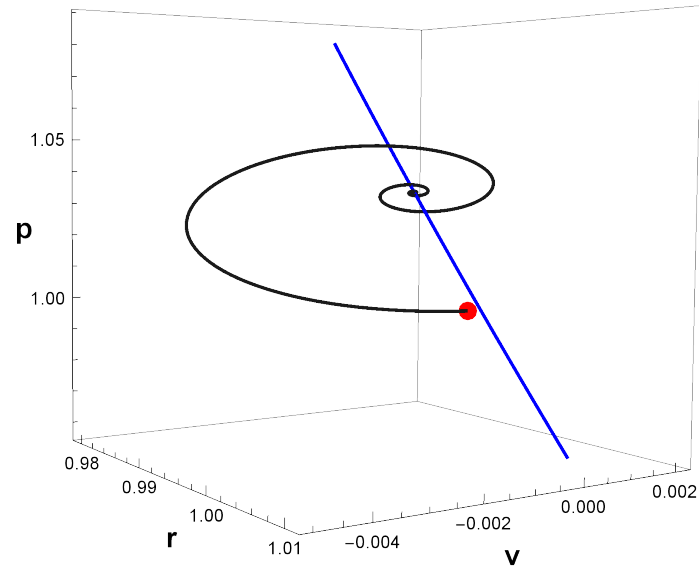


**Figure 5.7:** Phase plot of the Stellingwerf model for  $\xi = 0.08$ , with initial condition  $(0.9986, 0, 0.9986)$  marked in red. The trajectory ends at the point  $(0.991654, 0, 1.03409)$  on  $\mathcal{E}$  shown in blue.

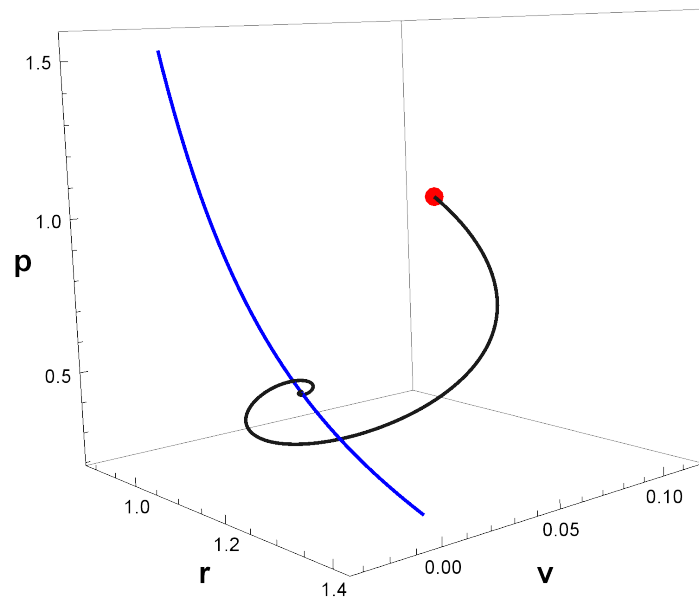


**Figure 5.8:** Phase plot of the Stellingwerf model for  $\xi = 0.08$ , with initial condition  $(1.02, 0.1, 0.98)$  marked in red. The trajectory ends at the point  $(1.18323, 0, 0.510184)$  on  $\mathcal{E}$  shown in blue.

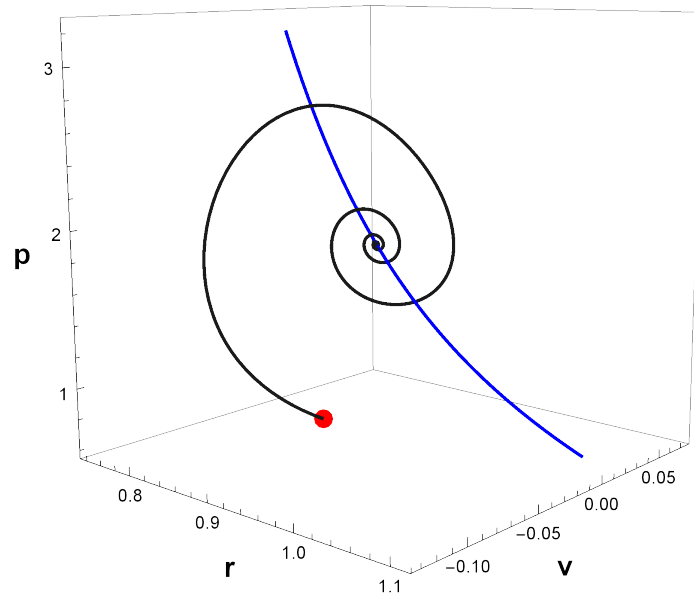


**Figure 5.9:** Phase plot of the Stellingwerf model for  $\xi = 0.08$ , with initial condition  $(0.97, -0.1, 1.04)$  marked in red. The trajectory ends at the point  $(0.865729, 0, 1.78022)$  on  $\mathcal{E}$  shown in blue.

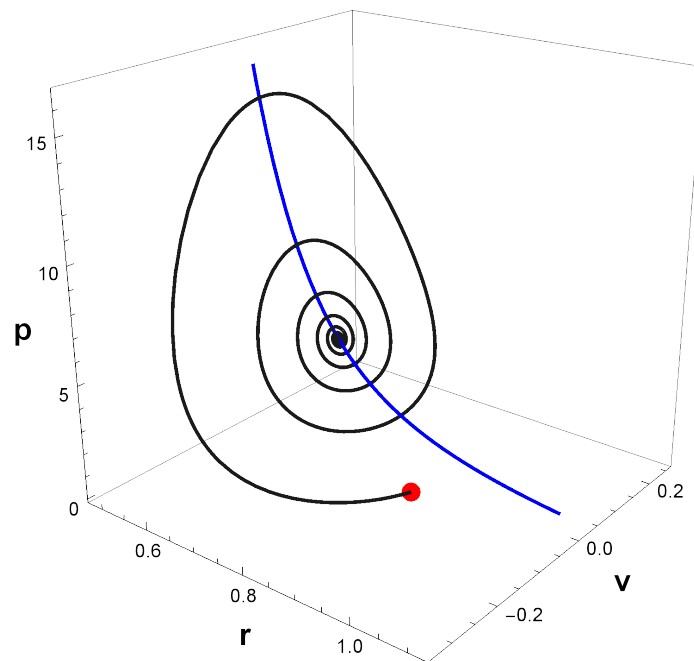


**Figure 5.10:** Phase plot of the Stellingwerf model for  $\xi = 0.08$ , with initial condition  $(0.9, -0.1, 1.1)$  marked in red. The trajectory ends at the point  $(0.668043, 0, 5.02092)$  on  $\mathcal{E}$  shown in blue.

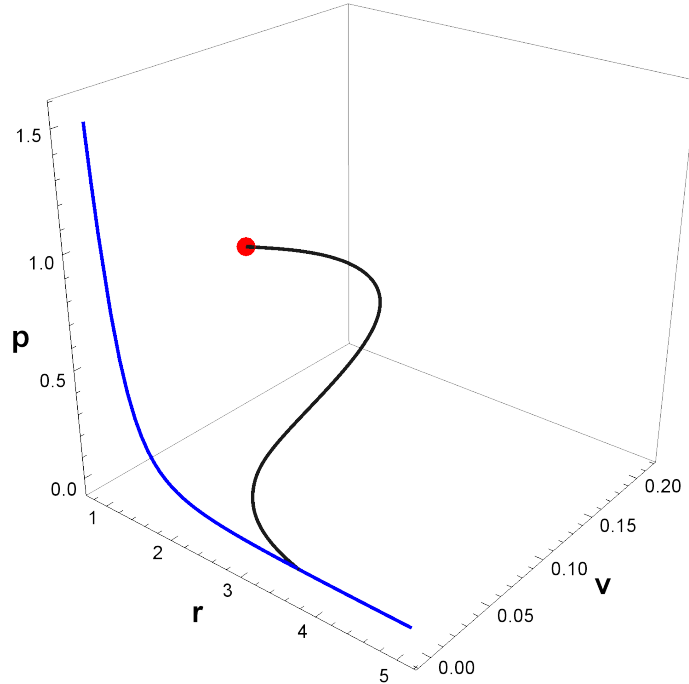


**Figure 5.11:** Phase plot of the Stellingwerf model for  $\xi = 0.08$ , with initial condition  $(1.15, 0.1, 0.8)$  marked in red. The trajectory ends at the point  $(3.59087, 0, 0.00601451)$  on  $\mathcal{E}$  shown in blue.

We now consider a case wherein the trajectory does indeed cross  $r_{crit}$ . In Figure 5.11, we see behavior that unlike the previous examples does not show much spiralling. In fact, we note that the trajectory appears to be what we would expect for an overdamped oscillator. We note that the initial condition chosen for this phase plot does have a rather large perturbation away from from  $r = 1$ , representing a rather large push of the mantle outwards, along with a positive radial velocity  $v$ . This then leads the trajectory to cross  $r_{crit,0.08}$  in its approach towards  $\mathcal{E}$ . This means that past this value of  $r$ , the points of  $\mathcal{E}$  are now described by stable nodes on the  $r = constant$  slices instead of the stable spirals from the previous cases. This likely explains the relatively more straightforward shape of the trajectory, which is consistent with nodes.

It is also interesting to point out that the points on  $\mathcal{E}$  that the trajectories end on are not necessarily the point on  $\mathcal{E}$  that the particular initial condition was closest to. The vector field of the dynamical system does not necessarily require so straightforward a return.

We also find that some sets of initial conditions may lead to a divergence or clearly unphysical results. In Figure 5.12, we find that the trajectory emanating from the initial condition  $(1.1, 0.1, 1.1)$  does not appear to settle on  $\mathcal{E}$  for the duration of

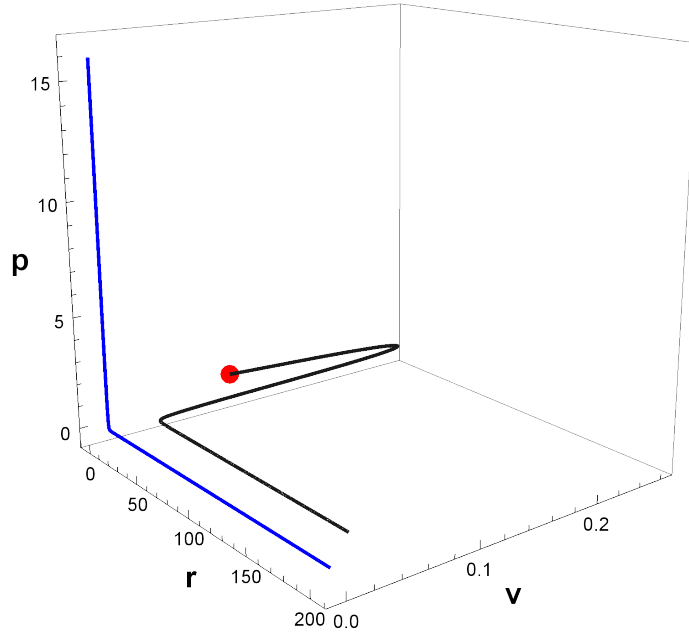


**Figure 5.12:** Phase plot of the Stellingwerf model for  $\xi = 0.08$ , with initial condition  $(1.1, 0.1, 1.1)$  marked in red. The trajectory appears to diverge to unphysical values for the radius.

up to  $t = 1000000$  that the numerical integration to generate this was run up to. It is possible that the chosen initial condition is just too far from  $\mathcal{E}$ , such that the linear stability of the curve on  $r = \text{constant}$  surfaces is not enough to confine this trajectory. It may also be that we have simply not run the numerical integration for a large enough  $t$  to show the trajectory settling on  $\mathcal{E}$ . Note that the sharp corner in the plot of  $\mathcal{E}$  is simply due to us showing the phase space up to  $r = 200$ , which distorts the shape of the curve in order to fit it into the image.

However, a further analysis of this divergence seems unnecessary as the result so far is already wildly unphysical. We note that the initial condition with a positive radial velocity  $v$ , and variations in  $r$  and  $p$  of  $+10\%$ , may possibly no longer be considered as small perturbations away from our conventional equilibrium  $\mathcal{H}$ . Thus, we may be unlikely to expect ever reaching this point of the phase space anyway for a real star, especially since pressure generally scales inversely to the radius.

In future work, the identification of a Lyapunov function that applies to the  $r = \text{constant}$  curves would be useful. This is a type of function used in dynamical systems analysis that would allow us to define a boundary for where the evaluated stability holds [40]. For our case then, this would allow us identify just how far away from  $\mathcal{E}$  our initial conditions may be while still ensuring that trajectories settle onto it.

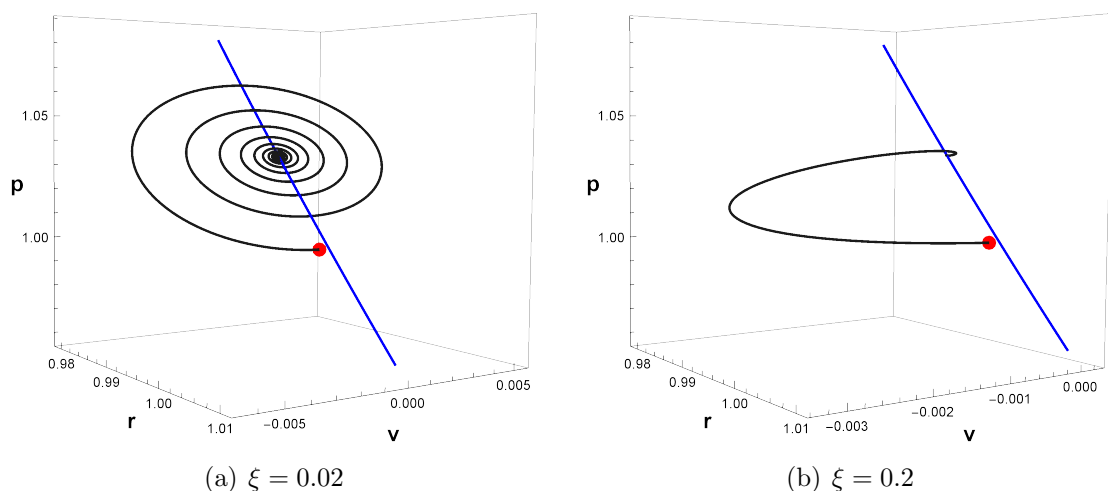


**Figure 5.13:** Phase plots of the Stellingwerf model with initial condition  $(0.9986, 0.1, 0.9986)$  marked in red, for varying  $\xi$ . Both trajectories shown end at the point  $(0.991654, 0, 1.03409)$  on  $\mathcal{E}$ .

## 5.4 Variation of $\xi$ in the Stellingwerf model

We now probe the effect of variation of the strength of the non-adiabaticity  $\xi$  on the shape of trajectories in the model. We recall that for long-period variable stars, we confine our survey to  $0 < \xi \leq 0.2$ .

We plot two trajectories for with the same initial condition  $(0.9986, 0.1, 0.9986)$ , but with different values of  $\xi$  in Figure 5.13. We see that the phase plot for the lower value of  $\xi = 0.02$  appears to show more spiralling than that for  $\xi = 0.2$ . It is interesting to note though that the value of  $\xi$  does not affect the final state of the trajectory, as both cases end up at the point  $(0.991654, 0, 1.03409)$  on  $\mathcal{E}$ . We can confirm that this is also consistent with our phase plot for the same initial conditions and  $\xi = 0.08$  in Figure 5.7.

This effect of the variation of  $\xi$  makes sense when we consider the effect of varying  $\xi$  on Equation 5.11. We recall that when  $Tr(\mathbf{J}_r)^2 - 4Det(\mathbf{J}_r) < 0$ , the fixed points of  $\mathcal{E}$  on our  $r = constant$  slices are spirals. Decreasing the value of  $\xi$  makes this equation more negative, and we thus expect trajectories around such points so exhibit stronger spiral-like behavior.

We further observe that the increase of  $\xi$  leads to a longer amount of time for the trajectories to settle down onto the equilibrium curve  $\mathcal{E}$ . We can perhaps understand this effect by considering that since increasing  $\xi$  makes the fixed point more node-

like, there becomes the increasing development of a preferred direction of attraction. This means that the “strength” of the attraction would generally be weaker in other directions. This can be observed qualitatively when we compare Figures 5.2 and 5.3. Thus, the trajectories corresponding to higher values of  $\xi$  would indeed take a longer amount of time to settle onto the fixed point.

## 5.5 Physical considerations and implications of the behavior of the Stellingwerf model

We have already identified that the fixed points of  $\mathcal{E}$  on  $r = \text{constant}$  surfaces are stable spirals or stable nodes. It then becomes pertinent to discuss what physical correspondences account for this transition from stable spirals to stable nodes.

We assess this transition by first looking at the equation for the radial acceleration  $\dot{v}$ , which flows from Euler Equation’s in Equation 4.14, encapsulating Newton’s 2nd Law. In this equation, we essentially have two competing terms. The first is the term  $pr^2$  corresponding to the pressure pushing outwards. The second term  $r^{-2}$  corresponds to the inward pull of gravity. Since the gravitational term decreases as an inverse square, as the radius  $r$  increases, we expect this term to approach 0. This means that for high values of  $r$ , the pressure term dominates, and we no longer expect much oscillation in the radial velocity  $v$ .

This then accounts for the transition we see at  $r_{crit}$ . For values of the radius  $r$  lower than this, the oscillations in  $v$  are still prominent, and this manifests as spiral-like behavior in phase space. When we now consider values of  $r$  past  $r_{crit}$ , the oscillatory behavior is minimal, and the points of  $\mathcal{E}$  on the  $r = \text{constant}$  surfaces are more node-like. This is akin to the mechanical analogue of the transition from oscillatory behavior in an underdamped system to a much slower approach to equilibrium in an overdamped system. This explains why the trajectory, with values of  $r$  past  $r_{crit}$ , shown in the full three-dimensional phase space in Figure 5.11 resembles what we would expect for an overdamped system.

Now, we turn to the dependence of this transition on the non-adiabaticity  $\xi$ . This can be tackled by assessing the role of  $\xi$  in the equation describing the variation in pressure over time  $\dot{p}$ . As we increase  $\xi$ , heat transfer in the star becomes more efficient, and the magnitude of  $\dot{p}$  is generally higher than if  $\xi$  were lower. This then entails that the pressure term  $pr^2$ , in the radial acceleration equation  $\dot{v}$ , more easily out-competes

the gravitational term. As expected, this leads to less oscillations in  $v$ , which once again means we see less spiralling. This accounts for the observed dependence of the behavior of phase space trajectories on  $\xi$ , that we showed in Figure 5.13. It thus also makes sense that the formula we found for  $r_{crit}$  in Equation 5.2 also shows this inverse dependence on the value of  $\xi$ .

However, we consider that when we solve Equation 5.2 for our non-adiabaticity values of  $0 < \xi \leq 0.2$ , we find that

$$1.59131 \leq r_{crit} < +\infty. \quad (5.19)$$

Since we are considering long-period variable stars, we note that we do not expect variations to lead to the radial extension getting anywhere near as large as  $r = 1.59131$ , as this would correspond to a growth of almost 60% of the radius. Thus, we can say that physically realizable phase space trajectories of this system should be confined to regions wherein the points of  $\mathcal{E}$  are stable spirals on  $r = constant$  surfaces. This further means that solutions such as that shown in the phase plot in Figure 5.11, wherein the trajectory crossed  $r_{crit}$  are unlikely to be physically realizable. This is especially evident when we note that this particular case has a final state wherein  $r = 3.59087$ . We obviously do not expect a star to more than triple its radial extension due to a small perturbation from  $\mathcal{H}$ .

Now, for the solutions with more physically realizable values for the radius, such as in Figures 5.7, 5.8, 5.9, and 5.10, we wish to assess what the behavior of the phase plots entail. The fact that small perturbations away from equilibrium states on  $\mathcal{E}$ , such as  $\mathcal{H}$ , still lead trajectories to other parts of  $\mathcal{E}$ , can be interpreted as the star “hopping” between equilibrium states. This is after some transient behavior in phase space, which for our case is mostly spiral-like behavior.

We may then conclude that the small number of transient oscillations that occur in this model cannot characterize real long-period variable stars. This is because the oscillations of such long-period variable stars are sustained long-term behaviors, and so the predictions of this model do not seem physically realizable for such stars.

It is important to note however that the nature and behavior of the perturbations that bring a star out of its equilibrium configurations are not included in the Stellingwerf model. Thus, it is possible that there is some mechanism that makes the oscillatory behavior of a star with constant opacity exponents  $n = 1$  and  $s = 3$  last for a more sustained period of time. Perhaps the inclusion of time-dependent

convective processes in the model will account for this. However, we are as of now unable to comment on these possibilities.

## 5.6 Equilibrium solutions and transient behavior of the Munteanu model

Now that we have completed our analysis of the case of constant opacity exponents in the Stellingwerf model, we now move on to the analysis of the Munteanu model, wherein the opacity exponents dynamically evolve.

We similarly begin our analysis by finding equilibrium solutions for the Munteanu model aside from  $\mathcal{H}$ . To do this, we set the three differential equations in Equation 4.61 to zero as

$$\begin{aligned} 0 &= v \\ 0 &= pr^2 - r^{-2} \\ 0 &= -3\Gamma_1 r^{-1} vp - \xi r^{-3} \left( r^{a(r^3 p - 1.2) + 21.6} p^{3.6 r^3 p (r^3 p - 0.2)} - 1 \right). \end{aligned} \tag{5.20}$$

Solving these simultaneously gives us three fixed points. Namely, these are  $\mathcal{H}$ ,  $(r^*, v^*, p^*) \approx (0.68, 0, 4.75)$ , and  $(r^*, v^*, p^*) \approx (8.8858, 0, 0.0002)$  [26]. For convenience, we denote these latter two fixed points as  $\mathcal{B}$  and  $\mathcal{C}$  respectively.

The three-dimensional Jacobian matrix would then be

$$\mathbf{J}_M = \begin{pmatrix} \frac{\partial \dot{r}}{\partial r} & \frac{\partial \dot{r}}{\partial v} & \frac{\partial \dot{r}}{\partial p} \\ \frac{\partial \dot{v}}{\partial r} & \frac{\partial \dot{v}}{\partial v} & \frac{\partial \dot{v}}{\partial p} \\ \frac{\partial \dot{p}}{\partial r} & \frac{\partial \dot{p}}{\partial v} & \frac{\partial \dot{p}}{\partial p} \end{pmatrix}_{(r^*, v^*, p^*)}. \tag{5.21}$$

Due to the complicated exponents in the second term of  $\dot{p}$ , stating this Jacobian in full is unwieldy, and is unlikely to give much insight. We thus proceed directly to classifying the fixed points based on the form of the eigenvalues we get from their corresponding Jacobian matrices. We present the classification of the three fixed points in Table 5.1. Munteanu et al. (2003) only identified that these fixed points were unstable, so we have added the specific classification of these fixed points [26].

Given this characterization, we may now proceed to probing the transient behavior of trajectories near these fixed points. We first note that the fixed point  $\mathcal{C}$  has

Fixed Point	Form of eigenvalues	Classification
$\mathcal{H}$	$\mu_1 = 0 \wedge \mu_{2,3} \neq 0, \alpha_1 < 0 \ \& \ \alpha_{2,3} > 0$	<b>Saddle-Focus</b>
$\mathcal{B}$	$\mu_1 = 0 \wedge \mu_{2,3} \neq 0, \alpha_1 > 0 \ \& \ \alpha_{2,3} < 0$	<b>Saddle-Focus</b>
$\mathcal{C}$	$\mu_1 = 0 \wedge \mu_{2,3} \neq 0, \alpha_{1,2,3} > 0$	<b>Unstable Focus-Node</b>

**Table 5.1:** Classification of fixed points in the Munteanu model. Here,  $\alpha_j$  corresponds to the real part of the eigenvalue  $\lambda_j$ , while  $\mu_j$  corresponds to the imaginary part.

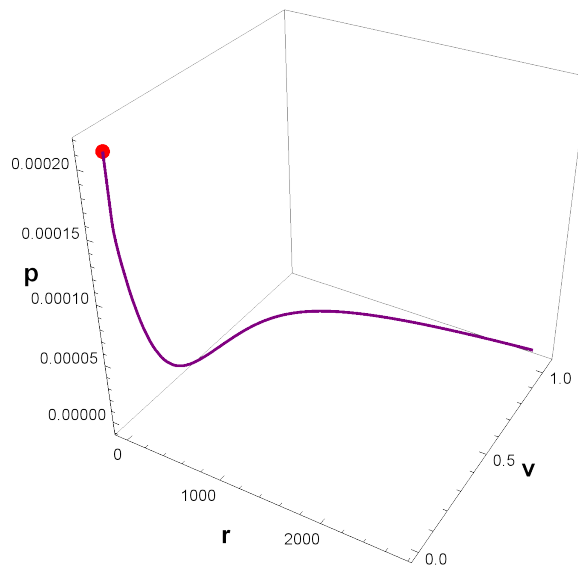


**Figure 5.14:** Phase plot of the Munteanu model for  $\xi = 0.08, a = 20$ , with initial condition near the fixed point  $\mathcal{C}$  marked in red.

$r \approx 8.8858$ , which is clearly unphysical. When we plot a trajectory emanating from this fixed point in Figure 5.14, we notice that the resulting trajectory diverges to even higher values of  $r$ . This is even more clearly an unphysical result. However, since in physical analysis we mostly consider initial conditions near  $\mathcal{H}$ , the presence of this result does not really take away from the model.

We now proceed to transient behavior of trajectories near the conventional fixed point  $\mathcal{H}$ . Shown in Figure 5.15, we see that the trajectory first spirals away from the initial condition near  $\mathcal{H}$ . It then continues to spiral around in larger arcs until it seems to settle down onto a limit cycle. This limit cycle behavior is confirmed when we plot the long-term behavior for  $t \in (2000, 3000)$ , where for  $\xi = 0.08, a = 20$  we have a period-1 limit cycle.

We then move on to our last fixed point  $\mathcal{B}$ . We see in Figure 5.16, that the trajectory appears to initially be repelled from  $\mathcal{B}$ . It then appears to spiral around

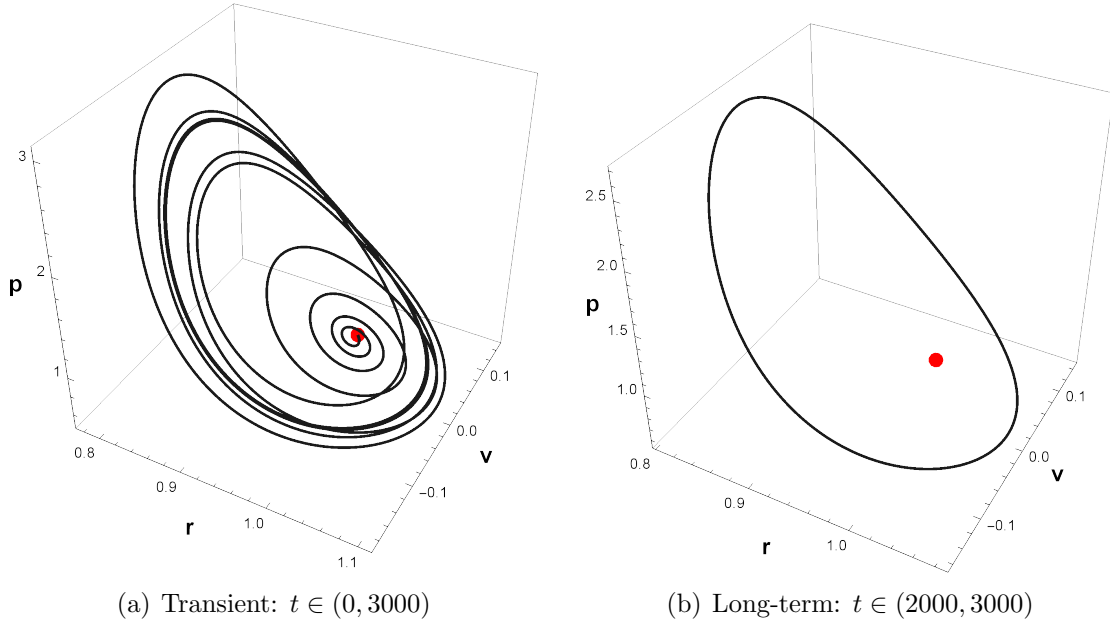


**Figure 5.15:** Phase plots of the Munteanu model for  $\xi = 0.08, a = 20$  with initial conditions near  $\mathcal{H}$  showing transient and long-term behavior. The initial condition is shown in red.

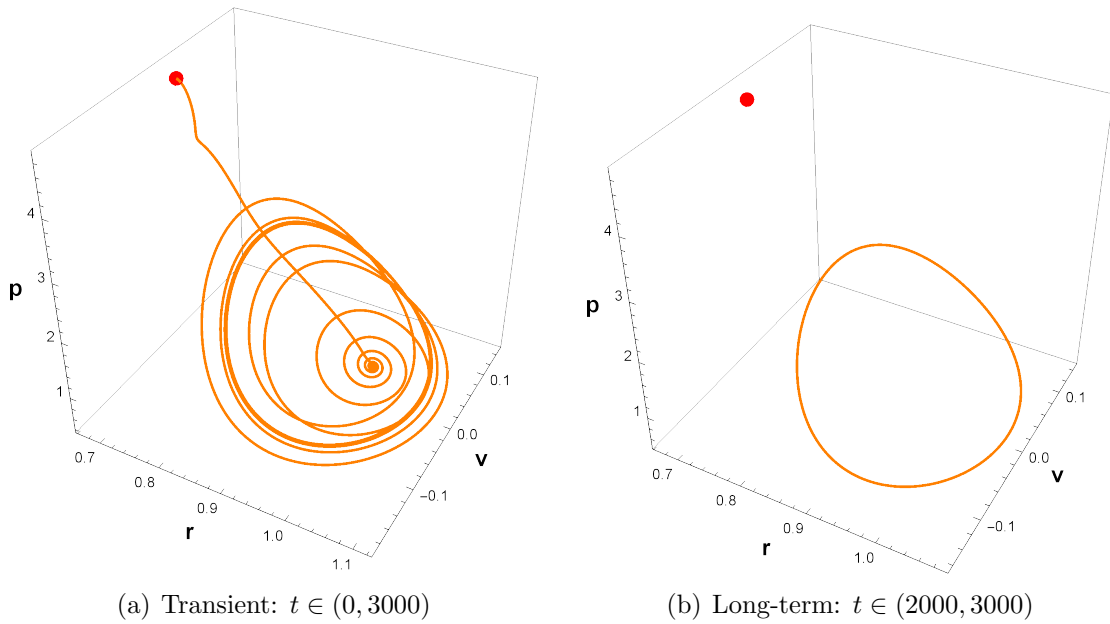


**Figure 5.16:** Phase plots of the Munteanu model for  $\xi = 0.08, a = 20$  with initial conditions near  $\mathcal{B}$  showing transient and long-term behavior. The initial condition is shown in red.

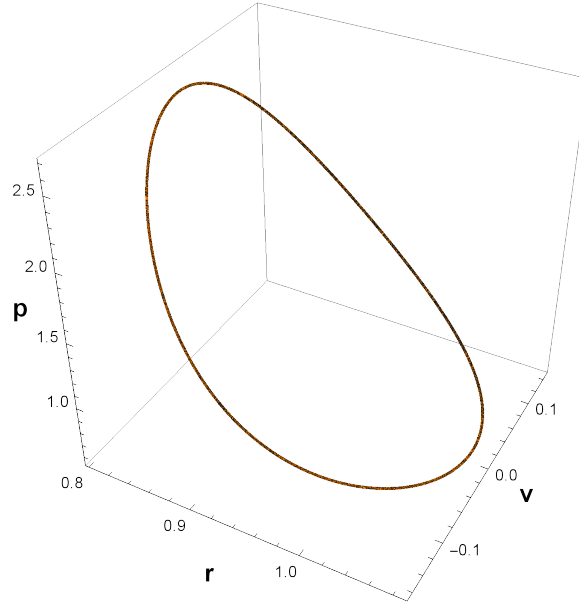


**Figure 5.17:** Trajectories of the Munteanu model for  $\xi = 0.08$ ,  $a = 20$  from near  $\mathcal{H}$  (black) and  $\mathcal{B}$  (orange) settling onto the same limit cycle for  $t \in (2000, 3000)$ .

another region of the phase space. When we plot only the long-term behavior from  $t \in (2000, 3000)$ , we see that it also settles onto a period-1 limit cycle for  $\xi = 0.08$ ,  $a = 20$ .

It appears to be the same limit cycle that we had from initial conditions near  $\mathcal{H}$ . We confirm this by showing the phase plots of both cases for  $t \in (2000, 3000)$ , in the same graph in Figure 5.17. We see that the limit cycle from the trajectory emanating near  $\mathcal{B}$  shown in orange, indeed settles onto the same limit cycle from the trajectory emanating from near  $\mathcal{H}$  shown in black.

We can interpret this behavior physically, as an unstable equilibrium configuration at  $r < 1$ . The star will tend to exhibit behavior nearer to the conventional equilibrium configuration  $\mathcal{H}$ , and that is why we see that in the long term, the behavior of phase plots from near these two distinct fixed points eventually coalesce.

## 5.7 Non-adiabaticity period-doubling route in the Munteanu model

Having identified the presence of limit cycle solutions in the Munteanu model after the cessation of transient behavior, we now move on to expounding on the period-doubling route to chaos from variation in the non-adiabaticity parameter  $\xi$  discussed

in Munteanu et al. (2003) [26]. For this evaluation, the parameter controlling the strength of the  $\kappa$ -mechanism was held at the constant value of  $a = 20$ , and the trajectories considered were those near the conventional fixed point  $\mathcal{H}$ . The period-doubling phenomena can be found from increase of  $\xi$  in the range  $0.08 \leq \xi \leq 0.16$ .

We show this period-doubling route to chaos in Figure 5.18. We see that it is the increase of  $\xi$  that leads to the bifurcation of solutions from a period-1 solution at  $\xi = 0.08$ , to a period-2 solution at  $\xi = 0.09$ , to period-4 at  $\xi = 0.108$ , and then to the chaos at  $\xi = 0.12$  [26].

## 5.8 $\kappa$ -mechanism period-doubling route in the Munteanu model

A similar period-doubling route to chaos but from variation in the  $\kappa$ -mechanism control parameter  $a$  was characterized by Saitou et al. (1989) [37]. This time, the strength of non-adiabaticity is held constant at  $\xi = 0.08$ , and the strength of the  $\kappa$ -mechanism control parameter is varied between  $10.1 \leq a \leq 20$ .

We show this period-doubling from the decrease of  $a$  in Figure 5.20. Decreasing  $a$  from  $a = 20$  to  $a = 16$ , we see a period-1 solution and then a period-2 solution respectively.

For  $a = 15$ , Saitou et al. (1989) reported that for the parameter values  $\xi = 0.08, a = 15$ , that the system exhibited a period-4 solution. They did this by counting the limit cycles shown on the phase plot [37]. However, we find that this is in fact a period-6 solution, and not period-4. Using a Lorenz Map in  $p$ , we more clearly see that in fact we indeed have the 6 points corresponding to a period-6 solution, and not the 4 points we would expect for period-4. This is shown in Figure 5.19, which we previously presented in our work in [43].

We see the presence of a chaotic solution for this period-doubling route when  $a = 13.5$ .

## 5.9 Physical implications of limit cycles and chaotic solutions in the Munteanu model

We recall that long-period variable stars are known to exhibit alternating deep and

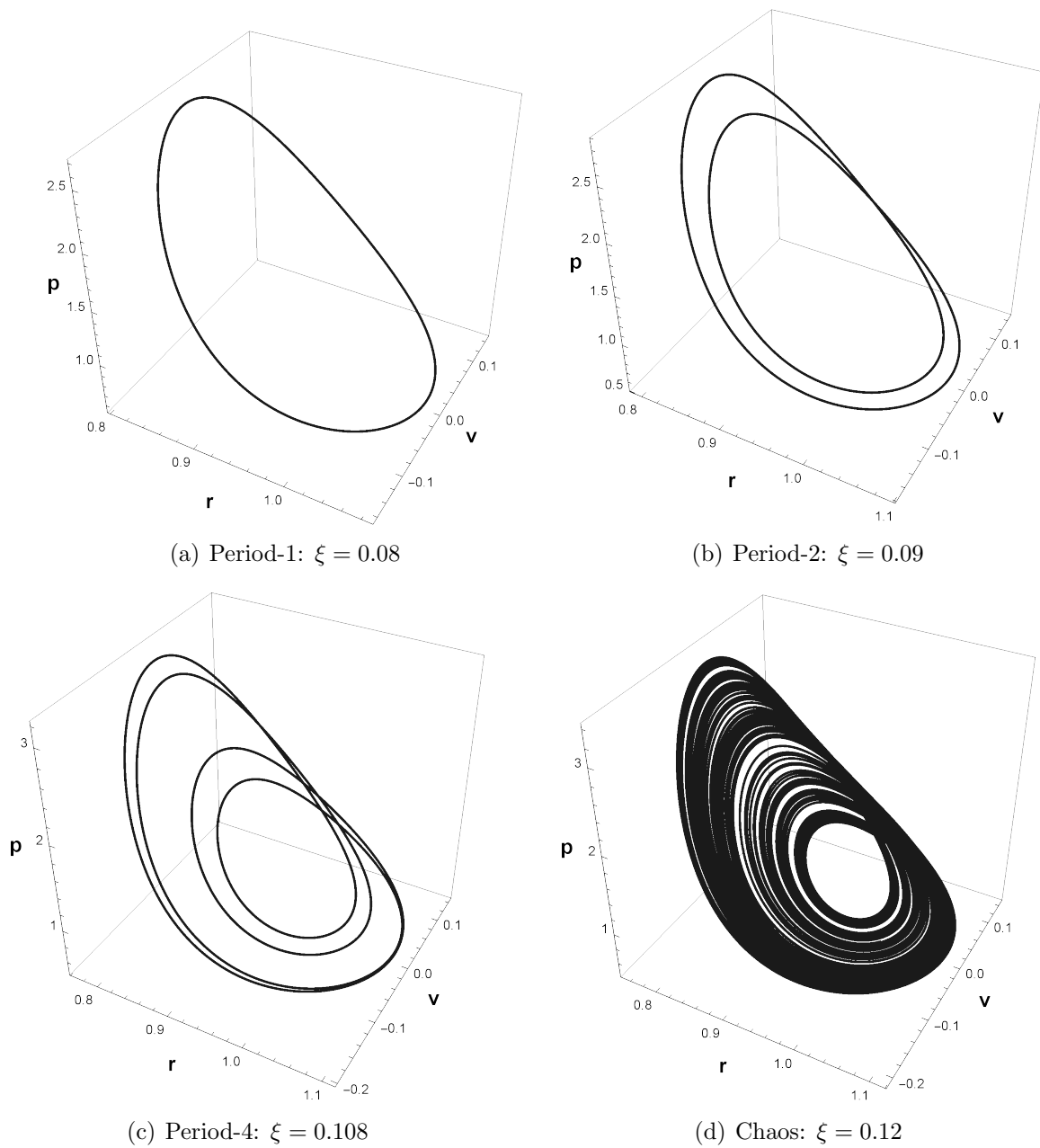


**Figure 5.18:** Phase plots of the Munteanu model with initial conditions near  $\mathcal{H}$  for  $a = 20$ , showing a period-doubling route to chaos from variation in  $\xi$ .

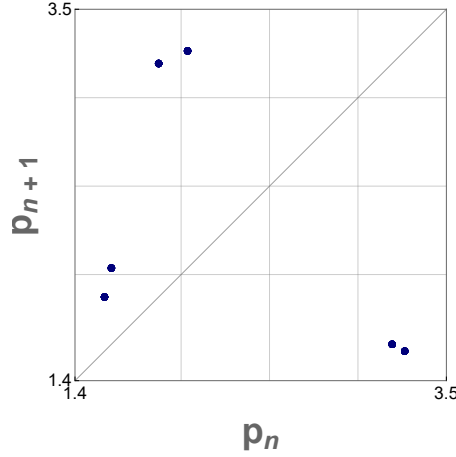


**Figure 5.19:** Lorenz Map in  $p$  of the Munteanu model for parameter values  $\xi = 0.08$ ,  $a = 15$ , showing a period-6 solution. We previously presented this plot in [43].

shallow minima in their light curves [5, 19]. We note that physically, the luminosity  $L$  light curves in fact exhibit two maxima for every one maximum in a cycle of the radius  $r$  or the radial velocity  $v$ . This is because the luminosity has a maximum around both the time when the radius  $r$  is at its maximum, and also when the radius  $r$  is at its minimum and the temperature is increasing [37]. This means that when we say our dynamical system in  $(r, v, p)$  has a period-1 solution, the luminosity would be period-2. This shows the importance of the formation of limit cycles in our phase plots of the Munteanu model, as these limit cycles allow us to replicate the behavior alternating deep and shallow minima you would expect for a period-2 or higher light curve.

We recall from our derivation in Chapter 4 that the normalized luminosity  $\ell$  can be given by

$$\ell \equiv \frac{L}{L_\star} = r^\beta p^\delta. \quad (5.22)$$

This then allows us to plot the time-series or light curve of  $\ell$  next to the time-series of  $r$ , so that this proportionality in their periodicities can be seen. We show this for a period-1 case in  $r(t)$  and corresponding period-2 case in  $\ell(t)$  in Figure 5.21. In these time-series, we use our dimensionless time  $t$ , which we recall is defined as  $t = \omega_\star \tau$ , where the characteristic frequency is  $\omega_\star = \sqrt{\frac{GM}{R_\star^3}}$ .

The chaotic solutions of the model are important, as we know that some long-period variable stars do in fact possess low-dimensional chaos [7]. We of course expect that a chaotic solution in one of our state variables such as  $r$  would also entail chaos

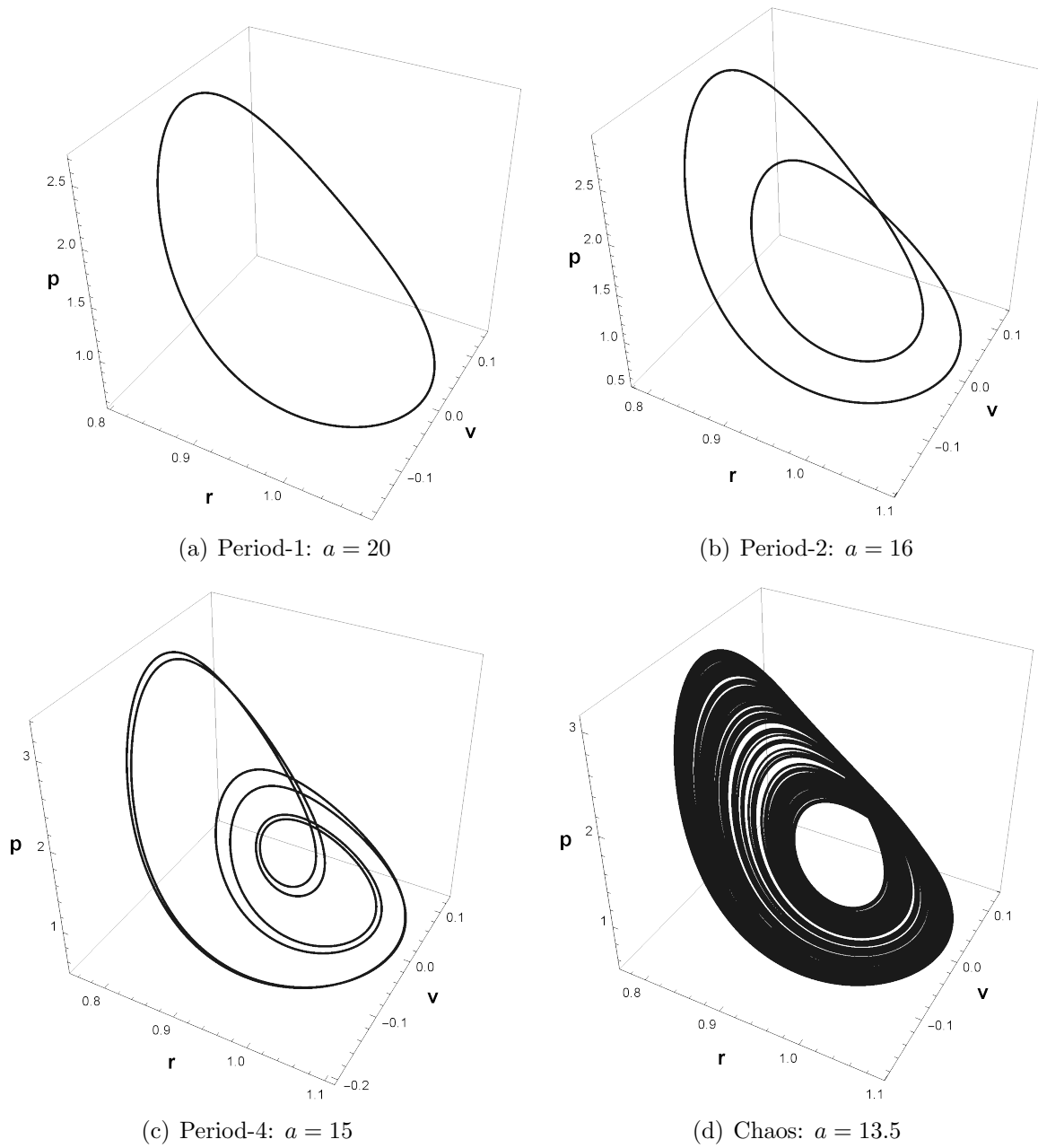


**Figure 5.20:** Phase plots of the Munteanu model with initial conditions near  $\mathcal{H}$  for  $\xi = 0.08$ , showing a period-doubling route to chaos from variation in  $a$ .

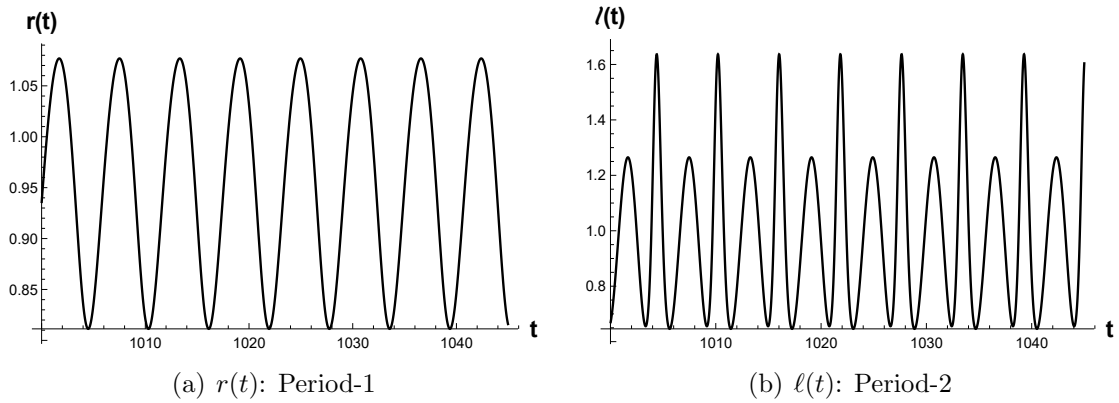


**Figure 5.21:** Time-series of  $r(t)$  and  $l(t)$  in the Munteanu model showing the corresponding proportionality in their periodicities for  $\xi = 0.08, a = 20$ . Here,  $t$  is our dimensionless time  $t = \omega_* \tau$ .

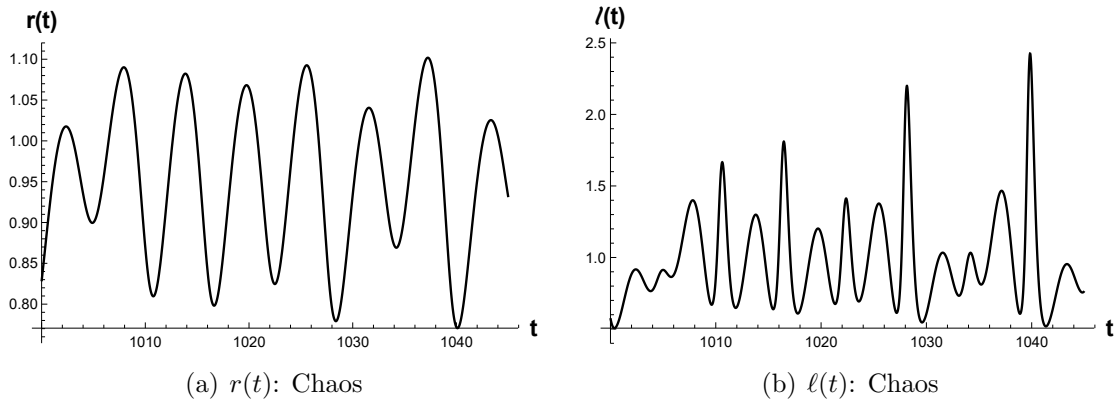


**Figure 5.22:** Time-series of  $r(t)$  and  $l(t)$  in the Munteanu model showing chaotic oscillations for  $\xi = 0.12, a = 20$ . Here,  $t$  is our dimensionless time  $t = \omega_* \tau$ .

in the luminosity  $l$ . Even though these are chaotic, and it is difficult to probe this simply by inspection, we present the time-series of  $r(t)$  and  $l(t)$  for a chaotic solution in Figure 5.22.

Now that we have discussed the dynamical behavior of both the Stellingwerf and Munteanu models, we move on to a deeper analysis of the chaotic regime of the Munteanu model in the next chapter.

# Chapter 6

## Strange attractors of stellar pulsation in the Munteanu model

All memories are traces of tears.

---

*Wong Kar-Wai*  
2046

In the presentation of the phase plots and time-series of chaotic solutions of the Munteanu model in the previous chapter, the chaotic nature of the curves were inferred merely from visual inspection. In this chapter, we use the tools developed in Chapter 3 in order to better characterize the strange chaotic attractors of the Munteanu model.

We first begin by the presentation of the Lorenz Maps of the pressure  $p$  and the radial velocity  $v$  for both the non-adiabaticity route and the  $\kappa$ -mechanism route to chaos. This allows us to more easily compare the geometric forms of the strange attractors corresponding to chaotic solutions from these two routes.

We then move on to our reconstruction of the strange attractors using time-delay embeddings. We identify the minimum embedding dimension and appropriate delay times.

### 6.1 Period-doubling route to chaos in Lorenz Maps of the pressure $p$

In order to present the period-doubling route to chaos for both the non-adiabaticity and  $\kappa$ -mechanism routes, we first present the Lorenz Maps of the pressure  $p$  showing the said period-doubling phenomena.

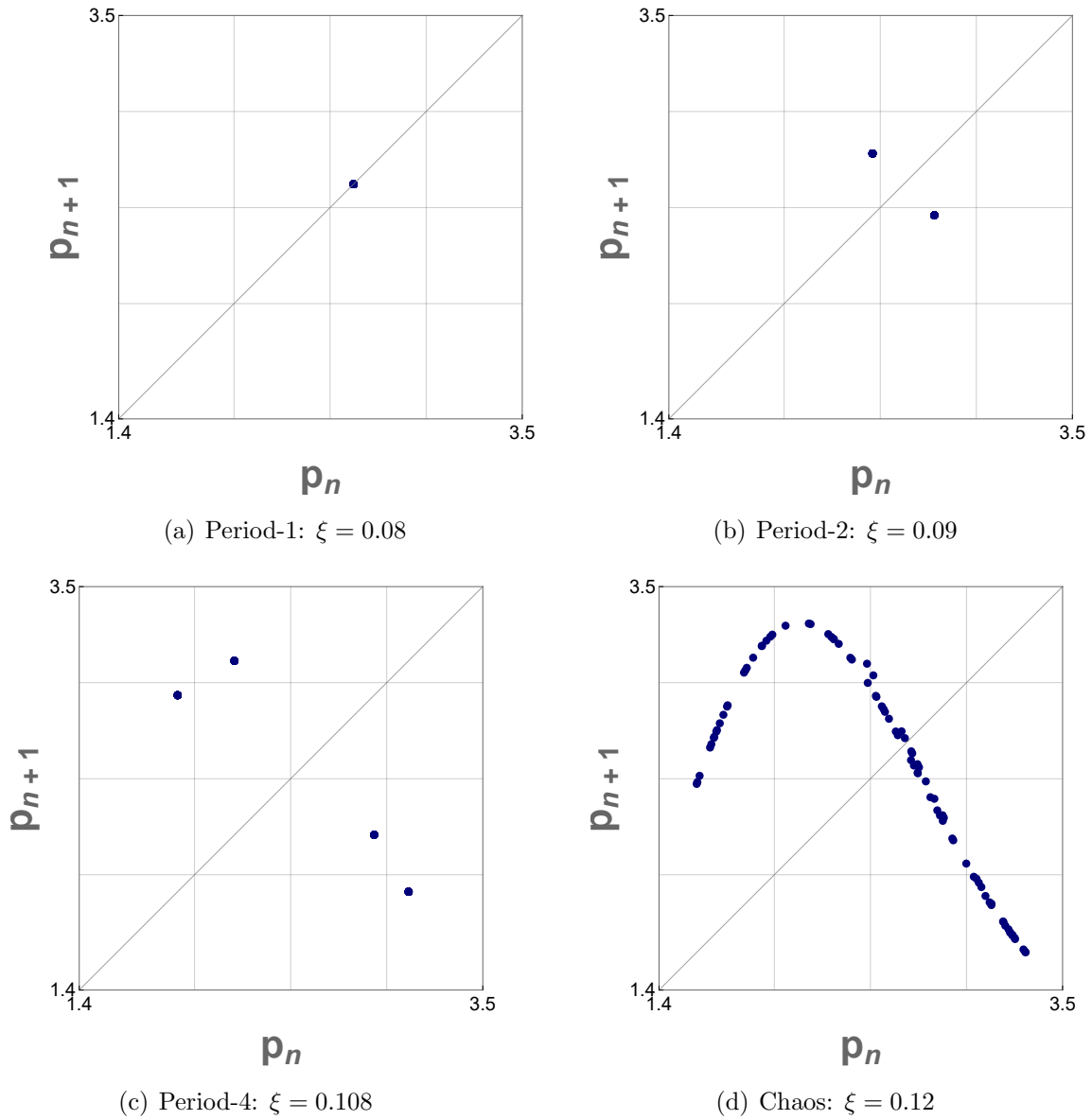


**Figure 6.1:** Lorenz Maps of  $p$  of the Munteanu model  $a = 20$ , showing a period-doubling route to chaos from variation in  $\xi$ . We previously presented these plots in [43].

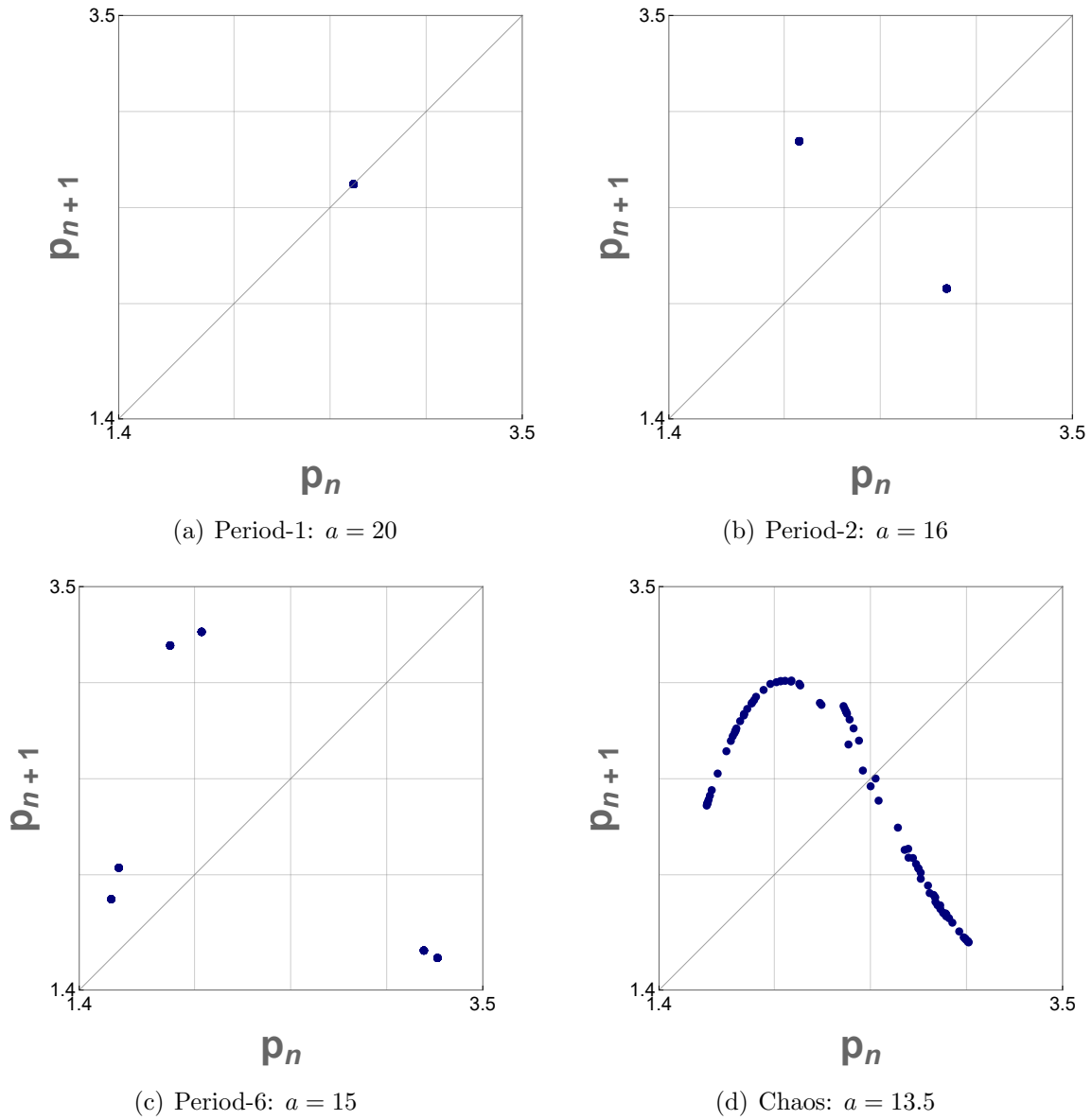


**Figure 6.2:** Lorenz Maps of  $p$  of the Munteanu model  $\xi = 0,08$ , showing a period-doubling route to chaos from variation in  $a$ . We previously presented these plots in [43].

We show the period-doubling route from the variation in the parameter controlling the amount of non-adiabaticity  $\xi$  in Figure 6.1, which we previously presented in [43]. We see that the period-1, period-2, and period-4 solutions are more easily determined by simply counting the corresponding number of points.

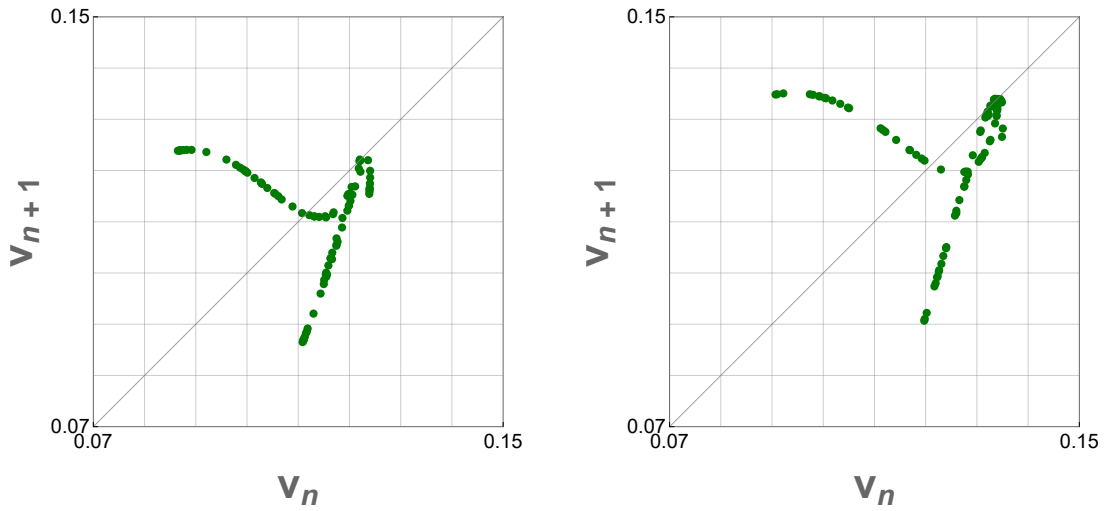
The period-doubling route from variation in the strength of the  $\kappa$ -mechanism  $a$  is shown in Figure 6.2, which we also previously presented in [43]. This time, we show period-1, period-2, and period-6 solutions.

When we compare the forms of the Lorenz Maps for the chaotic solutions from both routes to chaos, we see what appears like an inverted parabola in both cases. This similarity points to a similarity in the structure of the strange attractor from these two distinct routes to chaos, for these specific parameter values. This shape is similar to a Lorenz Map of the Rössler system [1]. Thus, it is possible that the Munteanu attractor may share some similarities to the dynamics of the Rössler attractor that can be expounded upon in future work.

## 6.2 Lorenz Maps of the radial velocity $v$

The study of Saitou et al. (1989) made use of Lorenz Maps maps in  $v$  for comparison with observational luminosity Lorenz Maps of long-period variable stars [37]. This was done because maxima of radial velocity  $v$ , are said to have correspondence with half of the luminosity  $\ell$  maxima. We may recall from the previous chapter, that luminosity  $\ell$  exhibits two maxima for every one maxima of  $r$  or  $v$ . Thus, Saitou et al. (1989) considered that radial velocity Lorenz Maps would prove to be a suitable comparison with the observational luminosity data of long-period variables available at the time. The reason that Lorenz Maps of the luminosity were not rendered directly is that since  $\ell = r^\beta p^\delta$  is a rather complicated term, the chaotic solutions would present much difficulty in use for comparisons [37].

Considering that we now have modern space telescopes such as Kepler, Gaia, the Transiting Exoplanet Survey Satellite, and other more advanced observational systems, there is also some capability in directly measuring the radial velocity of stellar surfaces [13]. This means that Lorenz Maps of the radial velocity  $v$  can potentially be used as direct probes of the strange attractors of chaotic long-period variables in nature. Direct comparison of  $v$  Lorenz Maps of one-zone models with observational luminosity  $\ell$  return maps may no longer be necessary in the future. This is helpful,



(a)  $\kappa$ -mechanism route:  $a = 13.5$ ,  $\xi = 0.08$       (b) Non-adiabaticity route:  $a = 20$ ,  $\xi = 0.12$

**Figure 6.3:** Lorenz Maps of the radial velocity  $v$  showing “ $y$ ”-shaped structures from both routes to chaos. We previously presented these plots in [43].

as we need not lose information about the second luminosity  $\ell$  maxima in each cycle that  $v$  exhibits no correspondence to.

It had previously been found by Saitou et al. (1989), that within the chaotic regime corresponding to variation in the strength of the  $\kappa$ -mechanism, the range  $13.5 \leq a \leq 14$ , for  $\xi = 0.08$ , had Lorenz Maps of  $v$  exhibiting a “ $y$ ”-shaped structure. Furthermore, they found that the Semiregular variable star S Vul WY And showed “ $y$ ”-shaped observational luminosity Lorenz Maps matching these synthetic  $v$  Lorenz Maps [37].

We discovered that the non-adiabaticity route to chaos also produces strange attractors with similarly shaped Lorenz Maps of  $v$ . This is found for  $a = 20$  within the parameter range  $0.11 \leq \xi \leq 0.125$ . We previously presented this result in [43].

It becomes evident that the strange attractors from both the  $\kappa$ -mechanism  $a$  and non-adiabaticity  $\xi$  routes to chaos, for these parameter values, must have very similar features due to the striking similarity in the “ $y$ ”-shaped morphology of the Lorenz Maps as shown in Figure 6.3. As previously discussed in Chapter 4, the  $\kappa$ -mechanism and the non-adiabaticity generally correspond to different physical processes. Thus, it is definitely interesting that the Munteanu model predicts the chaos resulting from these two different routes to have such similar strange attractors, as seen in the Lorenz Maps.

It is possible that the similarity in the forms of the strange attractors from both these routes present actual possibilities for the forms of chaos in long-period variables in nature. Going back to the work of Saitou et al. (1989), they did not present an analysis of the physical processes of the Semiregular variables S Vul and WY And that showed the “ $y$ ”-shaped observational luminosity Lorenz Maps. Thus, it cannot be concluded with finality that those stars got their “ $y$ ”-shaped Lorenz Maps from the  $\kappa$ -mechanism  $a$  route to chaos. The non-adiabaticity  $\xi$  route thus presents a valid alternative source of these shapes.

We further consider that some Mira variables, being cooler, may have values of the non-adiabaticity  $\xi$  higher than that for the RV Tauri and Semiregular variables presented in the work of Saitou et al. (1989), where the non-adiabaticity was held constant at  $\xi = 0.08$ . It is possible that the non-adiabaticity chaotic regime corresponding to  $a = 20$ ,  $0.11 \leq \xi \leq 0.125$ , may mean that some Mira variables may tend to exhibit such “ $y$ ”-shaped Lorenz Maps. As we previously noted in our previous work, since there are many similarities in the pulsations of RV Tauris, Semiregulars, and Miras, this outcome may not be totally surprising [43]. It would definitely be interesting though if it can be shown in the future that similarities in chaotic pulsations between these different types of long-period variables can be attributed to routes to chaos from the differing physical parameters corresponding to the  $\kappa$ -mechanism and the non-adiabaticity.

However, as we also posited in our previous work, it may be the case that the similarities in the forms of the strange attractors as revealed in the  $v$  Lorenz Maps are simply a degeneracy within the model and do not correspond to similarities exhibited by these stars in nature [43]. We reiterate that one-zone models are very simplified models, and thus this would not be an entirely surprising explanation for this similarity.

### 6.3 Time-delay embedding reconstruction of the strange attractors

In a similar but perhaps more robust spirit to the use of Lorenz Maps to characterize the strange attractors using only one state variable, we perform a time-delay reconstruction of the phase spaces of chaotic solutions of the Munteanu model. As discussed in Chapter 3, Takens’ Theorem allows us to reconstruct the topological form

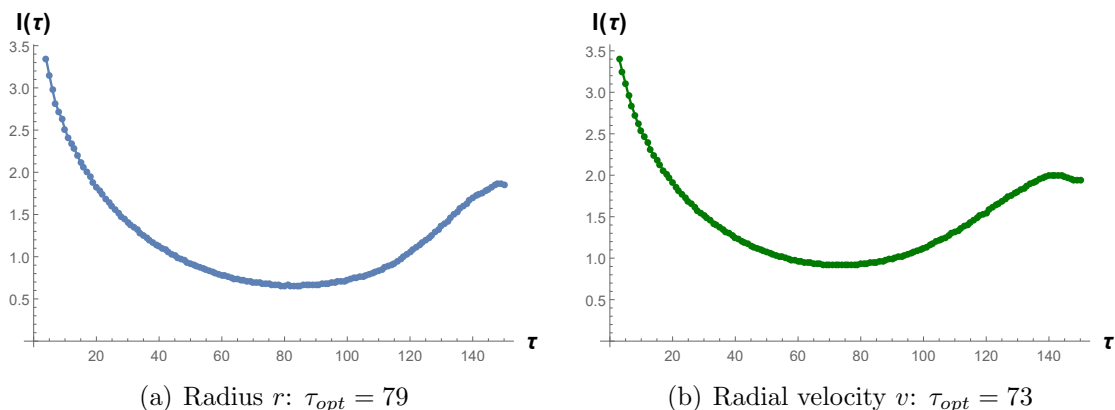


**Figure 6.4:** Plots of average mutual information  $I(\tau)$  for the state variables  $r$  and  $v$ , for the  $\kappa$ -mechanism route to chaos:  $a = 13.5, \xi = 0.08$ .

of a strange attractor using only a single state variable [41]. By this reconstruction of the strange attractors of the Munteanu model, we attain measures of the optimal delay time  $\tau_{opt}$  and embedding dimension  $d_e$ . These values can then potentially be used in future work for comparison with attractor reconstructions arising from observational data of chaotic long-period variable stars. There has already been work done on time-delay embedding strange attractor reconstruction from observational data for some chaotic astrophysical phenomena such as in X-ray binaries and some long-period variable stars [30, 32].

So as to further our characterization of the chaotic solutions that produced the “ $y$ ”-shaped Lorenz Maps, we focus our reconstructions on the solutions with parameter values  $a = 13.5$  and  $\xi = 0.08$  corresponding to the  $\kappa$ -mechanism route to chaos, and  $a = 20$  and  $\xi = 0.12$  corresponding to the non-adiabaticity route to chaos. For both these cases, we calculate the optimal delay time  $\tau_{opt}$  and embedding dimension  $d_e$ . We perform time-delay reconstructions using the radius  $r$  and radial velocity  $v$ , to see if there is any variable dependence exhibited by  $\tau_{opt}$  and  $d_e$ . Performing reconstructions in both  $r$  and  $v$  may also allow for an increased applicability of this work in the future, depending on what observational data is available for long-period variables.

Using the *Mathematica*® package of Ruskeepää, we first find the optimal values of the delay time  $\tau$  using the method of average mutual information, where we have chosen a bin width of 0.01 [36].

We show the plots of the average mutual information  $I(\tau)$  for varying  $\tau$ , using both  $r$  and  $v$  as the chosen state variables, for both the  $\kappa$ -mechanism route and the

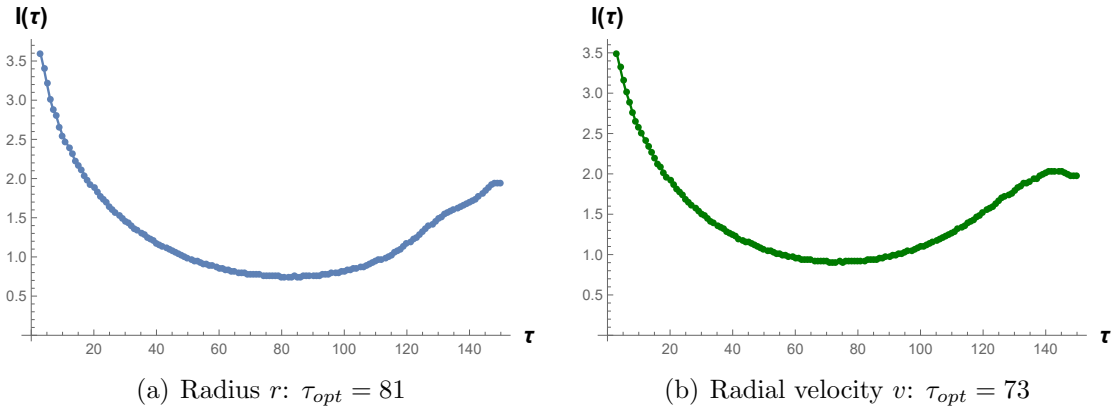


**Figure 6.5:** Plots of average mutual information  $I(\tau)$  for the state variables  $r$  and  $v$ , for the non-adiabaticity route to chaos:  $a = 20, \xi = 0.12$ .

non-adiabaticity route in Figures 6.4 and 6.5 respectively. We see that the plots of the average mutual information  $I(\tau)$  show roughly the same form for all four cases.

When time-series of  $r$  are used for the time-delay embedding, we get an optimal delay time of  $\tau_{opt} = 79$  for the case of the  $\kappa$ -mechanism route, and  $\tau_{opt} = 81$  for the case of the non-adiabaticity route. Since, as we stated, the selection of an optimal delay time  $\tau_{opt}$  is rather arbitrary, the differences between these two values may be considered negligible. Thus, we can say that the optimal time delay when  $r$  is used as the state variable is  $\tau_{opt} \approx 80$ . For the case when time-series of  $v$  are used, we get an optimal delay time  $\tau_{opt} = 73$  for both cases. This similarity in the optimal delay times  $\tau_{opt}$  between these two differing routes to chaos, for both  $r$  and  $v$ , furthers our claim that the structures of the strange attractors from these two cases are very similar.

Now that the optimal delay times  $\tau_{opt}$  have been calculated, the minimum embedding dimension  $d_e$  can now be found using the method of false nearest neighbors. In Table 6.1, we show the percentage of false nearest neighbors for varying embedding dimension  $d_e$ . We see that when the radius  $r$  is used as the state variable for the time-delay reconstruction, the percentage of false nearest neighbors already falls to zero when  $d_e = 3$  for both the  $\kappa$ -mechanism and non-adiabaticity routes to chaos. Thus, this may be considered as the optimal embedding dimension when  $r$  is used.

However, when we use the radial velocity  $v$  for the embedding, the percentage of false nearest neighbors only falls to zero starting when  $d_e = 4$ , for both routes to chaos. This poses a bit of difficulty, as plotting something in four dimensions is obviously quite challenging. We note that the percentage of false nearest neighbors

Route to Chaos	State variable	Embedding dimension $d_e$	Percentage of false nearest neighbors (%)
<b><math>\kappa</math>-mechanism:</b> $a = 13.5, \xi = 0.08$	Radius: $r$	1	99.6227
		2	19.8836
		3	0
		4	0
		5	0
	Radial velocity: $v$	1	99.5608
		2	22.6
		3	0.48252
		4	0
		5	0
<b>Non-adiabaticity:</b> $a = 20, \xi = 0.12$	Radius: $r$	1	99.55489
		2	19.5756
		3	0
		4	0
		5	0
	Radial velocity: $v$	1	99.6551
		2	18.0215
		3	0.23682
		4	0
		5	0

**Table 6.1:** Percentage of false nearest neighbors for varying embedding dimension  $d_e$ , for both state variables  $r$  and  $v$ , in both the  $\kappa$ -mechanism and non-adiabaticity routes to chaos.

is on the order of tenths of a percent when  $d_e = 3$ , thus it is possible that  $d_e = 3$  may also be a suitable embedding dimension for time-delay reconstructions using  $v$ . Nonetheless, we are more assured that  $d_e = 4$  is the optimal embedding dimension for embeddings using the radial velocity  $v$  as the chosen state variable.

We present a summary of the results for finding optimal values of the time delay and embedding dimension in Table 6.2. Using this information, we are now able to plot the reconstructed phase spaces using time-delay embeddings in  $r$  and  $v$ . We present these in three dimensions for all cases, since we are unable to plot the reconstructions using  $v$  in four dimensions.

The time-delay embedding reconstructions using  $r$  for the  $\kappa$ -mechanism and non-adiabaticity routes to chaos are shown in Figures 6.6 and 6.7 respectively. We show the effect of increasing the delay time  $\tau$  up to  $\tau_{opt}$ . We see that the points of the phase plot seem to spread out more evenly along the axes until we reach the corresponding optimal delay time  $\tau_{opt}$ . By inspection, we see that the forms of the plots for both routes to chaos look very similar. It is also interesting to observe that when  $\tau = 40$ , the

Route to Chaos	State variable	Optimal time delay	Optimal embedding dimension
		$\tau_{opt}$	$d_e$
$\kappa$ -mechanism $a = 13.5, \xi = 0.08$	Radius: $r$	79	3
	Radial velocity: $v$	73	4
Non-adiabaticity: $a = 20, \xi = 0.12$	Radius: $r$	81	3
	Radial velocity: $v$	73	4

**Table 6.2:** Summary of the optimal time delay  $\tau_{opt}$  and embedding dimension  $d_e$  for state variables  $r$  and  $v$  in the time-delay embedding reconstructions of the strange attractors from both the  $\kappa$ -mechanism and non-adiabaticity routes to chaos.

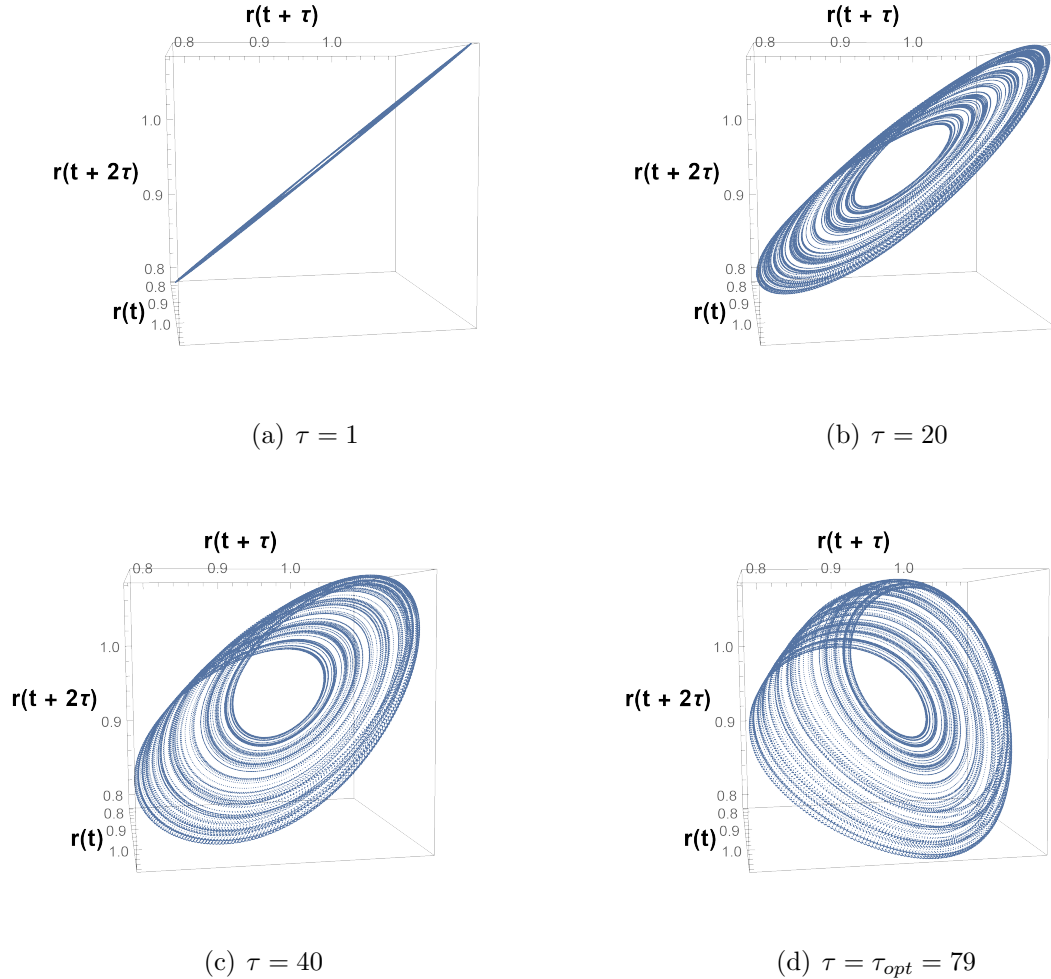
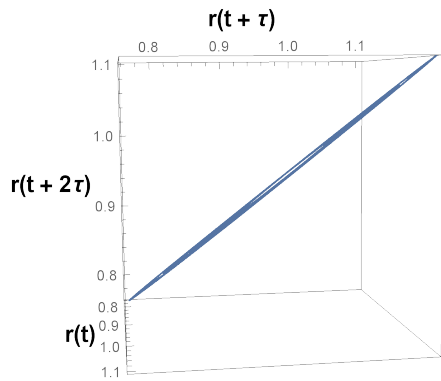
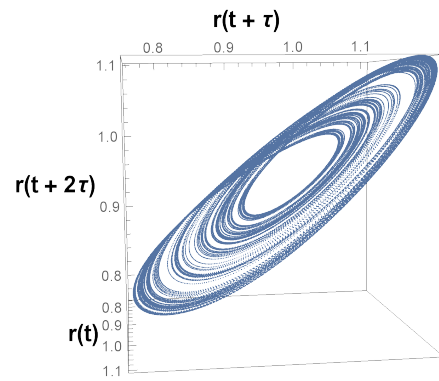


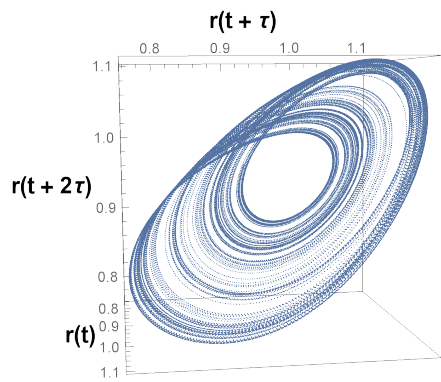
**Figure 6.6:** Plots of the time-delay embedding reconstruction using the radius  $r$  with varying delay time  $\tau$  for the  $\kappa$ -mechanism route to chaos wherein  $a = 13.5, \xi = 0.08$ .



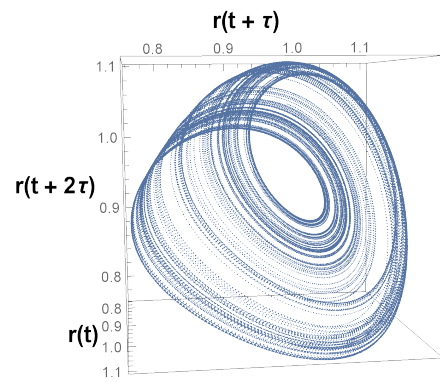
(a)  $\tau = 1$



(b)  $\tau = 20$



(c)  $\tau = 40$



(d)  $\tau = \tau_{opt} = 81$

**Figure 6.7:** Plots of the time-delay embedding reconstruction using the radius  $r$  with varying delay time  $\tau$  for the non-adiabaticity route to chaos wherein  $a = 20, \xi = 0.12$ .

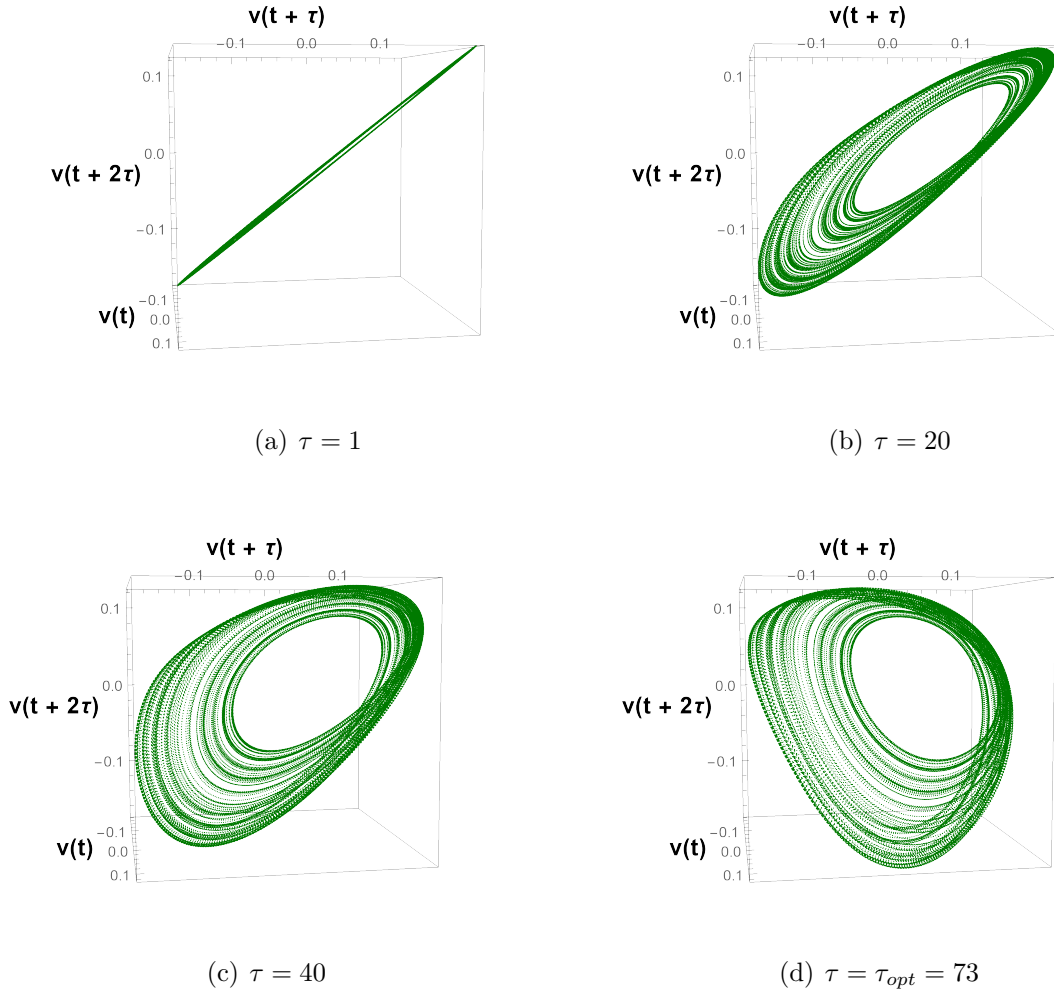


**Figure 6.8:** Plots of the time-delay embedding reconstruction using the radial velocity  $v$  with varying delay time  $\tau$  for the  $\kappa$ -mechanism route to chaos wherein  $a = 13.5, \xi = 0.08$ .

time-delay reconstruction plots using  $r$  even seem to closely resemble the qualitative shapes of the original chaotic phase plots using all the original state variables  $(r, v, p)$  shown in Figures 5.18 and 5.20. While qualitative, this resemblance does lead us to more easily believe that there exists a smooth invertible map between a time-delay embedding reconstruction and the original phase space as posited by Takens' Theorem [41].

We now similarly present the time-delay embedding reconstructions using  $v$  for both the  $\kappa$ -mechanism and non-adiabaticity routes to chaos in Figures 6.8 and 6.9. As previously stated, we plot these in three dimensions, in contrast to the optimal embedding dimension of  $d_e = 4$ , due to the difficulty of visualizing a four dimensional

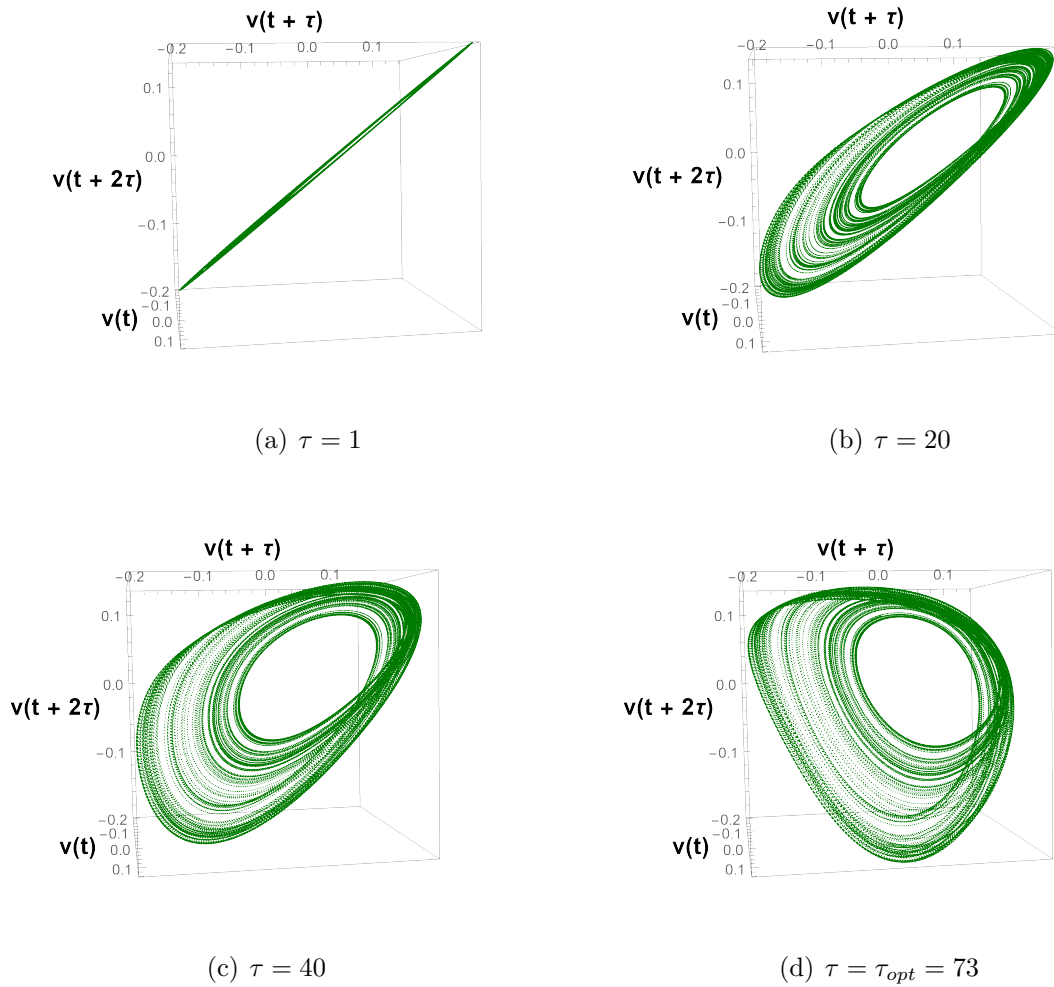


**Figure 6.9:** Plots of the time-delay embedding reconstruction using the radial velocity  $v$  with varying delay time  $\tau$  for the non-adiabaticity route to chaos wherein  $a = 20, \xi = 0.12$ .

plot. The fact that the percentage of false nearest neighbors is still very low for  $d_e = 3$  indicate that these three-dimensional reconstructions may still be suitable. We once again notice that the reconstructions of from both routes to chaos resemble one another. While the qualitative resemblance to the original phase space plots of  $(r, v, p)$  in Figures 5.18 and 5.20 is not as evident in our time-delay reconstructions using  $v$  as in the ones using  $r$ , we still see the presence of some features like the wide opening that exhibits the absence of any trajectories.

Having found the optimal delay times and embedding dimensions for what appeared as “ $y$ ”-shaped strange attractors in Lorenz Maps, these time-delay embedding reconstructions may serve as another basis for testing the possible validity of the Munteanu model when compared to observational data of real long-period variable stars.

# Chapter 7

## Conclusions and further work

Death closes all: but something ere the end,  
Some work of noble note, may yet be done,  
Not unbecoming men that strove with Gods.

---

*Alfred, Lord Tennyson*  
*Ulysses*

### 7.1 Summary and conclusions

We explored two one-zone models of stellar pulsation with parameter values corresponding to long-period variable stars. In the first model, we considered the constant opacity exponents  $n = 1$  and  $s = 3$ , as proposed by Stellingwerf (1972) [38]. The second model we considered was the autonomous Munteanu (2003) model, which now made use of the dynamically evolving opacity exponents put forward by Saitou et al. (1989) [26, 37].

Using a dynamical systems approach, we sought to find equilibrium solutions of the Stellingwerf model of constant opacity exponents by solving the equations of motion in terms of the radius, radial velocity, and pressure on the shell  $(r, v, p)$ . Our novel result is that the Stellingwerf model of constant opacity exponents exhibits an infinite number of equilibrium states. In phase space, these states all lie along the parametric curve  $\mathcal{E} = (r, 0, r^{-4})$ . To the best of the author's knowledge, this equilibrium curve in the model has not yet been discovered previously. While this equilibrium curve includes the conventional fixed point  $\mathcal{H} = (1, 0, 1)$ , deriving directly from the hydrostatic equilibrium case of Euler's Equation, small perturbations away from  $\mathcal{H}$  may lead to the star settling onto another fixed point along  $\mathcal{E}$ .

Since we could not use linear stability analysis on the entirety of  $\mathcal{E}$  in the full three-dimensional phase space, we performed linear stability analysis on the individual fixed points of  $\mathcal{E}$  on the two-dimensional  $r = \text{constant}$  slices which span the entire phase space (aside from  $r = 0$ ). Through this, we showed that on these surfaces, the fixed points of  $\mathcal{E}$  are always stable. Specifically, for physically relevant values of the radius, these fixed points are stable spirals. This led us to posit that trajectories in the full three-dimensional phase space, emanating from initial conditions near  $\mathcal{H}$ , were likely to exhibit spiral-like behavior before ultimately settling on some part of  $\mathcal{E}$ . This behavior is precisely what we observed. We further found that the decrease of the non-adiabaticity parameter  $\xi$  leads to an accentuation of this spiral-like behavior, along with a corresponding faster approach to  $\mathcal{E}$ .

However, due to the transient nature of the oscillations that we identified in this model, we find that it cannot reproduce the long-term oscillations expected for long-period variable stars. Thus, our unique insight is that in the formalism of the dynamical system used here, the constant opacity exponents  $n = 1$  and  $s = 3$  are not a good choice for use in modelling long-period variables.

On the other hand, for the Munteanu model which has dynamically evolving opacity exponents, we contribute to the established literature by providing the specific classifications of the three equilibrium solutions, which are all fixed points. These had previously only been generally identified as unstable by Munteanu et al. (2003) [26], so we added a more precise characterization of these solutions. We found that, for the relevant values of the parameters  $a$  and  $\xi$ , the fixed points  $\mathcal{H}$  and  $\mathcal{B} \approx (0.68, 0, 4.75)$  are saddle-foci, while the physically unrealistic  $\mathcal{C} \approx (8.8858, 0, 0.0002)$  is an unstable focus node. We noted that trajectories emanating near  $\mathcal{C}$  end up as unphysical divergent solutions. An intriguing behavior we observed is that trajectories emanating near  $\mathcal{B}$  end up settling onto the same limit cycles that had previously been found by Saitou et al. (1989) and Munteanu et al. (2003) around the fixed point  $\mathcal{H}$  [26, 37].

We also gave specific focus to the period-doubling routes to chaos in the Munteanu model from the variation in the  $\kappa$ -mechanism control parameter  $a$ , and the one from variation of the strength of non-adiabaticity  $\xi$ . Through the use of Lorenz Maps of the pressure  $p$ , we show this period-doubling phenomena clearly via the increase in the number of points on the maps. Using this, we correct a claim by Saitou et al. (1989) that the  $a = 15$ ,  $\xi = 0.08$  solution of the model is period-4, we in fact find

that it is more correctly described as period-6 [37].

Saitou et al. (1989) had previously characterized a chaotic solution of the Munteanu model with parameter values  $a = 13.5$ ,  $\xi = 0.08$  from the  $\kappa$ -mechanism route to chaos as showing a “y”-shaped strange attractor in its Lorenz Map. This was said to show a correspondence to observational luminosity return maps of the Semiregular variables S Vul and WY And [37]. Our unique discovery is that the chaotic solution with parameter values  $a = 20$ ,  $\xi = 0.12$  from the non-adiabaticity route to chaos also exhibits a clear “y”-shaped strange attractor in its corresponding Lorenz Map. This is noteworthy as it may mean that the luminosity return maps of those two stars, and potentially others like them, could just as well be described as having strange attractors from the non-adiabaticity route to chaos.

Finally, we performed time-delay embedding reconstructions of the attractors with the parameter values corresponding to the two “y”-shaped Lorenz Maps from the two distinct routes to chaos. We found that when the radius  $r$  is used for the reconstruction, we get an optimal delay time of  $\tau_{opt} \approx 80$  and minimal embedding dimension  $d_e = 3$ , for both routes to chaos. On the other hand, when the radial velocity  $v$  is used, we have  $\tau_{opt} \approx 73$  and  $d_e = 4$ .

The work we performed using the Lorenz Maps and time-delay reconstructions is potentially useful in that it adds to the body of results from the Munteanu one-zone model that may be compared to observational data of long-period variable stars. As we expounded upon earlier, the fact that these make use of only a single state variable at a time, such as the radius  $r$  or radial velocity  $v$ , may more readily allow for comparisons with observational data. This is because such observations may not simultaneously have good data for more than a single state variable at a time.

## 7.2 Recommendations for future work

We hope to be able more completely prove the stability of the equilibrium curve  $\mathcal{E}$  in the Stellingwerf model by the identification of a corresponding Lyapunov function. This would allow us to identify the specific regions of phase space wherein the stability of  $\mathcal{E}$  holds.

With regards to the Munteanu model, a full characterization of the parameter space  $\{a, \xi\}$ , such as the construction of a two-parameter bifurcation diagram would allow for a more complete exploration of possible chaotic solutions in the model.

Furthermore, with the presence of data from modern space telescopes such as Kepler, TESS, Gaia, etc., it would be of much interest to compare the solutions of the Munteanu model with observational data of irregular pulsations of long-period variable stars. As we previously stated, the Lorenz Maps and time-delay embeddings we performed may allow for more straightforward comparison with such observational data, since they make use of only single state variables such as the radius  $r$  and radial velocity  $v$ .

Finally, a more complete identification of some of the geometric measures of the strange attractors in the Munteanu model such as the Lyapunov exponents, correlation dimension, etc. would also be of interest.

# Bibliography

- [1] G. Amaral, C. Letellier, and L. Aguirre. Piecewise affine models of chaotic attractors: The Rössler and Lorenz systems. *Chaos*, 16(1):013115, 2006.
- [2] N. H. Baker, R. F. Stein, and A.G. W. Cameron. *Stellar Evolution*. Plenum Press, New York, 1966.
- [3] H. Binous. Mapping the maxima for a nonisothermal chemical system. <http://demonstrations.wolfram.com/MappingTheMaximaForANonisothermalChemicalSystem/>, 2012. Wolfram Demonstrations Project.
- [4] H. Binous, A. Bellagi, and B. G. Higgins. The Lorenz Map: Short-term predictability of chaotic systems. <http://demonstrations.wolfram.com/TheLorenzMapShortTermPredictabilityOfChaoticSystems/>, 2013. Wolfram Demonstrations Project.
- [5] A. Bódi, K. Szatmáry, and L. L. Kiss. Periodicities of the RV Tauri-type pulsating star DF Cygni: A combination of Kepler data with ground-based observations. *Astron. Astrophys.*, 596:A24, 2016.
- [6] J. R. Buchler. Chaotic pulsations in stellar models. *Annals of the New York Academy of Sciences*, 617:17–36, 1990.
- [7] J. R. Buchler and Z. Kolláth. Nonlinear analysis of irregular variables. *Astrophysics and Space Science Library*, page 185–213, 2001.
- [8] B. W. Carroll and D. A. Ostlie. *An Introduction to Modern Astrophysics*. Cambridge University Press, 2017.
- [9] B. Chun-Hua and N. Xin-Bao. Determining the minimum embedding dimension

- of nonlinear time series based on prediction method. *Chinese Physics*, 13(5):633–636, 2004.
- [10] A. S. Eddington. On the cause of Cepheid pulsation. *Mon. Not. R. Astron. Soc.*, 101:182–194, 1941.
- [11] S. Engle. *The Secret Lives of Cepheids: A Multi-Wavelength Study of the Atmospheres and Real-Time Evolution of Classical Cepheids*. PhD thesis, James Cook University, 2015.
- [12] J. Guckenheimer and P. Holmes. *Nonlinear oscillations, dynamical systems, and bifurcations of vector fields*. Applied mathematical sciences ; v. 42. Springer-Verlag, New York, 1983.
- [13] O. J. Hall, G. R. Davies, J. van Saders, Nielsen M. B., Lund M. N., Chaplin W. J. Chaplin, R. A. García, L. Amard, A. A. Breimann, S. Khan, V. See, and J. Tayar. Weakened magnetic braking supported by asteroseismic rotation rates of kepler dwarfs. *Nature Astronomy*, 5(7):707–714, 2021.
- [14] V. Icke, A. Frank, and A. Heske. Weak chaos in long-period variables. *Astron. Astrophys.*, 258:341–356, 1992.
- [15] E. M. Izhikevich. Equilibrium. *Scholarpedia*, 2(10):2014, 2007. revision #91238.
- [16] D. Jordan and P. Smith. *Nonlinear Ordinary Differential Equations: An Introduction for Scientists and Engineers*. Oxford Texts in Applied and Engineering Mathematics. OUP Oxford, 2007.
- [17] H. Kantz and T. Schreiber. *Nonlinear Time Series Analysis*. Cambridge University Press, USA, 2003.
- [18] M. B. Kennel, R. Brown, and H. D. I. Abarbanel. Determining embedding dimension for phase-space reconstruction using a geometrical construction. *Phys. Rev. A*, 45:3403–3411, 1992.
- [19] L. L. Kiss, K. Szatmáry, Jr. Cadmus, R. R., and J. A. Mattei. Multiperiodicity in semiregular variables. I. General properties. *Astron. Astrophys.*, 346:542–555, 1999.

- [20] J. F. Lindner, V. Kohar, B. Kia, M. Hippke, J. G. Learned, and W. L. Ditto. Strange nonchaotic stars. *Phys. Rev. Lett.*, 114:054101, 2015.
- [21] E. Lorenz. Deterministic nonperiodic flow. *Journal of Atmospheric Sciences*, 20(2):130–148, March 1963.
- [22] S. Lynch et al. *Dynamical Systems with Applications Using Mathematica®*. Springer, 2007.
- [23] D. W. Moore and E. A. Spiegel. A thermally excited non-linear oscillator. *Astrophys. J.*, 143:871–887, 1966.
- [24] A. Munteanu. *Nonlinear one-zone models of stellar pulsations*. Universitat Politècnica de Catalunya, 2003.
- [25] A. Munteanu, E. Garcia-Berro, and J. Jose. Bursting oscillations in long-period variables. In *Interplay of Periodic, Cyclic and Stochastic Variability in Selected Areas of the HR Diagram*, page 285, Brussels, Belgium, 2002.
- [26] A. Munteanu, E. García-Berro, and J. José. A weakly non-adiabatic one-zone model of stellar pulsations: application to Mira stars. *Mon. Not. R. Astron. Soc.*, 341(3):855–862, 2003.
- [27] E. Ott. *Chaos in Dynamical Systems*. Cambridge University Press, 1993.
- [28] J. R. Percy. *Understanding Variable Stars*. Cambridge University Press, 2007.
- [29] L. E. Persson. *A basic course in applied mathematics. Applied Mathematics, Lecture notes, Luleå University of Technology*. Sweden.
- [30] R. A. Phillipson, P. T. Boyd, and A. P. Smale. The chaotic long-term X-ray variability of 4U 1705–44. *Monthly Notices of the Royal Astronomical Society*, 477(4):5220–5237, 2018.
- [31] H. Pi and C. Peterson. Finding the embedding dimension and variable dependencies in time series. *Neural Computation*, 6(3):509–520, 05 1994.
- [32] E. Plachy, A. Bódi, and Z. Kolláth. Chaotic dynamics in the pulsation of DF Cygni, as observed by Kepler. *Monthly Notices of the Royal Astronomical Society*, 481(3):2986–2993, 2018.

- [33] R. Roberts. AAVSO long period variable section. <https://www.aavso.org/aavso-long-period-variable-section>, 2020.
- [34] M. R. Roussel. *Nonlinear Dynamics, Lecture notes, University Hall*. Canada, 2005.
- [35] T. J. Rudd and R. M. Rosenberg. A simple model for Cepheid variability. *Astron. Astrophys.*, 6:193–205, 1970.
- [36] H. Ruskeepää. Analysis of chaotic data with Mathematica. <https://library.wolfram.com/infocenter/MathSource/8775/>, 2014. Wolfram Library Archive.
- [37] M. Saitou, M. Takeuti, and Y. Tanaka. Chaotic behavior in nonlinear radial oscillations of one-zone stellar models. *Publ. Astron. Soc. Jpn.*, 41:297–309, 1989.
- [38] R. F. Stellingwerf. Luminosity variation in the one-zone Cepheid model. *Astron. Astrophys.*, 21:91–96, 1972.
- [39] R. F. Stellingwerf. A simple model for coupled convection and pulsation. *Astrophys. J.*, 303:119–129, 1986.
- [40] S. H. Strogatz. *Nonlinear Dynamics and Chaos: With Applications to Physics, Biology, Chemistry, and Engineering*. CRC Press, 2018.
- [41] F. Takens. Detecting strange attractors in turbulence. In D. Rand and L.S. Young, editors, *Dynamical Systems and Turbulence, Warwick 1980*, pages 366–381, Berlin, Heidelberg, 1981. Springer Berlin Heidelberg.
- [42] F. Ulrike, S P. Kuznetsov, and P. Arkady. Strange nonchaotic attractors: Dynamics between order and chaos in quasiperiodically forced systems. 2006.
- [43] J.M. A. Yulo and M.F.I. G. Vega. Strange attractors of long-period variable stars in a one-zone model of stellar pulsation. In *Proceedings of the Samahang Pisika ng Pilipinas*, volume 39, pages SPP–2021–1C–04, 2021.
- [44] J. P. Zahn. On possible non-radial pulsations of Baker’s one-zone model. *Astrophysical Letters*, 1:209–212, 1968.